

Montana Tech Library

Digital Commons @ Montana Tech

---

Graduate Theses & Non-Theses

Student Scholarship

---

Fall 2020

**EFFECT OF GLOBAL ENERGY DENSITY ON DYNAMIC STRAIN  
HARDENING OF SELECTIVE LASER MELTED ALSI10MG**

MD Salah Uddin

Follow this and additional works at: [https://digitalcommons.mtech.edu/grad\\_rsch](https://digitalcommons.mtech.edu/grad_rsch)



Part of the [Materials Science and Engineering Commons](#)

---

EFFECT OF GLOBAL ENERGY DENSITY ON DYNAMIC STRAIN  
HARDENING OF SELECTIVE LASER MELTED ALSI10MG

by  
Md Salah Uddin

A dissertation submitted in partial fulfillment of the  
requirements for the degree of

Doctor of Philosophy:  
Materials Science

Montana Technological University

2020



EFFECT OF GLOBAL ENERGY DENSITY ON DYNAMIC STRAIN HARDENING OF  
SELECTIVE LASER MELTED ALSI10MG

By

MD SALAH UDDIN

B.Sc. Physics, University of Dhaka, Dhaka, Bangladesh, 2010

M.S. Physics, Miami University, Oxford, Ohio, 2016

M.S. Materials Science and Engineering, Montana Technological University, Butte, Montana,  
2019

Dissertation

presented in partial fulfillment of the requirements for the degree of

Doctor of Philosophy in Materials Science

Montana Technological University

Butte, MT

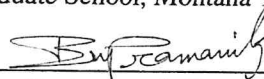
December 2020

Approved by:



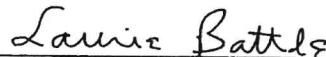
Beverly K. Hartline, Ph.D.

Vice Chancellor for Research and Dean of the Graduate School, Montana Tech Graduate School



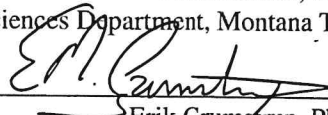
Brahmananda Pramanik, Ph.D., P.E., Chair

Associate Professor, Mechanical Engineering Department, Montana Tech



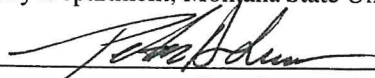
Laurie Battle, Ph.D.

Head and Professor, Mathematical Sciences Department, Montana Tech



Erik Grumstrup, Ph.D.

Associate Professor, Chemistry & Biochemistry Department, Montana State University



Peter Lucon, Ph.D., P.E.

Assistant Professor, Mechanical Engineering Department, Montana Tech



K.V. Sudhakar, Ph.D., P.E.

Professor, Metallurgical and Materials Engineering Department, Montana Tech

© COPYRIGHT

by

Md Salah Uddin

2020

All Rights Reserved

Salah Uddin, Md, Doctor of Philosophy in Materials Science, December 2020

Effect of Global Energy Density on Dynamic Strain Hardening of Selective Laser Melted

AlSi10Mg

Chairperson: Brahmananda Pramanik

The characteristics of strain hardening of selective laser melting (SLM) processed AlSi10Mg under dynamic impact was investigated. The dynamic impact at high strain rate loading conditions occurs in many engineering applications, such as collisions of flying objects on aircraft engine components like bird impact, vehicle collisions, and impacts occur in sports events like club impact on golf balls and helmet impact. Among these various applications, the strength of the materials needs to be characterized accurately for product quality, performance, and reliability.

AlSi10Mg is a lightweight metal alloy, and it has a growing demand in aircraft, military, and automotive applications. SLM is a manufacturing technique that uses a laser for the powder bed fusion-based product development process, and the method is applicable for producing AlSi10Mg parts. In the past few years, the microstructure, mechanical characteristics like quasi-static and toughness, and post-processing based on manufacturing parameters of the SLM built AlSi10Mg were studied by many researchers. However, the dynamic mechanical behavior, such as strain hardening behavior under different impact conditions, remains to be explored. For this work, split Hopkinson pressure bar (SHPB) and Charpy impact tester were used for the dynamic impact experimentation on the SLM built AlSi10Mg specimens.

The dynamic strain hardening response for the SLM built AlSi10Mg was investigated to explore the effects of manufacturing variables like the global energy density (GED) and the build orientation. The test specimens were produced at three GEDs of 37.1, 45.4, 49.9 J/mm<sup>3</sup>, and two build orientations: 0° and 90°. The specimens were tested under dynamic compressive impact conditions at strain rates of 800 to 2555 s<sup>-1</sup> using a split Hopkinson pressure bar (SHPB). The pendulum (hammer) loading test was conducted by using a standardized Charpy impact tester (i.e., ASTM E23). It was found that, at more than 95% confidence limit, the maximum flow stress, which is related to the strain hardening behavior, was influenced by build orientation and global energy density. Also, at more than 95% confidence limit, the void growth, type of fractures, and roughness were affected by global energy density and build orientation. That influenced the strain hardenability of the SLM built AlSi10Mg specimens.

Keywords: Selective Laser Melting, AlSi10Mg, Split Hopkinson Pressure Bar, Charpy Impact Test, Strain Hardening

## **Dedication**

To my family:

The greatest gift from Allah (Glorious and Exalted): dear mom, dad, wife, and brother.

Thank you.

## Acknowledgments

I would like to offer my wholehearted and sincere gratitude to my advisor, Dr. Brahmananda Pramanik, for his guidance and support towards the completion of the dissertation in Materials science. Also, my earnest thanks to my committee: Dr. K.V. Sudhakar, Dr. Laurie Battle, Dr. Erik Grumstrup, and Dr. Peter Lucon.

With my sincere and hearty gratitude, I would like to thank Dr. Richard LaDouceur for the help with statistical interpretation and Cristina Stefanescu and Gary Wyss for the scanning electron microscope.

Also, I acknowledge the Center for Advanced Mineral and Metallurgical Processing (CAMP) for providing me the opportunity of performing the X-ray diffraction experiment.

At last, I acknowledge the Army Research Laboratory (ARL) and Montana Technological University: Cooperative Agreement W911NF-15-2-0020 for providing me support for the dissertation research and doctoral education.

## Table of Contents

<b>DEDICATION .....</b>	<b>V</b>
<b>ACKNOWLEDGMENTS .....</b>	<b>VI</b>
<b>LIST OF TABLES .....</b>	<b>X</b>
<b>LIST OF FIGURES.....</b>	<b>XIII</b>
<b>LIST OF EQUATIONS .....</b>	<b>XX</b>
<b>GLOSSARY OF TERMS.....</b>	<b>XXII</b>
1. INTRODUCTION .....	1
1.1. <i>Research Background</i> .....	3
1.1.1. Dynamic Impact using SHPB Testing Method.....	3
1.1.2. Dynamic Impact using Charpy Testing Method.....	5
2. MATERIALS AND MANUFACTURING METHOD.....	7
2.1. <i>Manufacturing of the Specimens</i> .....	8
2.2. <i>Preparation of the Specimens</i> .....	9
2.2.1. CVN Test Specimens.....	9
2.2.2. SHPB Specimens .....	11
2.3. <i>Statistical Analysis</i> .....	13
3. STRAIN HARDENING BEHAVIOR: SPLIT HOPKINSON PRESSURE BAR EXPERIMENT .....	15
3.1. <i>SHPB Data Analysis</i> .....	18
3.2. <i>Maximum Flow Stress</i> .....	25
3.2.1. Statistical Significance: Maximum Flow Stress .....	26
3.3. <i>Energy Absorption Behavior</i> .....	26
3.3.1. Statistical Significance: Energy Absorption Behavior .....	27
3.4. <i>Temperature Rise in Adiabatic Heating</i> .....	28
3.4.1. Statistical Significance: Adiabatic Temperature Rise .....	29

3.5.	<i>Development of Shear Plane</i> .....	30
3.6.	<i>Strain Hardening Behavior</i> .....	31
3.7.	<i>Observation</i> .....	33
3.7.1.	Effects of Build Orientation on Strain Hardening Behavior .....	33
3.7.2.	Effects of GED on Strain Hardening Behavior .....	34
3.8.	<i>Future Research</i> .....	35
4.	STRAIN HARDENING BEHAVIOR: CHARPY IMPACT TEST .....	36
4.1.	<i>Surface Roughness</i> .....	45
4.1.1.	Section-Wise Surface Roughness .....	50
4.1.1.1.	Tension Region .....	50
4.1.1.2.	Neutral Region .....	52
4.1.1.3.	Compression Region .....	55
4.1.2.	The Roughness of the Total Fractured Surface Area .....	59
4.1.2.1.	Statistical Significance: Roughness for Total Fractured Surface .....	60
4.2.	<i>Observation</i> .....	61
4.3.	<i>Future Research</i> .....	61
5.	FRACTURE SURFACE ANALYSIS .....	62
5.1.	<i>Void-Size Estimation</i> .....	70
5.1.1.	Void Size at Tension, Neutral, and Compression Region – Specimens Prepared at 37.1J/mm <sup>3</sup> .....	72
5.1.2.	Void Size at Tension, Neutral, and Compression Region – Specimens Prepared at 45.4J/mm <sup>3</sup> .....	73
5.1.3.	Void Size at Tension, Neutral, and Compression Region – Specimens Prepared at 49.9J/mm <sup>3</sup> .....	74
5.1.4.	Statistical Significance: Void Size at Tension region .....	75
5.1.5.	Statistical Significance: Void Size at Neutral Region .....	76
5.1.6.	Statistical Significance: Void Size at Compression Region .....	77
5.1.7.	Void Size at GEDs: 37.1, 45.4, and 49.9J/mm <sup>3</sup> .....	78
5.1.7.1.	Statistical Significance: Void Size at GEDs: 37.1, 45.4, and 49.9J/mm <sup>3</sup> .....	79
5.2.	<i>Observation</i> .....	80
6.	MICROANALYSIS: TESTED CHARPY AND SPLIT HOPKINSON PRESSURE BAR SPECIMENS .....	82

6.1.	<i>Concept and Theory for the Microanalysis</i> .....	83
6.2.	<i>X-ray Diffraction Experiment</i> .....	89
6.2.1.	CVN Specimens.....	89
6.2.2.	SHPB Specimens .....	90
6.3.	<i>Microanalysis for the CVN Specimens</i> .....	91
6.3.1.	Lattice Strain.....	94
6.3.2.	Deformation Energy Density .....	95
6.3.3.	Crystal Size .....	96
6.4.	<i>Microanalysis for the SHPB Specimens</i> .....	97
6.4.1.	Lattice Strain.....	101
6.4.1.1.	Statistical Significance: Lattice Strain .....	103
6.4.2.	Deformation Energy Density .....	104
6.4.2.1.	Statistical Significance: Deformation Energy.....	105
6.4.3.	Crystal Size .....	106
6.4.3.1.	Statistical Significance: Crystal Size .....	107
6.5.	<i>Observation</i> .....	108
7.	CONCLUSION .....	109
8.	REFERENCES CITED.....	110

## List of Tables

Table I: The AlSi10Mg alloy composition (, wt%) [23] .....	7
Table II: Processing parameters of the SLM built AlSi10Mg specimens .....	9
Table III: Design parameters of the bars of the SHPB experiment [28].....	12
Table IV: Maximum flow stress: the statistical sample size for the ‘student’s T-test’ .....	26
Table V: Student’s T-test for the maximum flow stress .....	26
Table VI: Energy absorption behavior: the statistical sample size for the ‘student’s T-test’	28
Table VII: Student’s T-test for energy absorption behavior .....	28
Table VIII: Adiabatic temperature rise: the statistical sample size for the ‘student’s T-test’ .....	29
Table IX: Student’s T-test for the adiabatic temperature rise.....	30
Table X: Absorbed energy of SLM-AlSi10Mg specimens in the Charpy impact test. ....	36
Table XI: Roughness on tension region: the statistical sample size for the ‘student’s T-test’ .....	52
Table XII: Student’s T-test for the roughness on the tension region.....	52
Table XIII: Roughness on neutral region: the statistical sample size for the ‘student’s T-test’ .....	54
Table XIV: Student’s T-test for the roughness on the neutral region.....	55
Table XV: Roughness on compression region: the statistical sample size for the ‘student’s T-test’ .....	58
Table XVI: Student’s T-test for the roughness on the compression region.....	58
Table XVII: Roughness for total fractured surface: the statistical sample size for the ‘student’s T- test’ .....	61

Table XVIII: Student’s T-test for the roughness for total fractured surface.....	61
Table XIX: Void size at tension region: the statistical sample size for the ‘student’s T-test’ .....	75
Table XX: Student’s T-test for the void size at the tension region.....	76
Table XXI: Void size at neutral region: the statistical sample size for the ‘student’s T-test’ .....	76
Table XXII: Student’s T-test for the void size at the neutral region .....	77
Table XXIII: Void size at compression region: the statistical sample size for the ‘student’s T- test’ .....	77
Table XXIV: Student’s T-test for the void size at the compression region.....	78
Table XXV: Void size at GEDs: 37.1, 45.4, and 49.9J/mm <sup>3</sup> : the statistical sample size for the ‘student’s T-test’ .....	79
Table XXVI: Student’s T-test for the void size at GEDs: 37.1, 45.4, and 49.9J/mm <sup>3</sup> .....	80
Table XXVII: Geometric parameters of the SLM-AISI10Mg CVN specimens. The specimens were prepared at two build orientations (BO): 0° and 90°, and three GEDs: 37.1, 45.4, and 49.9J/mm <sup>3</sup> and tested under Chapry impact loading.....	94
Table XXVIII: Geometric parameters of the SLM-AISI10Mg SHPB specimens. The specimens were prepared at two build orientations (BO): 0° and 90°, and three GEDs: 37.1, 45.4, and 49.9J/mm <sup>3</sup> and examined at different strain rates, which range from 800 to 2555s <sup>-1</sup> using SHPB.....	101
Table XXIX: Maximum strain rate applied for the SHPB specimens.....	102
Table XXX: Lattice strain: the statistical sample size for the ‘student’s T-test’ .....	103
Table XXXI: Student’s T-test for the lattice strain.....	104

Table XXXII: Deformation energy: the statistical sample size for the ‘student’s T-test’	105
Table XXXIII: Student’s T-test for the deformation energy .....	106
Table XXXIV: Crystal size: the statistical sample size for the ‘student’s T-test’ .....	107
Table XXXV: Student’s T-test for the crystal size .....	108

## List of Figures

- Figure 1: An Al-Si binary phase diagram. In the diagram, the eutectic composition of silicon (Si) is 12.6 wt.% [22].....7
- Figure 2: Schematic diagram of standardized Charpy V-notch specimen: (a) surface in the transverse direction where the area of the surface is 10 mm × 10 mm and (b) surface in the longitudinal direction where the surface area is 10 mm × 55 mm.....10
- Figure 3: A schematic diagram of the build orientation of the CVN specimen. A black arrow (▲) indicates the location of the pendulum impact that occurs in the test specimen. ..11
- Figure 4: A SHPB specimen is cylindrical in shape. It has a diameter and height, both are 9.50 mm (or 0.37 in). .....12
- Figure 5: A schematic diagram of the build orientation of the SHPB specimens is presented. ....13
- Figure 6: Distribution of the strain rates with multiple specimens reported for the SHPB experiment.....15
- Figure 7: Split Hopkinson Pressure Bar (SHPB) tested specimens: (a) GED of 37.1J/mm<sup>3</sup> and build at 0°, (b) GED of 37.1J/mm<sup>3</sup> and build at 90°, (c) GED of 45.4J/mm<sup>3</sup> and build at 0°, (d) GED of 45.4J/mm<sup>3</sup> and build at 90°, (e) GED of 49.9J/mm<sup>3</sup> and build at 0°, and (f) GED of 49.9J/mm<sup>3</sup> and build at 90°. .....18
- Figure 8: A simple schematic diagram of the Split Hopkinson Pressure Bar apparatus. ..19
- Figure 9: Schematic diagram of the SHPB experiment [31] .....19
- Figure 10: Typical incident and transmission bar pulses of the SHPB experiment. The incident bar pulses are marked with a “blue” color, and the transmission bar pulse is marked with an “orange” color. ....20

- Figure 11: The incident pulse is in blue, the reflected pulse is in red, and the transmitted pulse is in green. An incident bar pulse is a combination of reflected and transmitted wave pulses. ....21
- Figure 12: The average maximum flow stress of the SHPB specimens tested at a range of strain rates. The standard deviation of the data is shown using error bars. ....25
- Figure 13: The average energy absorption capacity of the SHPB specimens tested at a range of strain rates. The standard deviation of the data is shown using error bars. ....27
- Figure 14: The average adiabatic temperature rise of the SHPB specimens tested at a range of strain rates. The standard deviation of the data is shown here using error bars. ...29
- Figure 15: Investigating the development of the shear plane of the tested SHPB specimen: (a) schematic diagram of the shear plane and (b) SHPB tested specimen where no shear plane was observed. ....31
- Figure 16: Strain hardening behavior of the specimens built at a GED of  $37.1\text{J/mm}^3$  and two build orientations:  $0^\circ$  and  $90^\circ$ . ....32
- Figure 17: Strain hardening behavior of the specimens built at a GED of  $45.4\text{J/mm}^3$  and two build orientations:  $0^\circ$  and  $90^\circ$ . ....32
- Figure 18: Strain hardening behavior of the specimens built at a GED of  $49.9\text{J/mm}^3$  and two build orientations:  $0^\circ$  and  $90^\circ$ . ....33
- Figure 19: A correlation between toughness and roughness. Here  $\xi$  is for the ductile fracture surface roughness, and  $J_{IC}$  is a measure of the material's resistance to crack growth [42]. Here,  $e_x$  is the in-plane (x-y plane) element dimension (i.e., normalized length), and  $J_{IC}$  is normalized by the reference flow strength,  $\sigma_0$  ( $= 300\text{MPa}$ ) and  $e_x$  [42]. ....37

Figure 20: A strength–toughness relationship for engineering materials is presented by the Ashby plot [44].	38
Figure 21: A schematic diagram of a fractured surface image was captured by a digital microscope at 300x magnification for a tested CVN specimen.	42
Figure 22: A 3D fractured surface image of a tested CVN specimen captured by a digital microscope at 300x magnification.	43
Figure 23: A surface profile was taken from one of the 72 images of a tested CVN specimen’s fractured surface. The development of the profile and profile image were captured by a digital microscope. The roughness ( $R_s$ ) of the profile above is $R_s = 1.29$	44
Figure 24: A schematic diagram of three regions: tension, neutral, and compression, of a fractured surface of a tested CVN specimen.	45
Figure 25: Average roughness of the fractured surface of the CVN specimens built at a GED of $37.1\text{J}/\text{mm}^3$ and $0^\circ$ build orientation.	46
Figure 26: Average roughness of the fractured surface of the CVN specimens built at a GED of $37.1\text{J}/\text{mm}^3$ and $90^\circ$ build orientation.	46
Figure 27: Average roughness of the fractured surface of the CVN specimens built at a GED of $45.4\text{J}/\text{mm}^3$ and $0^\circ$ build orientation.	47
Figure 28: Average roughness of the fractured surface of the CVN specimens built at a GED of $45.4\text{J}/\text{mm}^3$ and $90^\circ$ build orientation.	48
Figure 29: Average roughness of the fractured surface of the CVN specimens built at a GED of $49.9\text{J}/\text{mm}^3$ and $0^\circ$ build orientation.	48
Figure 30: Average roughness of the fractured surface of the CVN specimens built at a GED of $49.9\text{J}/\text{mm}^3$ and $90^\circ$ build orientation.	49

Figure 31: A schematic diagram of the ‘tension’ region of a CVN specimen.....	50
Figure 32: Average roughness of the ‘tension’ region of the CVN specimens. ....	51
Figure 33: A schematic diagram of the ‘neutral’ region of a CVN specimen. ....	53
Figure 34: Average roughness of the ‘neutral’ region of the CVN specimens.....	53
Figure 35: A schematic diagram of the ‘compression’ region of a CVN specimen. ....	56
Figure 36: Average roughness of the ‘compression’ region of the CVN specimens.....	57
Figure 37: A schematic diagram of the total fractured surface area of a CVN specimen. ....	59
Figure 38: Average roughness of the total fractured surface area of the CVN specimens.....	60
Figure 39: The fractured surface of the CVN specimen built at a GED $37.1\text{J}/\text{mm}^3$ - $0^\circ$ . The image was captured by a digital microscope. ....	63
Figure 40: The fractured surface of the CVN specimen built at a GED $37.1\text{J}/\text{mm}^3$ - $90^\circ$ . The image was captured by a digital microscope. ....	63
Figure 41: The fractured surface of the CVN specimen built at a GED $45.4\text{J}/\text{mm}^3$ - $0^\circ$ . The image was captured by a digital microscope. ....	64
Figure 42: The fractured surface of the CVN specimen built at a GED $45.4\text{J}/\text{mm}^3$ - $90^\circ$ . The image was captured by a digital microscope. ....	64
Figure 43: The fractured surface of the CVN specimen built at a GED $49.9\text{J}/\text{mm}^3$ - $0^\circ$ . The image was captured by a digital microscope. ....	65
Figure 44: The fractured surface of the CVN specimen built at a GED $49.9\text{J}/\text{mm}^3$ - $90^\circ$ . The image was captured by a digital microscope. ....	66
Figure 45: The fractured surface of the CVN specimen built at a GED $37.1\text{J}/\text{mm}^3$ - $0^\circ$ . The image was captured under an SEM. ....	67

- Figure 46: The fractured surface of the CVN specimen built at a GED  $37.1\text{J}/\text{mm}^3$ - $90^\circ$ . The image was captured under an SEM. ....67
- Figure 47: The fractured surface of the CVN specimen built at a GED  $45.4\text{J}/\text{mm}^3$ - $0^\circ$ . The image was captured under an SEM. ....68
- Figure 48: The fractured surface of the CVN specimen built at a GED  $45.4\text{J}/\text{mm}^3$ - $90^\circ$ . The image was captured under an SEM. ....68
- Figure 49: The fractured surface of the CVN specimen built at a GED  $49.9\text{J}/\text{mm}^3$ - $0^\circ$ . The image was captured under an SEM. ....69
- Figure 50: The fractured surface of the CVN specimen built at a GED  $49.9\text{J}/\text{mm}^3$ - $90^\circ$ . The image was captured under an SEM. ....69
- Figure 51: A schematic diagram of the 2-point measurement method for measuring the void size. [1] and [2] present the length of the coalescence of voids, [3] and [4] illustrate the peanut-shaped void (which is a type of coalescence of voids), and [5] shows for a single void. ....70
- Figure 52: Schematic diagram of the three regions: tension, neutral, and compression, of the CVN specimen. It was also described in Chapter 4. ....71
- Figure 53: A schematic diagram of all the image sections of the CVN specimen's fractured surface. The void measurement was performed on the rows marked as 'yellow' color. ....72
- Figure 54: An average voids size of the three regions of two build orientation:  $0^\circ$  and  $90^\circ$ . The specimens were built at a GED of  $37.1\text{ J}/\text{mm}^3$ . ....73
- Figure 55: An average voids size of the three regions of two build orientation:  $0^\circ$  and  $90^\circ$ . The specimens were built at a GED of  $45.4\text{ J}/\text{mm}^3$ . ....74

Figure 56: An average voids size of the three regions of two build orientation: 0° and 90°. The specimens were built at a GED of 49.9 J/mm <sup>3</sup> . .....	75
Figure 57: An average voids size at two build orientations: 0° and 90° and at three GEDs: 37.1, 45.4, and 49.9 J/mm <sup>3</sup> .....	79
Figure 58: A schematic diagram of lattice strain based, shift, and broadening [65]. .....	83
Figure 59: A tested SLM built AlSi10Mg CVN specimen: (a) tested specimen, where the V-notch is shown on the top of the diagram and hammer impact zone is opposite to the face of V-notch. The crack initiates at the V-notch due to the impact, (b) the flat surface where XRD was performed, and (c) the fractured surface of the specimen.....	90
Figure 60: XRD experiment was performed on the flat surface of the tested SHPB specimens: (a) tested SHPB specimen, and (b) a schematic diagram of the stress wave propagation direction. ....	91
Figure 61: The XRD line graph for the tested CVN specimens. ....	92
Figure 62: The average of the Bragg's angle for each peak of aluminum in the XRD line graphs for the tested CVN specimens.....	93
Figure 63: Standard deviation from the average of the Bragg's angle for each aluminum peak of Figure 71 .....	93
Figure 64: The average lattice strain of the tested CVN specimens. ....	95
Figure 65: The average deformation energy density of the tested CVN specimens.....	96
Figure 66: The average size of the crystal of the tested CVN specimens.....	97
Figure 67: The XRD line graph for the specimens built at GED of 37.1J/mm <sup>3</sup> .....	98
Figure 68: The XRD line graph for the specimens built at GED of 45.4J/mm <sup>3</sup> .....	99
Figure 69: The XRD line graph for the specimens built at GED of 49.9J/mm <sup>3</sup> .....	99

Figure 70: The average of the Bragg's angle for each peak of aluminum in the XRD line graphs for the tested SHPB specimens. ....	100
Figure 71: Standard deviation from the average of the Bragg's angle for each aluminum peak of Figure 79. ....	100
Figure 72: The average lattice strain of the tested SHPB specimens. ....	103
Figure 73: The average deformation energy density of the tested SHPB specimens. ....	105
Figure 74: The average size of the crystal of the tested SHPB specimens. ....	107

## List of Equations

Equation 1: Global energy density.....	8
Equation 2: Normal strain rate.....	22
Equation 3: Normal strain.....	22
Equation 4: Normal stress.....	22
Equation 5: True strain.....	23
Equation 6: True strain rate.....	23
Equation 7: True stress.....	23
Equation 8: Energy absorption capacity.....	24
Equation 9: Adiabatic temperature rise.....	24
Equation 10: Holloman Equation.....	38
Equation 12: Relation between surface roughness and strength co-efficient.....	39
Equation 12: Hooke's law.....	39
Equation 13: Relation between roughness and strength of the material.....	39
Equation 14: Surface roughness model.....	40
Equation 15: Profile roughness parameter.....	40
Equation 16: Integrated width of the diffraction peak.....	84
Equation 17: Instrumental broadening correction.....	85
Equation 18: Scherrer's equation.....	85
Equation 19: Stokes and Wilson formula.....	86
Equation 20: Uniform deformation model (UDM).....	86
Equation 21: Hooke's law.....	87
Equation 22: Young's modulus of the cubic crystals [74].....	87

Equation 23: Uniform stress deformation model (USDm).....	88
Equation 24: Deformation energy density .....	88
Equation 25: Uniform deformation energy density model (UDEDm).....	89

## Glossary of Terms

<b>Term</b>	<b>Definition</b>
3D	Three-dimensional
SLM	Selective Laser Melting
GED	Global Energy Density
BO	Build Orientation
SHPB	Split Hopkinson Pressure Bar
CVN	Charpy V-notch
SEM	Scanning Electron Microscope
HRSEM	High-Resolution Scanning Electron Microscope
XRD	X-ray Diffraction
UDM	Uniform Deformation Model
USDM	Uniform Stress Deformation Model
UDEDM	Uniform Deformation Energy Density Model

## 1. Introduction

AlSi10Mg is a casting alloy with growing demand in the aerospace and automotive industries because it exhibits good fluidity and produces low shrinkage [1,2]. The chemical composition is at near-eutectic, so-called hypoeutectic alloy. It is a lightweight metal alloy with high corrosion resistance, excellent electric and thermal conductivity, and cost-effectiveness [3]. The solidification range of AlSi10Mg alloy is significantly less than that of any higher-strength aluminum alloys, such as of 7000 series. Hence, the application of the selective laser melting (SLM) method for processing AlSi10Mg alloy becomes convenient [4]. In this research, the mechanical characteristics of SLM-processed AlSi10Mg under dynamic loading condition is investigated.

The selective laser melting (SLM) method applies laser power to fuse metal powder bed with a layer-by-layer strategy and builds a metal structure [5]. The SLM process enables greater design freedom, customization, higher complexity, more significant topology-optimized forms, and less material waste than conventional subtractive manufacturing techniques [6]. In the manufacturing process using this technique, the process parameters are influential in developing an anisotropy in the produced part. The anisotropy affects the microstructure. Thus, it changes the strength of the material. Laser power, laser scan speed, and build orientations are important processing parameters for developing an anisotropy of the material. In this investigation, the SLM built AlSi10Mg specimens were prepared at two build orientations of the layers:  $0^\circ$  and  $90^\circ$ . Three different global energy densities (GEDs) of 37.1, 45.4, and  $49.9 \text{ J/mm}^3$  were applied in processing the specimens. The global energy density (GED) is a processing parameter derived from the laser power applied in the fabrication process, laser movement defined by laser scanning speed, hatch spacing is identified as the distance between the consecutive laser

scanning paths, and build layer thickness. In the next chapter, the diagram of the build orientations and GEDs will be presented.

The conventional mechanical testing equipment can measure yield stress and ultimate strength at a quasi-static loading rate (approximately  $10^{-3} \text{ s}^{-1}$ ). However, determining the mechanical behavior under high strain rate (i.e.:  $10^2$ - $10^4 \text{ s}^{-1}$ ) impact is beyond the scope of common material testing experiments [7]. Typically, the high strain rate impact occurs in collision-related loading conditions. Small objects like birds can hit on aircraft engine components by accident. The club's blow on golf-balls, the helmet impacted by hard surfaces, and different types of vehicle collisions are few examples from our life. Therefore, to ascertain the quality and reliability of material for various applications such as high strain rate (HSR) impact, the mechanical strength needs to characterize. However, the high strain rate behavior (i.e., the dependence of the plastic stress on the flow-strain, varied strain rates, and at elevated temperatures) of many materials was not well-understood [8].

Most mechanical testing machines experience difficulties achieving stress equilibrium at a high loading rate. An example of the dynamic impact at a high strain rate regime can be replicated with a hammer impact [7]. In the past, two issues were experienced in characterizing materials properties for a hammer impact; first, limited information was recorded. Second, the specimens were not properly stress-equilibrated [7]. The issues were solved by introducing a specialized mechanical testing machine called a split Hopkinson pressure bar (SHPB). It characterizes the material's mechanical behavior of the materials under dynamic loading. It can deform the material at a high strain rate by ramping the stress at nominal equilibrium conditions. Another type of hammer impact experiment is known as the Charpy impact experiment. It is a standard laboratory testing method to determine the materials' impact toughness [9]. In the

Charpy impact testing method, a pendulum is used as a hammer to produce a dynamic impact on the specimen. During the pendulum impact, the hammer strikes the specimen to break. The energy absorbed to break (or fracture) the test specimen is used to indicate the materials' toughness. In the later chapters, the test-sample specification for the two experimental methods: SHPB and Charpy, has been described.

## **1.1. Research Background**

### **1.1.1. Dynamic Impact using SHPB Testing Method**

The dynamic mechanical characteristics at a high strain rate regime for the SLM built AlSi10Mg was not reported extensively. Amir *et al.* [10] reported the dynamic response of the SLM-AlSi10Mg specimens. The specimens were prepared at two build orientations (i.e., X-direction:  $0^\circ$  and Z-direction:  $90^\circ$ ). Besides, two manufacturing techniques, such as EOS M280 and CL X line 1000R machines, were used to prepare the specimens with the same powder composition. The SHPB experiment was performed at a compressive strain rate of 700 to  $6700\text{s}^{-1}$ . In this investigation, importance was mostly imposed on the influence of the material manufacturing technique. The manufacturing technique's effect on the stress-strain behavior was not observed at strain rates of 700 to  $2800\text{s}^{-1}$ . However, different plastic deformation behavior was observed at higher than  $2800\text{s}^{-1}$ . Nurel *et al.* [11] studied the high strain rates compressive behavior of the heat-treated (T5) and as-built SLM-AlSi10Mg alloy. The range of strain rates applied for this study was from 700 to  $7900\text{s}^{-1}$ . The test specimens were also prepared at two build orientations (i.e.,  $0^\circ$  and  $90^\circ$ ). This investigation reported that the strain rate of 1000 to  $3000\text{s}^{-1}$  has no influence on the constitutive behavior. The dynamic tensile response of the SLM-AlSi10Mg at different build orientations was found in the literature. The reviewed research insists on the importance of build orientations related to the stress-strain behavior under HSR

tensile loading. However, the build orientations of  $0^\circ$  and  $90^\circ$  showed a minimal influence on the dynamic mechanical response of the SLM-AlSi10Mg under high strain rates tensile loading. The test was performed using a VISAR instrumented (VISAR-Velocity Interferometer System) for any reflector planar impact tests [12]. Maconachie *et al.* [13] performed split Hopkinson tensile bar (SHTB) tests. The authors investigated the response of SLM-AlSi10Mg at  $3.3 \times 10^{-2}$  to  $2.4 \times 10^3 \text{s}^{-1}$  tensile strain rates. The specimens were built at three different build orientations, such as  $0^\circ$ ,  $45^\circ$ , and  $90^\circ$ . Within this strain rate range, the strength of the SLM-AlSi10Mg in tension was minimally affected by the build angles. The ductility of the SLM-AlSi10Mg showed dependency on the build orientation at the quasi-static regime. The SHTB tested specimens were fractured with a surface exhibiting a distinctive fracture path for each build orientation. But the tensile strength remains insensitive to the applied loading rate.

The reviewed research indicates that the build orientation remains indifferent on the strength of the SLM-AlSi10Mg in the range of 700 to  $3000 \text{s}^{-1}$ . However, the influence of build angle (i.e., build orientation) on the strain hardening characteristics of the SLM-AlSi10Mg under high loading rate compressive conditions was not well discussed in the existing literature. Also, at the HSR compressive impact regime, the influence of the global energy density (GED) on the dynamic strain hardening of the SLM-AlSi10Mg was not found in the literature review.

Therefore, dynamic strain hardening of SLM built AlSi10Mg was investigated for build orientation and GED. The SHPB specimens were prepared at  $0^\circ$  and  $90^\circ$  build angles, 37.1, 45.4, and  $49.9 \text{J/mm}^3$  GEDs. The specimens were tested under dynamic compressive impact conditions at strain rates 800 to  $2555 \text{s}^{-1}$ .

### 1.1.2. Dynamic Impact using Charpy Testing Method

In general, the Charpy impact testing method produces strain rates of  $10^2$  to  $10^3\text{s}^{-1}$  under dynamic pendulum (-hammer) impact [14]. Under the Charpy impact loading conditions, the strain hardening behavior was not fully understood within this strain rate range.

The Charpy impact test is not designed to produce a high strain rate impact. Such an impact loading method is inefficient to have a high strain rate loading [15]. Also, the quantitative analysis of the stress wave propagation in the specimen and corresponding loading system is difficult for the jagged strain-time response [15, 16].

Tvergaard *et al.* [14] numerically analyzed the effect of strain rate and failure mechanism of CVN specimen using a material model (i.e., an elastic-viscoplastic version of the Gurson model). Many researchers applied the Charpy testing method to measure the toughness of the SLM processed AlSi10Mg specimens. It is quite frequently found in the literature that the build-orientations influence the toughness of the SLM-AlSi10Mg specimens [17, 18, 19, 20, 21]. The literature review also revealed that the specimens prepared at  $0^\circ$  build orientation have higher toughness than those with a  $90^\circ$  build angle. However, the effects of build orientations and GEDs on the strain hardening behavior of the SLM processed AlSi10Mg specimens under Charpy impact condition was not found in the literature review.

Therefore, for this work, the dynamic strain hardening behavior under Charpy impact loading condition was investigated for the SLM processed AlSi10Mg specimens. The Charpy V-notch (CVN) specimens were prepared at  $0^\circ$ ,  $90^\circ$  orientations, 37.1, 45.4, and  $49.9\text{J/mm}^3$  GEDs. The fractured surface of the specimen tested was studied under an optical-3D-digital microscope. The dynamic fracture surface was found with non-uniform fractal nature. Hence, a quantitative technique related to fractal was applied to estimate the parametric surface roughness. This roughness parameter gave an insight into the dynamic strain hardening behavior of AlSi10Mg

alloy. The quantitative fractography techniques have been discussed in the later section. It is a non-destructive technique that uses surface roughness to determine the strain hardening behavior under the Charpy impact. The surface roughness correlates with toughness, and that shows the strain hardening behavior of the SLM-AlSi10Mg specimens.

## 2. Materials and Manufacturing Method

The AlSi10Mg alloy is a hypoeutectic alloy [22]. The hypoeutectic alloy composition is mostly rich with aluminum (90 wt.%), and the aluminum solution is called primary or  $\alpha$ -Al matrix. Figure 1 shows the composition of the phases of aluminum and silicon in the phase diagram. Compared to the AlSi10Mg alloy's other chemical elements, silicon (Si) has 10 wt.%, the maximum amount after aluminum. Table I illustrates the average chemical composition used to prepare the AlSi10Mg specimens in this investigation.

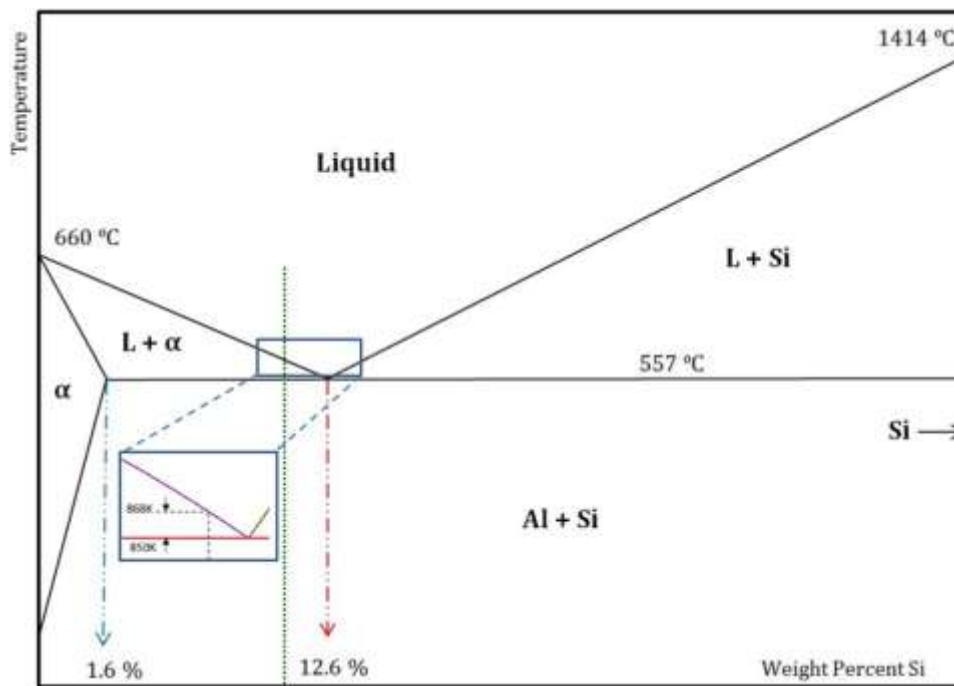


**Figure 1: An Al-Si binary phase diagram. In the diagram, the eutectic composition of silicon (Si) is 12.6 wt.% [22].**

**Table I: The AlSi10Mg alloy composition (, wt%) [23]**

Chemical Composition								
Chemical Element	Al	Si	Fe	Cu	Mn	Mg	Zn	Ti
AlSi10Mg	88.99	10.45	0.17	0.03	0.05	0.3	0.01	0.005

For this investigation, both SHPB and CVN AlSi10Mg specimens were built by the SLM method. The test-specimen geometry was obtained through CAD models from a computer. The SLM technique is a powder bed fusion based product fabrication process. The laser melts the powder and fuse layer-by-layer and builds the parts according to the CAD model. In this work, the powder particle size distribution ranges from 15.5 to 50.6 $\mu\text{m}$  for all the specimens.

In the SLM technique, a specimen is processed using multiple parameters, including hatch spacing, layer thickness, scan speed, and laser power. Global Energy Density (GED) is a derivative quantity of the processing parameters, as mentioned in equation (1). It facilitates comparing produced parts with different sets of parameters in the SLM process [24].

**Equation 1: Global energy density**

$$E_v = \frac{P}{v \cdot t \cdot h_s}$$

In this equation (1),  $E_v$  stands for GED (alternatively, volumetric energy input to the built [25]). The other parameters  $P$ ,  $h_s$ ,  $t$ , and  $v$  are the laser power input, hatch spacing is the distance between two consecutive runs of the laser beams, the thickness of the build layer, and the scanning speed of the laser, respectively.

## **2.1. Manufacturing of the Specimens**

The AlSi10Mg specimens were prepared on an additive manufacturing system, known as Electro-Optical Systems (EOS) M290. The specimens were built for both the Charpy V-notch (CVN) test and the split Hopkinson pressure bar (SHPB) experiment. There were three GED values applied to produce the specimens. A list of processing parameters of the SLM build

specimens is presented in Table II. From the list, a consistent layer thickness of 30 $\mu\text{m}$  was maintained. The hatch spacing and laser power were held the same for the GEDs of 37.1 and 45.4 J/mm<sup>3</sup>. Only the laser scan speed was varied. The laser scan speed is 1430 and 1170 for the 37.1 J/mm<sup>3</sup> GED and 45.4 J/mm<sup>3</sup> GED, respectively. The laser scan speed is 1430 and 1170 for the GEDs of 37.1 and 45.4J/mm<sup>3</sup>. For the GED of 49.9 J/mm<sup>3</sup>, all three processing parameters are different than that found for the other two GEDs: 37.1 and 45.4J/mm<sup>3</sup>. Among the three GEDs, the 49.9 J/mm<sup>3</sup> has maximum laser power of 370W. Also, it has minimum hatch spacing, and the scan speed lies between the other two GEDs. Therefore, the scan speed is the only parameter to develop the anisotropic structure, such as grains and defects of the specimens built at GEDs 37.1 and 45.4J/mm<sup>3</sup>. The anisotropy behavior affects the strain hardening of the specimens. The specimens were designed to develop at two build orientations: 0<sup>0</sup> and 90<sup>0</sup>, for the Charpy impact and SHPB experiment.

**Table II: Processing parameters of the SLM built AlSi10Mg specimens**

GED (J/mm <sup>3</sup> )	Laser power (W)	Scan Speed (mm/s)	Hatch spacing ( $\mu\text{m}$ )	Layer thickness ( $\mu\text{m}$ )
37.1	333	1430	209	30
45.4	333	1170	209	30
49.9	370	1300	190	30

## 2.2. Preparation of the Specimens

### 2.2.1. CVN Test Specimens

For the CVN test, the response of sixteen specimens in total was reported in this research. The specimens were prepared at ASTM A370 standard Charpy V-notch [26]. According to the standard, the Charpy specimen's dimension is 10 mm  $\times$  10 mm  $\times$  55 mm (Figure 2). The depth

and angle of the V-notch are 2mm and  $45^\circ$ , respectively. The V-notch was included in the Charpy specimen bar to control the fracture process. It allows concentrating the stress during the impact that occurred by the pendulum. The specimen breaks on the pendulum impact. The anvil supports the specimen resides to the same side of the V-notch. In contrast, the pendulum strikes at the opposite side of the specimen where the V-notch is located. The specimens were tested with an ASTM E23 standard Charpy impact tester [27]. The specimens were tested with a Tinius Olsen: Model IT 542 Charpy impact tester at room temperature.

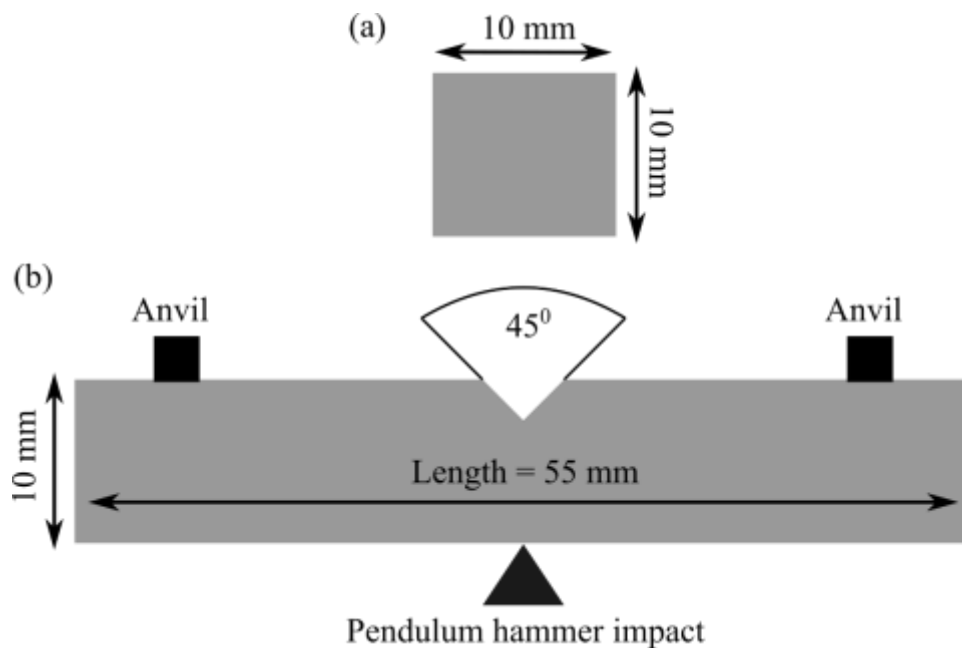


**Figure 2: Schematic diagram of standardized Charpy V-notch specimen: (a) surface in the transverse direction where the area of the surface is 10 mm × 10 mm and (b) surface in the longitudinal direction where the surface area is 10 mm × 55 mm.**

The build orientations of the CVN specimen is presented in Figure 3. In the diagram, the building direction lies along the z-axis. For the  $90^\circ$  build specimen, the building direction is orthogonal to the layer orientation (i.e., build angle) of the test specimen. On the other side, the

$0^\circ$  angle exists between the building direction (axis) and the layer direction for the  $0^\circ$  build orientation. The longitudinal length was 55 mm along the z-axis when the specimen was built at  $90^\circ$ . The  $0^\circ$  build specimen, in contrast, has a transverse height of 10 mm along the z-axis. Therefore, for the  $90^\circ$  build specimen, the pendulum impact axis was developed parallel to the layer orientation. In comparison, the  $0^\circ$  specimen has a perpendicular impact loading axis.

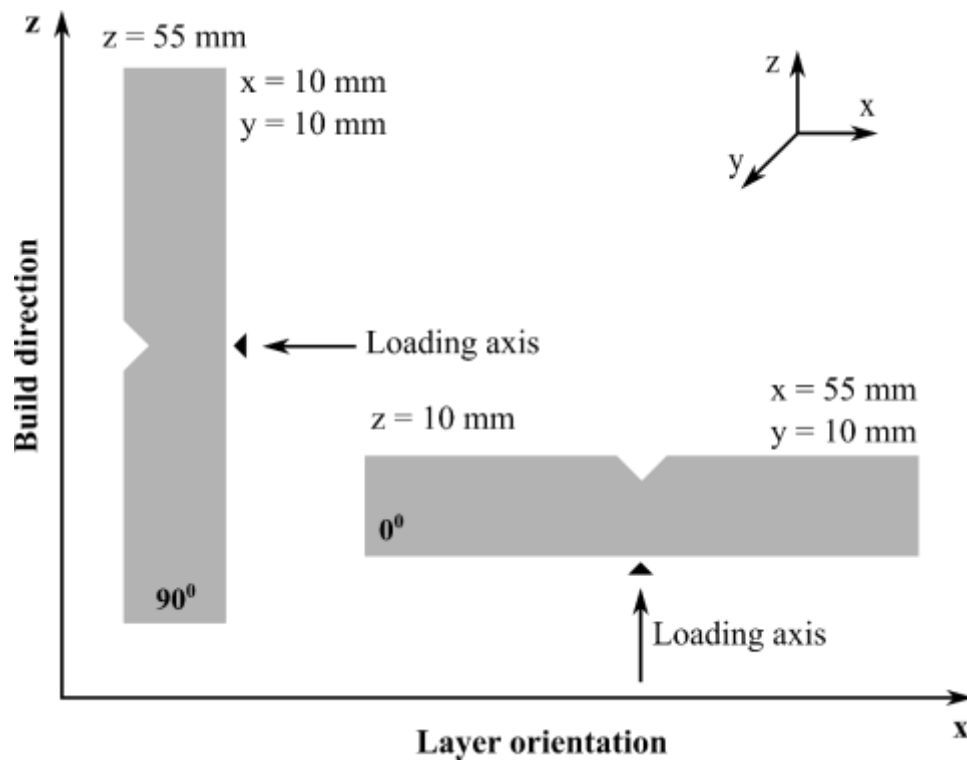


Figure 3: A schematic diagram of the build orientation of the CVN specimen. A black arrow ( $\blacktriangle$ ) indicates the location of the pendulum impact that occurs in the test specimen.

### 2.2.2. SHPB Specimens

The design of a specific SHPB experiment essentially relies on the specification of the specimen (i.e., the length,  $l_0$ , and diameter,  $d_0$  of the test specimen [7]). Other apparatus specifications are the length,  $L$ , and diameter,  $D$  of the incident, and transmission bar. The

experimental design, therefore, is followed by considering the following ratios:  $L/D$ ,  $D/d_0$ , and  $l_0/d_0$ . Typically, the value of  $L/D$  is considered as an order of 100,  $D/d_0$  is of the order of 2 to 4, and  $l_0/d_0$  is 0.6 to 1 [8]. In this investigation, all the ratios (i.e.,  $L/D$ ,  $D/d_0$ , and  $l_0/d_0$ ) of the SHPB experiment are presented in Table III. The materials of the incident, transmission, and striker bars were C350 maraging steel. The SHPB experiment was conducted on a REL split Hopkinson pressure bar assembly at room temperature.

**Table III: Design parameters of the bars of the SHPB experiment [28]**

Parameter	Bar (in)	Specimen (mm)	$L/D$	$D/d_0$	$l_0/d_0$
Length	$L = 72$	$l_0 = 9.5 \text{ mm (or } 0.37 \text{ in)}$	96	2	1
Diameter	$D = 0.72$	$d_0 = 9.5 \text{ mm (or } 0.37 \text{ in)}$			

The specimen's average size is; length:  $9.50 \text{ mm} \pm 0.017$  and diameter:  $9.50 \text{ mm} \pm 0.012$ . The average mass of the test specimens is  $1.78 \text{ gm} \pm 0.007$ . Figure 4 schematically presents the diagram of the SHPB specimen.

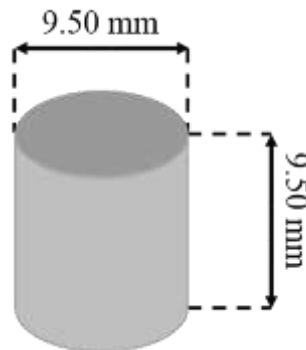


**Figure 4: A SHPB specimen is cylindrical in shape. It has a diameter and height, both are 9.50 mm (or 0.37 in).**

The build orientations of the SHPB specimens are presented in Figure 5. The impact loading axis is parallel to the build direction for the  $90^\circ$  build specimen, whereas it is perpendicular for the  $0^\circ$  specimen,

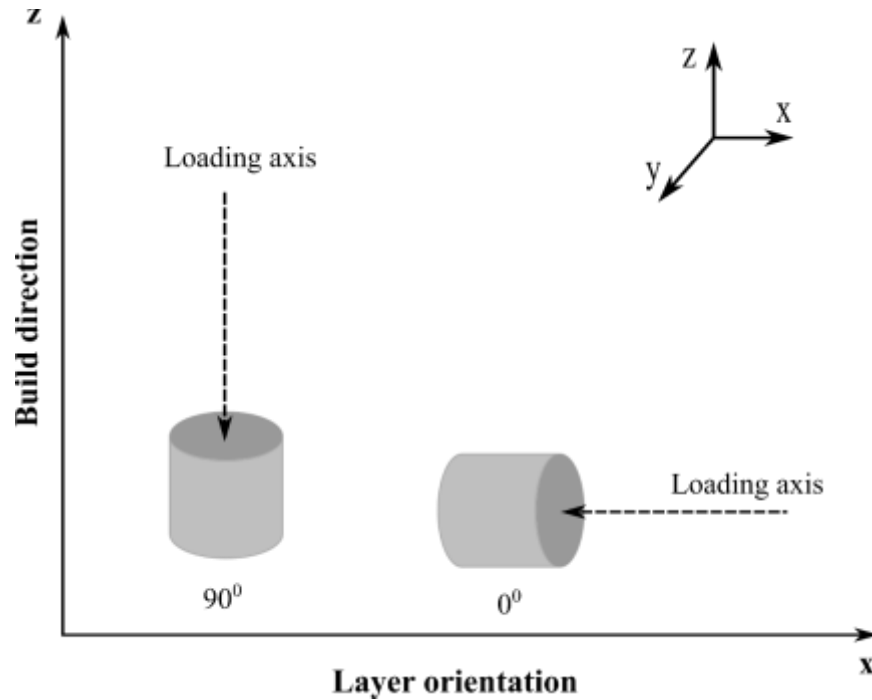


Figure 5: A schematic diagram of the build orientation of the SHPB specimens is presented.

### 2.3. Statistical Analysis

The statistical significance of the data obtained from the SHPB and Charpy impact experiment was evaluated using 'Student's T-test' (also called 'T-test'). An unpaired and two-tailed T-test was used to calculate the significant difference of the mechanical behavior for build orientations and GEDs of the specimens. The T-test was performed using Microsoft Excel 2013 in-built software package for the T-test. A confidence limit of  $\leq 95\%$  and the probability of  $P < 0.05$  were

reported as statistically significant, and below 95% was marked as 'Not significant (NS).' Such type of statistical analysis method was applied by researchers for a variety of fields [29, 30]. Fazio *et al.* [29] used an unpaired type of 'Student's T-test' for evaluating the statistical significance of chemical elements, such as Cadmium, Mercury, and Lead, in the water and sediment of two lakes. Newman *et al.* [30] used this method for determining statistical significance in the computed tomography data for healthy and asthmatic subjects. In this dissertation, the T-test was performed for two build orientations of 0° and 90°, and for three GEDs of 37.1, 45.4, and 49.9 J/mm<sup>3</sup>.

### 3. Strain Hardening Behavior: Split Hopkinson Pressure Bar Experiment

The dynamic strain hardening behavior of the SLM built AlSi10Mg specimens was determined by the split Hopkinson pressure bar (SHPB) experiments. The compressive impact loadings were applied to deform the SHPB specimen at a high strain rate (HSR). The experiments were performed at strain rates of 800 to 2555s<sup>-1</sup>. The distribution of the test strain rates applied in different SHPB specimens is shown in Figure 6.

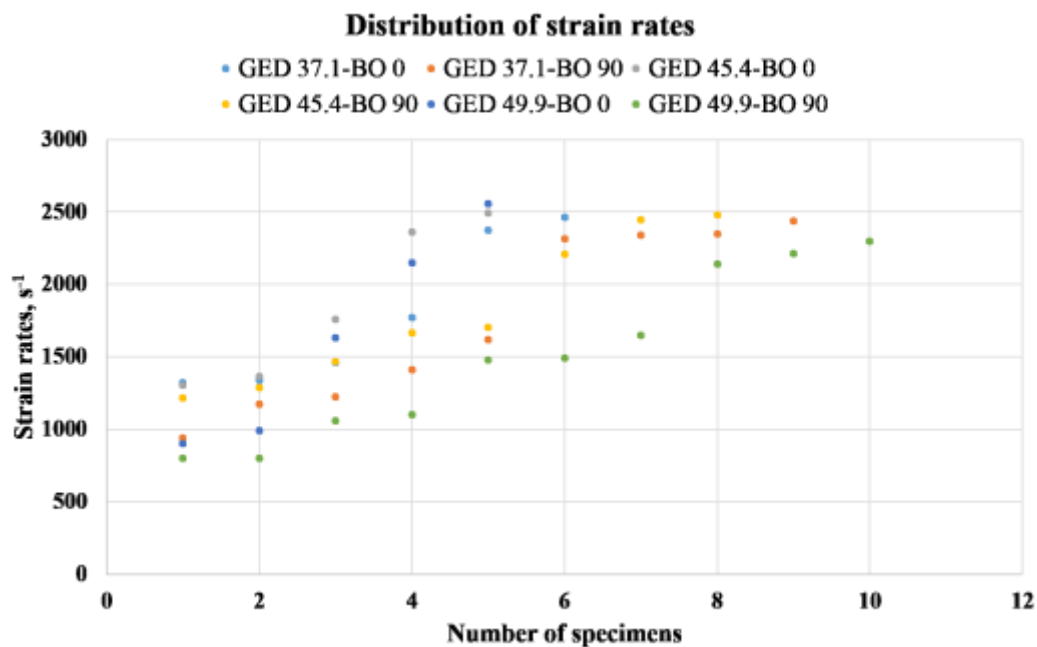
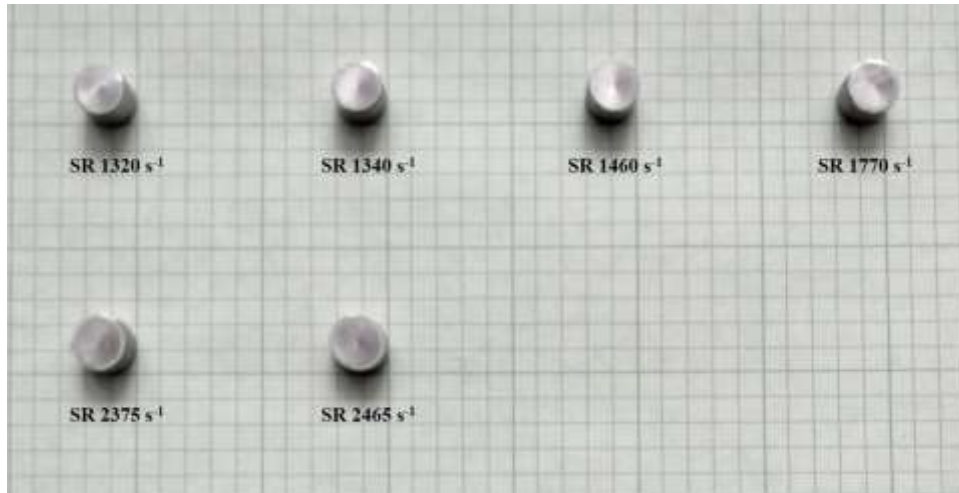


**Figure 6: Distribution of the strain rates with multiple specimens reported for the SHPB experiment**

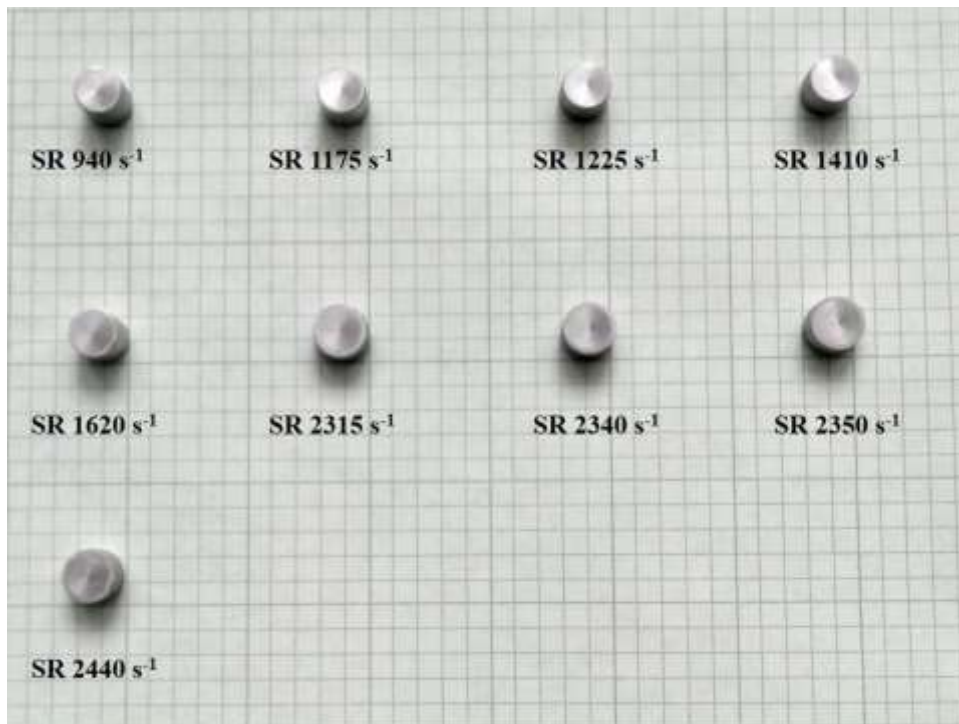
The pictures of all the tested specimens are reported in Figure 7. For GED of 37.1J/mm<sup>3</sup> and 0° build specimens, the tested strain rates were 1320 to 2465s<sup>-1</sup> (Figure 7a). Figure 7b presents the test specimens prepared at GED of 37.1J/mm<sup>3</sup> and 90° and tested at strain rates of 940 to 2440s<sup>-1</sup>. For GED of 45.4J/mm<sup>3</sup>, the strain rates for the 0° and 90° specimens were 1305

to  $2495\text{s}^{-1}$  (Figure 7c) and  $1215$  to  $2480\text{s}^{-1}$  (Figure 7d), respectively. The GED of  $49.9\text{J}/\text{mm}^3$  of the  $0^\circ$  and  $90^\circ$  specimens have loading rates of  $900$  to  $2555\text{s}^{-1}$  (Figure 7e) and  $800$  to  $2300\text{s}^{-1}$  (Figure 7f).

(a)



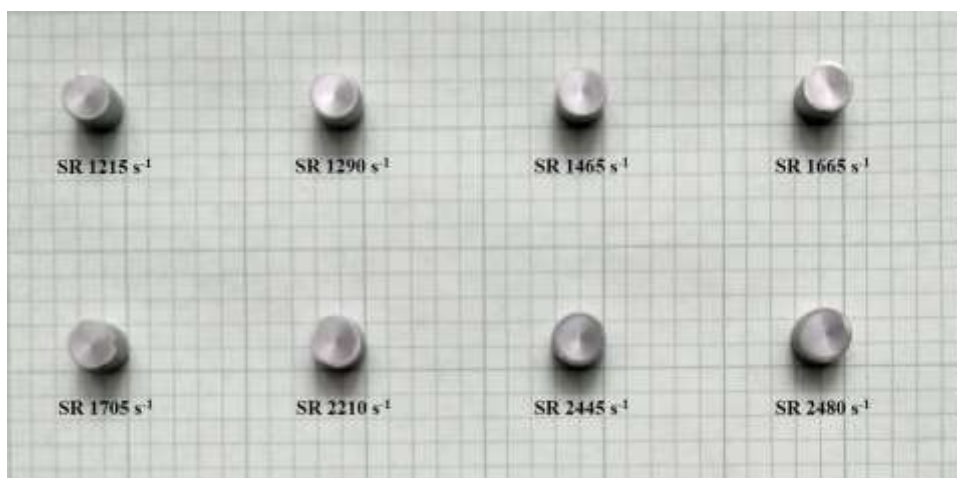
(b)



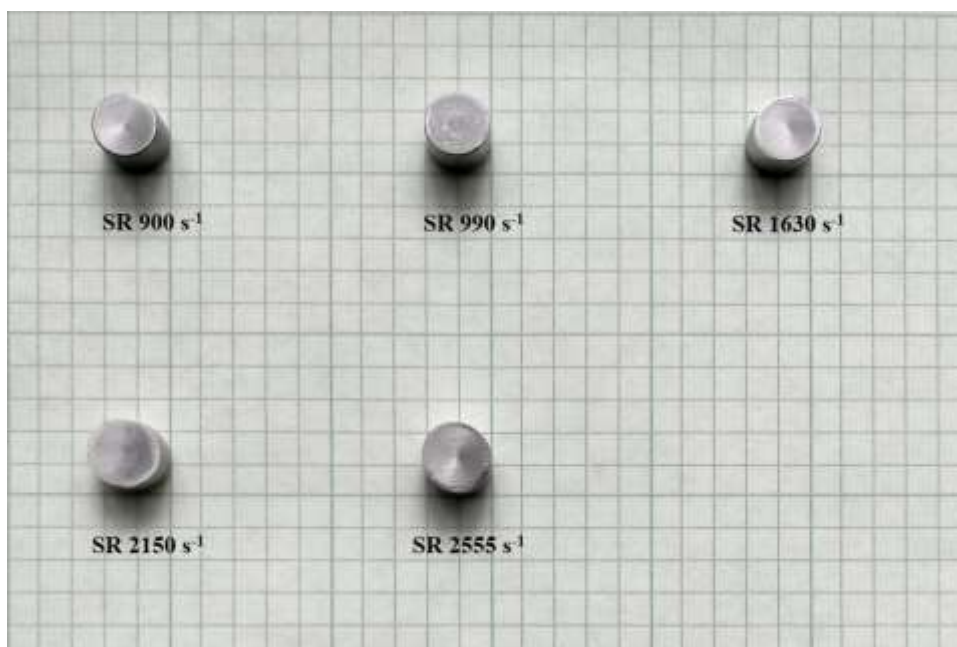
(c)



(d)



(e)



(f)

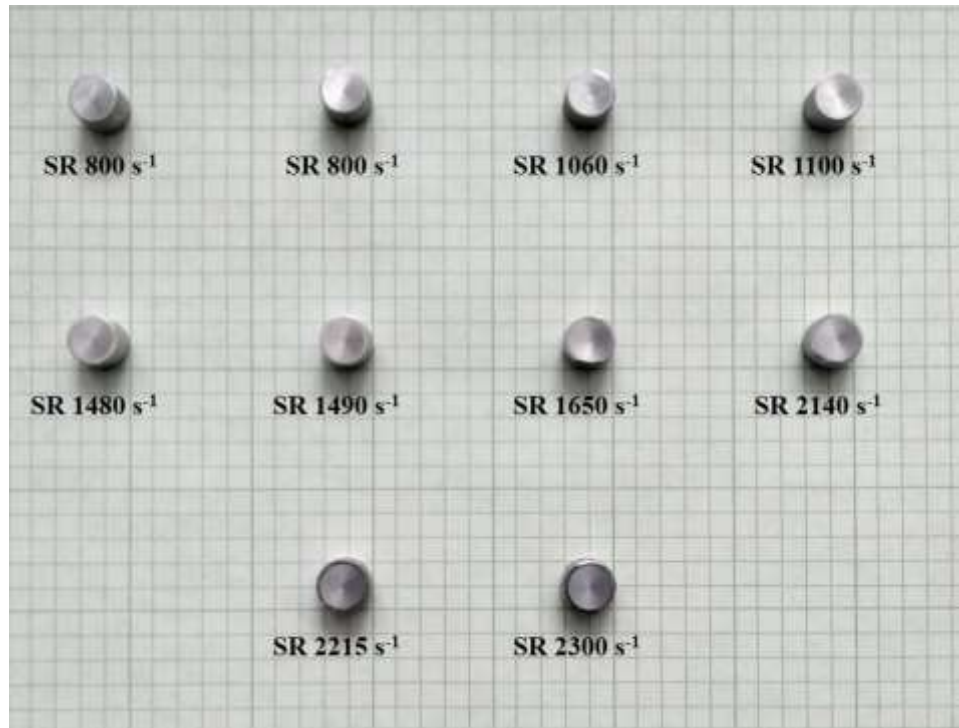


**Figure 7: Split Hopkinson Pressure Bar (SHPB) tested specimens: (a) GED of  $37.1\text{J/mm}^3$  and build at  $0^\circ$ , (b) GED of  $37.1\text{J/mm}^3$  and build at  $90^\circ$ , (c) GED of  $45.4\text{J/mm}^3$  and build at  $0^\circ$ , (d) GED of  $45.4\text{J/mm}^3$  and build at  $90^\circ$ , (e) GED of  $49.9\text{J/mm}^3$  and build at  $0^\circ$ , and (f) GED of  $49.9\text{J/mm}^3$  and build at  $90^\circ$ .**

### 3.1. SHPB Data Analysis

The basic concept of the SHPB experimental design is presented in Figure 8. In the diagram, two bars are shown, called incident and transmission bars. The bars are cylindrical rods. A cylindrical specimen is placed like a sandwich between the two bars as all three remain axially aligned. An external impact (Figure 8) is subjected by a striker bar (Figure 9) at the incident bar end. Hence, the axial impact develops a stress pulse in the incident bar. The stress pulse transmits into the specimen and passes through the transmission bar. A part of the stress wave returns from the specimen interfaces back to the incident bar.

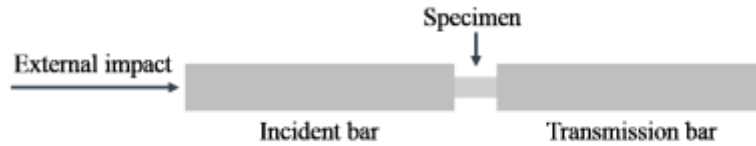


**Figure 8: A simple schematic diagram of the Split Hopkinson Pressure Bar apparatus.**

Figure 9 represents the SHPB experiment setup that is capable of capturing stress wave response at HSR impact. In the diagram, two strain gauges: A and B, are shown, installed at the cylindrical surfaces of the incident bar and transmission bar. The strain gauge 'A' (Figure 9) records incident-pulse (in terms of surface strain) and reflected-pulse. The strain gauge 'B' (Figure 9) records the transmitted pulse in the transmission bar. Three pulses (i.e., incident pulse, reflected pulse, and transmitted pulse) are conditioned and amplified by a signal conditioning amplifier and record in the oscilloscope. The data are analyzed by using elastic wave theory mentioned in the later section.

The specimens for the SHPB experiment are smaller in size. Because to reduce the radial inertia effects. Theoretically, the radial inertia changes with the specimen's squared radius. It indicates that a narrow test-specimen is useful for eliminating the radial inertia effect [7].

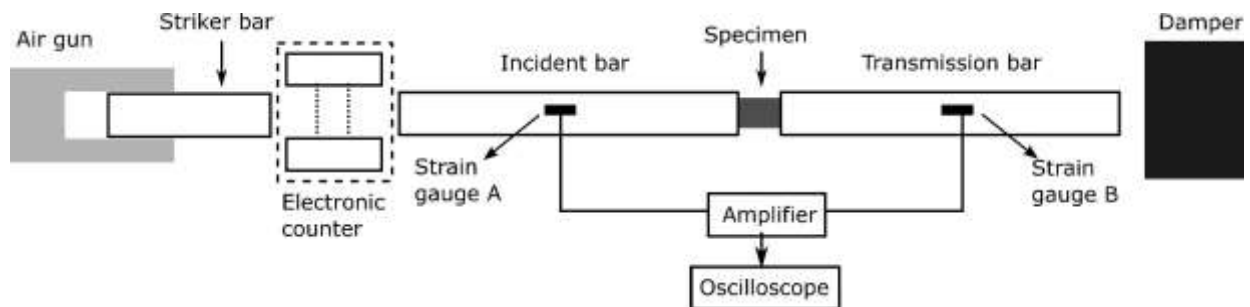


**Figure 9: Schematic diagram of the SHPB experiment [31]**

The corresponding incident bar pulses (i.e., two blue-color pulses) and transmission bar pulse (i.e., orange color pulse) are presented in Figure 10. In the compressive SHPB experiment, the striker bar whacks the incident bar. Hence, it sends a stress pulse that moves through on the incident bar. Upon the arrival of the incident pulse at the other end of the incident bar, a part of the incident pulse (compression pulse) returns to the incident bar as a reflected pulse (tensile pulse). The rest of the incident pulse remains compressive and continues moving into the specimen and then through the transmission bar. Similar transmission and reflection of the pulse occur at both sides of the test-specimen. Since the impedance of the SHPB is designed higher than the test-specimen, the reflected pulses within the test-specimen remain compressive. The compressive pulse reverberates within the specimen. It increases the compressive stress level up, and hence specimen deformation occurs at a high strain rate. This procedure takes a few micro-seconds to equilibrate the stress state within the specimen.

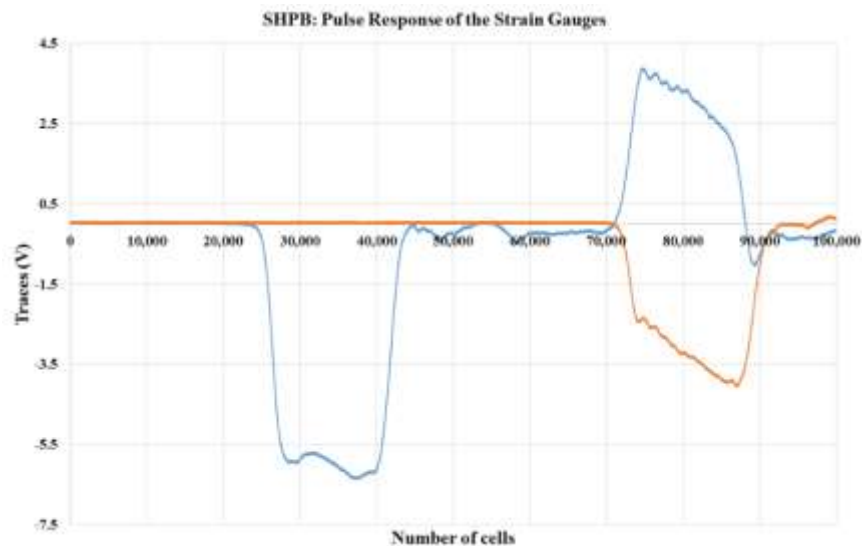


**Figure 10: Typical incident and transmission bar pulses of the SHPB experiment. The incident bar pulses are marked with a “blue” color, and the transmission bar pulse is marked with an “orange” color.**

Once the equilibrium stress condition is established (i.e., both interfaces of the specimen experiences the same pressure), the corresponding strains of the wave pulses can be written as:

$$\varepsilon_I + \varepsilon_R = \varepsilon_T$$

In the above equation,  $\varepsilon_I$  is the incident pulse,  $\varepsilon_R$  is the reflected pulse, and  $\varepsilon_T$  is the transmitted pulses.

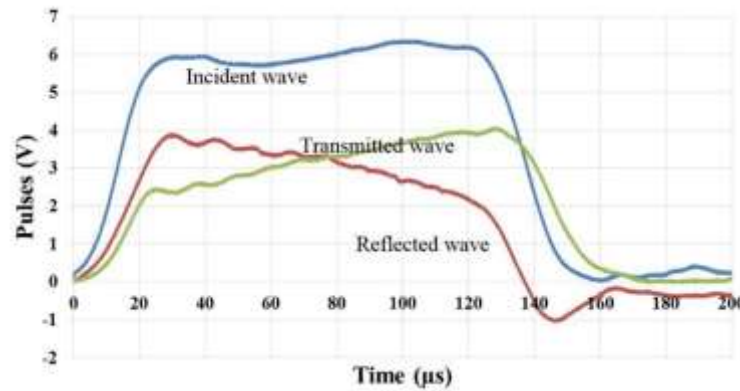


**Figure 11: The incident pulse is in blue, the reflected pulse is in red, and the transmitted pulse is in green. An incident bar pulse is a combination of reflected and transmitted wave pulses.**

The stress-strain and related strain rate behavior must be determined from the SHPB pulses to get the specimens' strain hardening behavior. The reflected wave pulse,  $\varepsilon_R$  is used to obtain a normal strain rate,  $\dot{\varepsilon}_s$  which is presented by equation (2).

**Equation 2: Normal strain rate**

$$\dot{\epsilon}_s(t) = -\frac{2c_b}{l_0} \epsilon_R$$

In the above equation (2),  $c_b$  ( $= E_b/\rho_b$ ) is stress wave speed in the SHPB. The  $E_b$  and  $\rho_b$  are the corresponding elastic modulus and density. The initial specimen length is presented by  $l_0$ . This negative sign is used because the strain due to the reflected pulse is tensile. In contrast, the strain response is due to the incident pulse. Since the HSR test is compressive. The compressive strain rate (equation (2)) is positive.

The nominal strain is estimated using the strain rate of the above equation over time,  $t$

**Equation 3: Normal strain**

$$e_s(t) = \int_0^t \dot{\epsilon}_s(\tau) d\tau$$

The nominal stress is evaluated from the transmitted pulse. [8].

**Equation 4: Normal stress**

$$s_s(t) = \frac{E_b A_b}{A_s} \epsilon_T(t)$$

In equation (4),  $A_s$ - the area of the cross-section for the pristine specimen is  $A_b$ , whereas  $A_b$  is the cross-section area of the SHPB.

The true strain,  $\varepsilon_s$  and true strain rate,  $\dot{\varepsilon}_s$  are determined by equation (5) and (6)

**Equation 5: True strain**

$$\varepsilon_s(t) = -\ln[1 - e_s(t)]$$

**Equation 6: True strain rate**

$$\dot{\varepsilon}_s(t) = \frac{\dot{e}_s(t)}{1 - e_s(t)}$$

It was assumed that the compression is positive for the compressive SHPB experiment.

The true stress,  $\sigma_s$  is obtained as,

**Equation 7: True stress**

$$\sigma_s(t) = s_s(t)[1 - e_s(t)]$$

The energy-absorbing capacity (E) of a specimen is defined by the equation (8) [32]. The equation describes the amount of energy requires to deform a specimen per unit volume. The absorbed energy is determined as the integral over the area of the corresponding stress-strain curve.

**Equation 8: Energy absorption capacity**

$$E = \int_0^{ut} \sigma(\varepsilon) d\varepsilon$$

In this equation, ‘ $ut$ ’ is for the ultimate strain on the stress-strain curve. The  $\sigma$  and  $\varepsilon$  are the stress and strain, respectively.

In the SHPB experiment, a sudden temperature rise occurs in the SHPB specimen due to the bar to specimen impact. The plastic deformation is transformed into an adiabatic temperature rise in the SHPB specimen [33]. The adiabatic temperature rise is evaluated by equation (9) [34].

**Equation 9: Adiabatic temperature rise**

$$\Delta T = \frac{\beta}{\rho c} \int \sigma(\varepsilon_p) d\varepsilon_p$$

The temperature rise ( $\Delta T$ ) during the adiabatic heating occurs for the plastic deformation of the specimen. A coefficient that indicates the proportion of the work for plastic deformation transformed into heat is denoted by  $\beta$ . Typically, most of the plastic work is assumed to be converted into heat such that  $\beta$  lies between 0.9 and 1. Berkovic *et al.* [34] calculated the adiabatic temperature rise of the SHPB experiment on aluminum alloy with a value for  $\beta = 0.95$ . Similarly, for simplicity and comparison purposes about the temperature rise at build orientations and GEDs, the value of  $\beta = 0.95$  was considered for this work. The mass density and specific heat are denoted by  $\rho$  and  $c$ , respectively. The value for the specific heat,  $c$  of the SLM-ALSi10Mg was taken as 875 J/kgK [35].

### 3.2. Maximum Flow Stress

Maximum flow stress was determined to understand plastic deformation behavior under the high strain rate impact. Typically, the increment of strain and strain-rate increases the true flow stress. However, the flow stress decreases for the adiabatic heating. It provides a self-acceleration to the strain localization or adiabatic shear banding [36]. The average adiabatic heating behavior is presented in the next sections.

An average of maximum flow stress was evaluated for all the specimens at each build orientation and presented in a bar chart in Figure 12. The standard deviation from the average value was given by error bars in the bar chart.

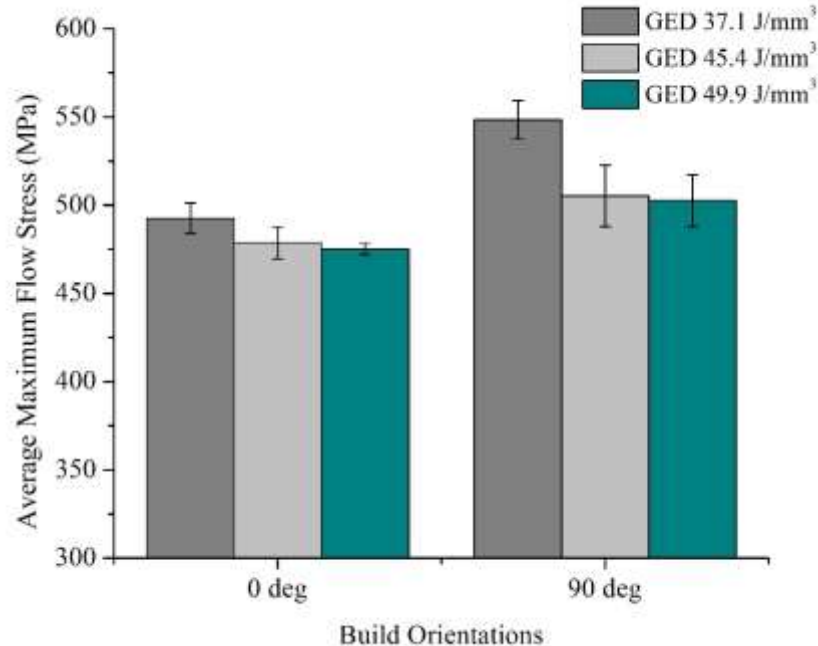


**Figure 12:** The average maximum flow stress of the SHPB specimens tested at a range of strain rates. The standard deviation of the data is shown using error bars.

### 3.2.1. Statistical Significance: Maximum Flow Stress

The significant difference between build orientations and GEDs was evaluated using the student's T-test for the maximum flow stress presented in Table V (and the statistical sample size in Table IV). It was observed that the GEDs of 37.1 and 49.9J/mm<sup>3</sup> for both orientations: 0° and 90°, the maximum flow stress does not have a significant difference. For the remaining comparison at build orientations with GEDs, the maximum flow stresses have a significant difference.

**Table IV: Maximum flow stress: the statistical sample size for the 'student's T-test'**

GEDs & BOs	Statistical sample size	
	0°	90°
GED 37.1J/mm <sup>3</sup>	5	10
GED 45.4J/mm <sup>3</sup>	6	9
GED 49.9J/mm <sup>3</sup>	5	8

**Table V: Student's T-test for the maximum flow stress**

GEDs & BOs	Probability, P	Confidence limit (%)
GED 37.1: 0° & 90°	P = 0.0003	99.97
GED 45.4: 0° & 90°	P = 2.2×10 <sup>-7</sup>	100.00
GED 49.9: 0° & 90°	P = 0.0065	99.35
Build 0°: 37.1 & 45.4	P = 0.0046	99.54
Build 0°: 37.1 & 49.9	P > 0.05	Not significant
Build 0°: 45.4 & 49.9	P = 0.0224	95.51
Build 90°: 37.1 & 45.4	P = 1.3×10 <sup>-6</sup>	100.00
Build 90°: 37.1 & 49.9	P > 0.05	Not significant
Build 90°: 45.4 & 49.9	P = 0.0001	99.99

### 3.3. Energy Absorption Behavior

The energy absorption capacity under the high strain rate impact was determined by using equation (8). Figure 13 shows the average response for all the specimens at each build

orientation. The error bars represent the standard deviation from the average. It shows that the 90° build specimens absorbed marginally higher energy.

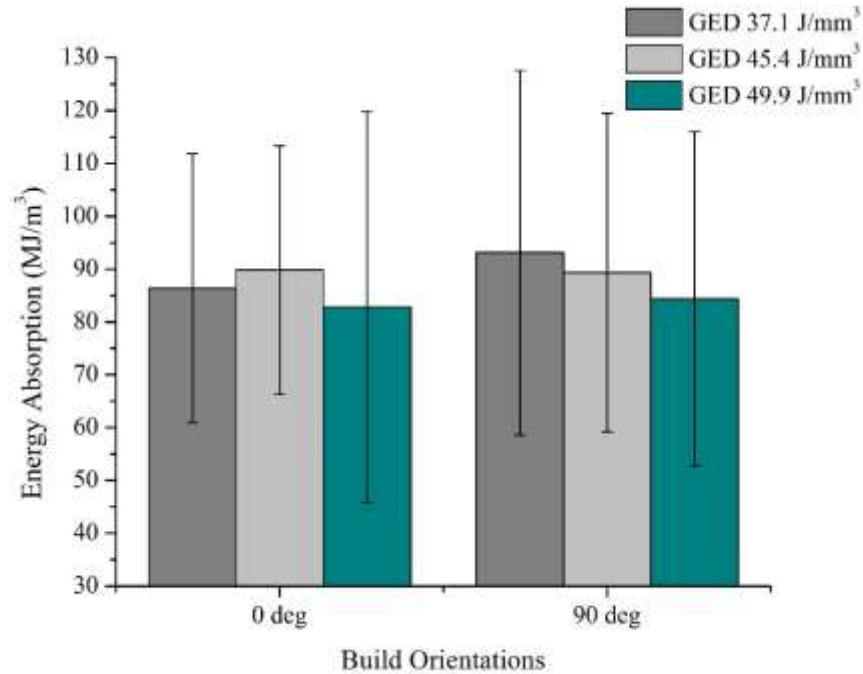


**Figure 13: The average energy absorption capacity of the SHPB specimens tested at a range of strain rates. The standard deviation of the data is shown using error bars.**

### 3.3.1. Statistical Significance: Energy Absorption Behavior

The ‘student’s T-test’ was applied for evaluating the ‘statistical significance’ (Table VII and the statistical sample size in Table VI) of specimens’ energy absorption behavior under high strain-rate deformation. None of the comparisons show the energy absorption behavior at two build orientations: 0° and 90°, even three GEDs of 37.1, 45.4, and 49.9J/mm<sup>3</sup> are different.

**Table VI: Energy absorption behavior: the statistical sample size for the ‘student’s T-test’**

GEDs & BOs	Statistical sample size	
	0°	90°
GED 37.1J/mm <sup>3</sup>	5	10
GED 45.4J/mm <sup>3</sup>	6	9
GED 49.9J/mm <sup>3</sup>	5	8

**Table VII: Student’s T-test for energy absorption behavior**

GEDs & BOs	Probability, P	Confidence limit (%)
GED 37.1: 0° & 90°	P > 0.05	Not significant
GED 45.4: 0° & 90°	P > 0.05	Not significant
GED 49.9: 0° & 90°	P > 0.05	Not significant
Build 0°: 37.1 & 45.4	P > 0.05	Not significant
Build 0°: 37.1 & 49.9	P > 0.05	Not significant
Build 0°: 45.4 & 49.9	P > 0.05	Not significant
Build 90°: 37.1 & 45.4	P > 0.05	Not significant
Build 90°: 37.1 & 49.9	P > 0.05	Not significant
Build 90°: 45.4 & 49.9	P > 0.05	Not significant

### 3.4. Temperature Rise in Adiabatic Heating

The adiabatic temperature rise was evaluated by using equation (9). The average temperature for the adiabatic heating is presented in Figure 14. The average was calculated for all the specimens for each build orientations. The error bars are the standard deviation from the average of adiabatic heating values.

An apparently observed trend may be reported here that the average temperature rise for adiabatic heating was higher for the 90° specimens for the three GEDs. For each build orientation, the 90° build specimens experienced a higher temperature rise than the 0° build specimens.

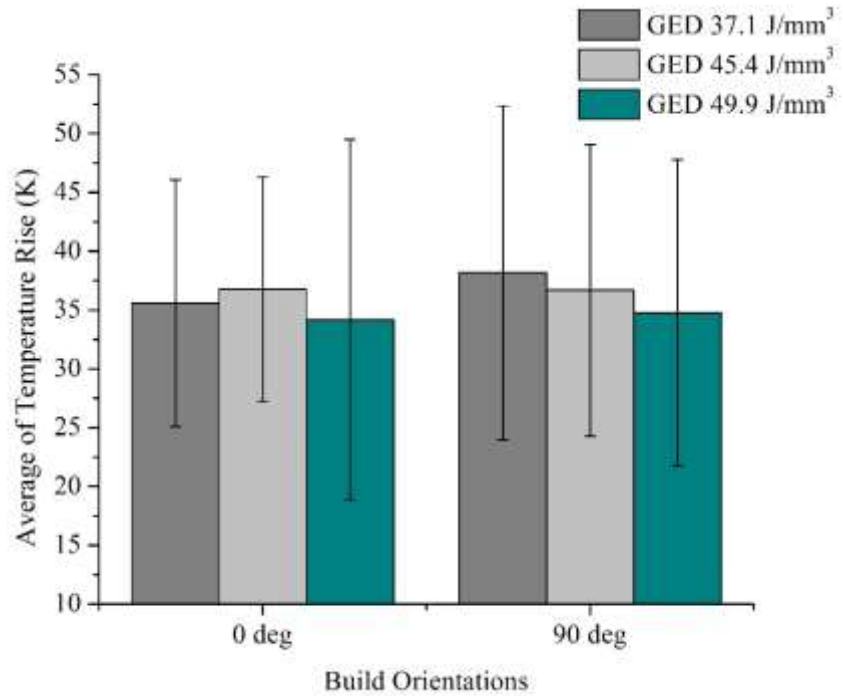


**Figure 14:** The average adiabatic temperature rise of the SHPB specimens tested at a range of strain rates. The standard deviation of the data is shown here using error bars.

### 3.4.1. Statistical Significance: Adiabatic Temperature Rise

The ‘student’s T-test’ compared the test-data (Table IX and the statistical sample size in Table VIII) and reported that none of the adiabatic temperature rise at two build orientations: 0° and 90°, and three GEDs of 37.1, 45.4, and 49.9J/mm<sup>3</sup> are significantly different.

**Table VIII:** Adiabatic temperature rise: the statistical sample size for the ‘student’s T-test’

GEDs & BOs	Statistical sample size	
	0°	90°
GED 37.1J/mm <sup>3</sup>	5	10
GED 45.4J/mm <sup>3</sup>	6	9
GED 49.9J/mm <sup>3</sup>	5	8

**Table IX: Student's T-test for the adiabatic temperature rise**

<b>GEDs &amp; BOs</b>	<b>Probability, P</b>	<b>Confidence limit (%)</b>
<b>GED 37.1: 0° &amp; 90°</b>	P > 0.05	Not significant
<b>GED 45.4: 0° &amp; 90°</b>	P > 0.05	Not significant
<b>GED 49.9: 0° &amp; 90°</b>	P > 0.05	Not significant
<b>Build 0°: 37.1 &amp; 45.4</b>	P > 0.05	Not significant
<b>Build 0°: 37.1 &amp; 49.9</b>	P > 0.05	Not significant
<b>Build 0°: 45.4 &amp; 49.9</b>	P > 0.05	Not significant
<b>Build 90°: 37.1 &amp; 45.4</b>	P > 0.05	Not significant
<b>Build 90°: 37.1 &amp; 49.9</b>	P > 0.05	Not significant
<b>Build 90°: 45.4 &amp; 49.9</b>	P > 0.05	Not significant

### 3.5. Development of Shear Plane

The surface of the SHPB post-specimen was investigated. The attempt was taken to see any shear plane by using a digital microscope at 300x magnification. An average of 8 images was developed on an entire specimen surface at 300x magnification with a digital microscope.

The development of a shear band is a localized phenomenon and defined as thermo-viscoplastic instabilities. It occurs in metals and alloys at considerable strain rate deformation, such as in ballistic impact and penetration. Such a kind of phenomenon is also observed in the high strain rate regime [37, 38]. A localized shearing can occur at the high strain rate deformation, leading to a localized deformation and corresponding heat generation. The type of shear band varies with deformation concentration, such as deformation bands and transformation bands [36].

It was observed that the shear plane was not found in any of the specimens. Figure 15 shows that no shear plane was observed on the test SHPB specimen's surface. The test specimen in Figure 20 was built at 90° build orientation and GED of 37.1J/mm<sup>3</sup>. It was tested at a 2315s<sup>-1</sup> strain rate and induced with maximum flow stress of 557.46MPa.

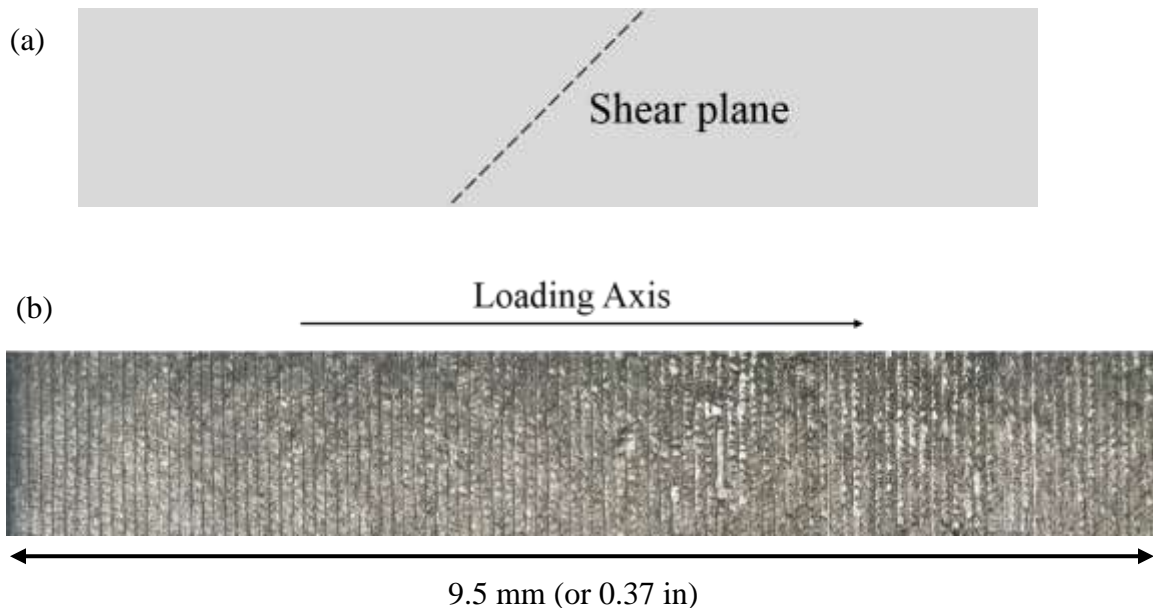


**Figure 15: Investigating the development of the shear plane of the tested SHPB specimen: (a) schematic diagram of the shear plane and (b) SHPB tested specimen where no shear plane was observed.**

### 3.6. Strain Hardening Behavior

The maximum flow stress versus logarithmic strain rate plots (Figure 16, 17, and 18) show the strain hardening behavior under a high rate of compressive loading. It was found that the 90° build specimens experienced higher maximum flow stress than that the 0° build specimens experienced. The maximum flow stress demonstrated a decremental trend with the increasing GED. It was observed that the GED of 49.9J/mm<sup>3</sup> faced a minimum value for the flow stress than the other two GEDs of 37.1 and 45.4J/mm<sup>3</sup>.

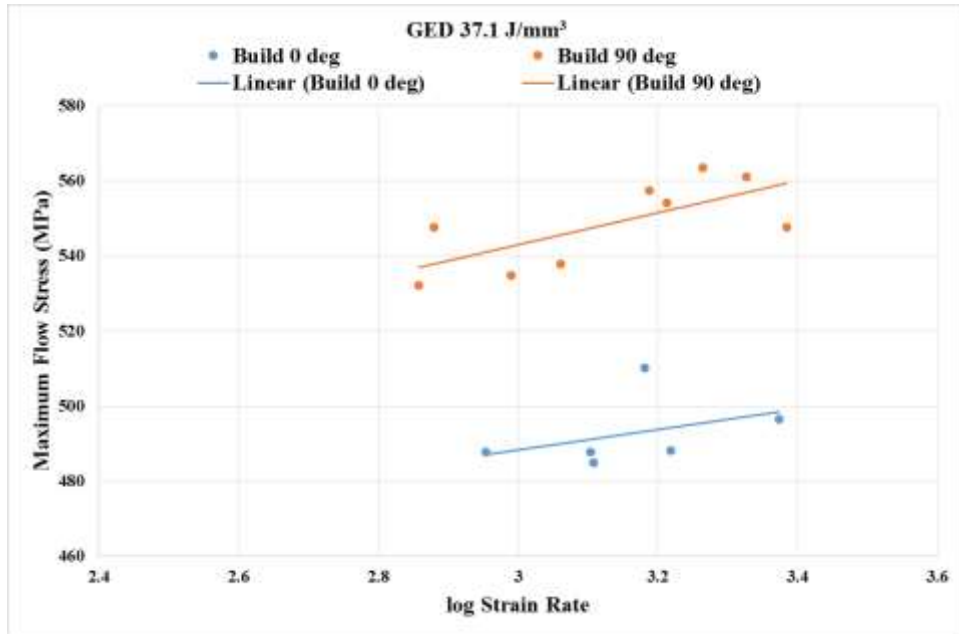


Figure 16: Strain hardening behavior of the specimens built at a GED of 37.1J/mm<sup>3</sup> and two build orientations: 0° and 90°.

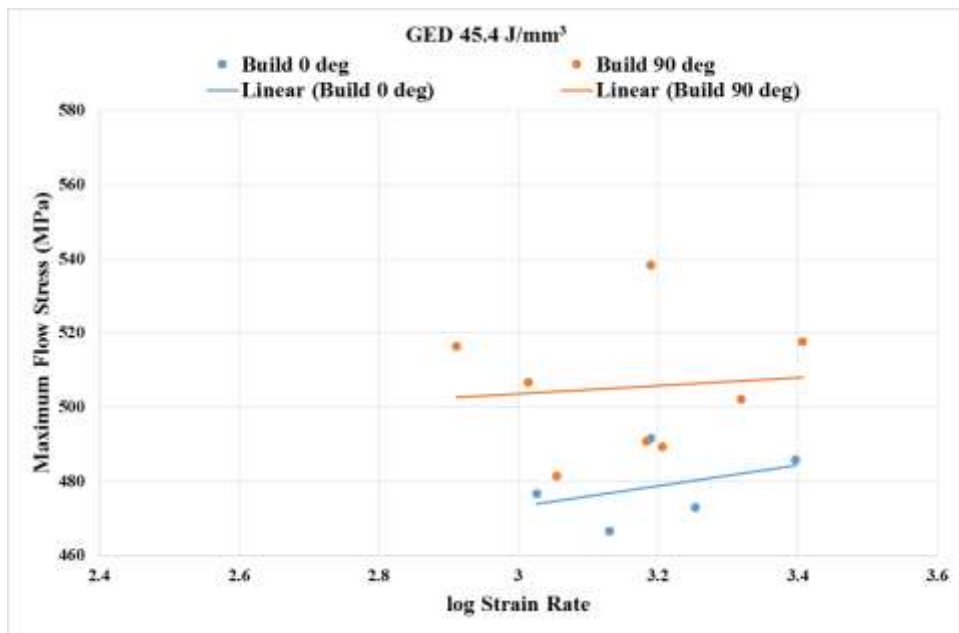


Figure 17: Strain hardening behavior of the specimens built at a GED of 45.4J/mm<sup>3</sup> and two build orientations: 0° and 90°.

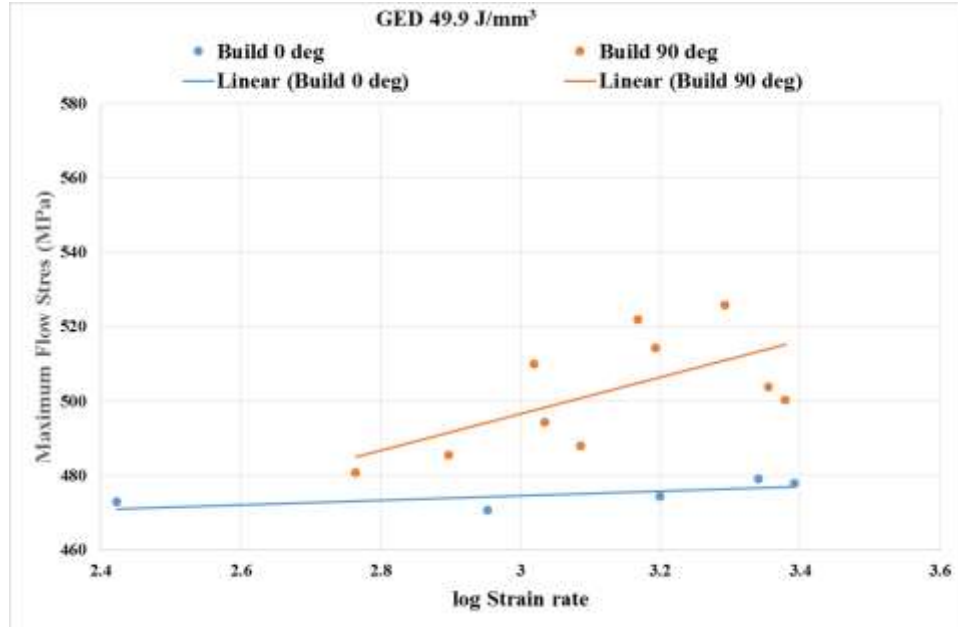


Figure 18: Strain hardening behavior of the specimens built at a GED of 49.9J/mm<sup>3</sup> and two build orientations: 0° and 90°.

### 3.7. Observation

The dynamic mechanical behavior of SLM-AlSi10Mg under compressive loading was investigated at three GEDs and two build orientations. The results are not conclusive.

A trend was observed within limited and available data for the strain hardening behavior of the SLM processed AlSi10Mg under HSR dynamic loading conditions and reported here.

#### 3.7.1. Effects of Build Orientation on Strain Hardening Behavior

- At more than 95% confidence limit, the average max flow stress was higher for 90° specimens.
- The average energy absorption for deforming the specimens was not significantly different for 0° and 90° build specimens.

- Similarly, the average adiabatic temperature rise for the deformed specimen under HSR conditions are not statistically different at 0° and 90° build orientations. The evolution of adiabatic temperature is responsible for softening the materials.
- As the strain rate increased, it was observed that 0° specimens experienced lower max flow stress than the 90° specimens consistently.

The strain hardening behavior (i.e., at more than 95% confidence limit, the maximum flow stress with build orientations) was influenced for the build orientations. Still, the energy absorption and adiabatic temperature rise were not significantly different at build orientations: 0° and 90°.

### **3.7.2. Effects of GED on Strain Hardening Behavior**

- At more than 95% confidence limit, the average maximum flow stress is different for the GED of 45.4 and 49.9J/mm<sup>3</sup>. But for the GED of 37.1 and 49.9J/mm<sup>3</sup>, the average of the maximum flow stress was not different. A trend was also observed that may be reported here that the maximum flow stress was lower for the higher GED specimens. The test specimens were built at a GED of 49.9J/mm<sup>3</sup> with lower maximum flow stress than the GED of 37.1J/mm<sup>3</sup>.
- The average energy absorption behavior was not statistically significant for the GEDs of 37.1, 45.4, and 49.9J/mm<sup>3</sup>.
- The rise of the adiabatic temperature was not significantly different for the GEDs of 37.1, 45.4, and 49.9J/mm<sup>3</sup>.

Therefore, at more than 95% confidence limit, the strain hardening behavior under HSR dynamic impact was influenced by the GEDs of 45.4J/mm<sup>3</sup> and 49.9J/mm<sup>3</sup>. The energy

absorption and adiabatic temperature rise were not statistically different for the GEDs of 37.1, 45.4, and 49.9J/mm<sup>3</sup>.

### **3.8. Future Research**

For statistical analysis, a statistical sample size of more than 10 may provide good statistical significance. Therefore, it may be recommended to test more specimens for the same GEDs and build orientations.

#### 4. Strain Hardening Behavior: Charpy Impact Test

In this chapter, the strain hardening behavior of SLM built AlSi10Mg specimens is described. The process parameters and build orientations of the CVN (Charpy V-notch) specimens were illustrated in chapter 2. The specimens were built at three GEDs of 37.1, 45.4, and 49.9J/mm<sup>3</sup> and two build orientations: 0° and 90°. The absorbed energy of the SLM-AlSi10Mg specimens in the Charpy impact test is reported in Table X. Here, a total of the sixteen (16) specimens are reported in Table X, and the data is also available at reference [28].

**Table X: Absorbed energy of SLM-AlSi10Mg specimens in the Charpy impact test.**

GED (J/mm <sup>3</sup> )	Build orientations	Specimen ID	Absorbed energy (J)
<b>37.1</b>	0°	S1	3.9
		S2	3.9
	90°	S3	2.2
		S4	2.0
		S5	2.1
<b>45.4</b>	0°	S6	5.6
		S7	5.6
	90°	S8	2.4
		S9	2.6
		S10	2.6
<b>49.9</b>	0°	S11	3.1
		S12	3.2
		S13	3.2
	90°	S14	2.3
		S15	2.2
		S16	2.2

In the Charpy impact test, the strain rate of the dynamic impact was not measured. Therefore, the fractured surface roughness was taken as a gauge for evaluating the strain

hardening behavior of the tested CVN specimens. A correlation between fracture toughness and surface roughness was reported by researchers for a variety of materials. Aluminum/epoxy interface [39], alumina platelet reinforced borosilicate glass matrix composites [40], and granite rocks [41] were investigated in this area. Ponson *et al.* [42] reported a correlation between fracture toughness and surface roughness for a ductile fracture presented in Figure 19. For brittle fracture, the correlation was reported at reference [43].

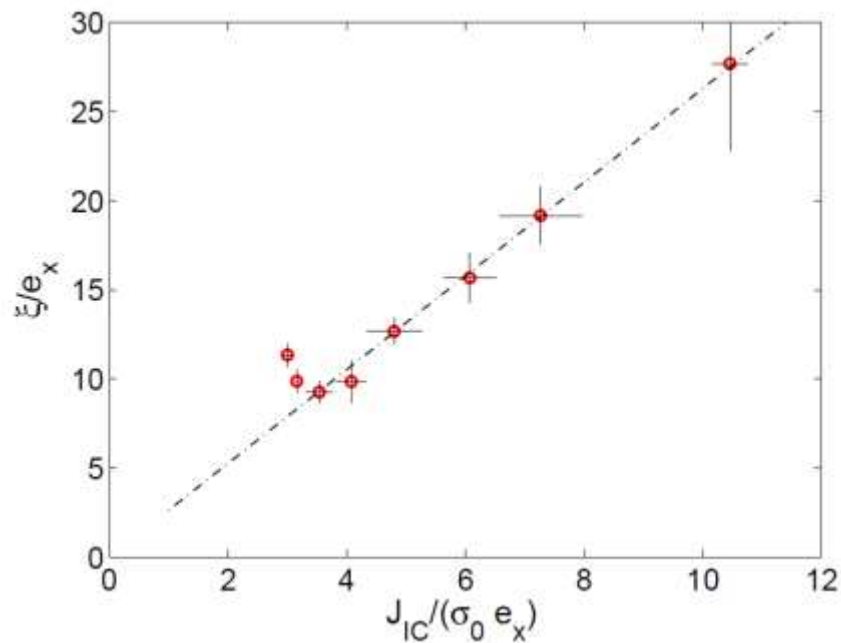


**Figure 19: A correlation between toughness and roughness. Here  $\xi$  is for the ductile fracture surface roughness, and  $J_{IC}$  is a measure of the material's resistance to crack growth [42]. Here,  $e_x$  is the in-plane (x-y plane) element dimension (i.e., normalized length), and  $J_{IC}$  is normalized by the reference flow strength,  $\sigma_0$  (= 300MPa) and  $e_x$  [42].**

The fracture toughness is also related to the strength of the materials. Ritchie [44] reported that, for aluminum alloys, the strength of the materials decreased with increasing the fracture toughness (Figure 20).

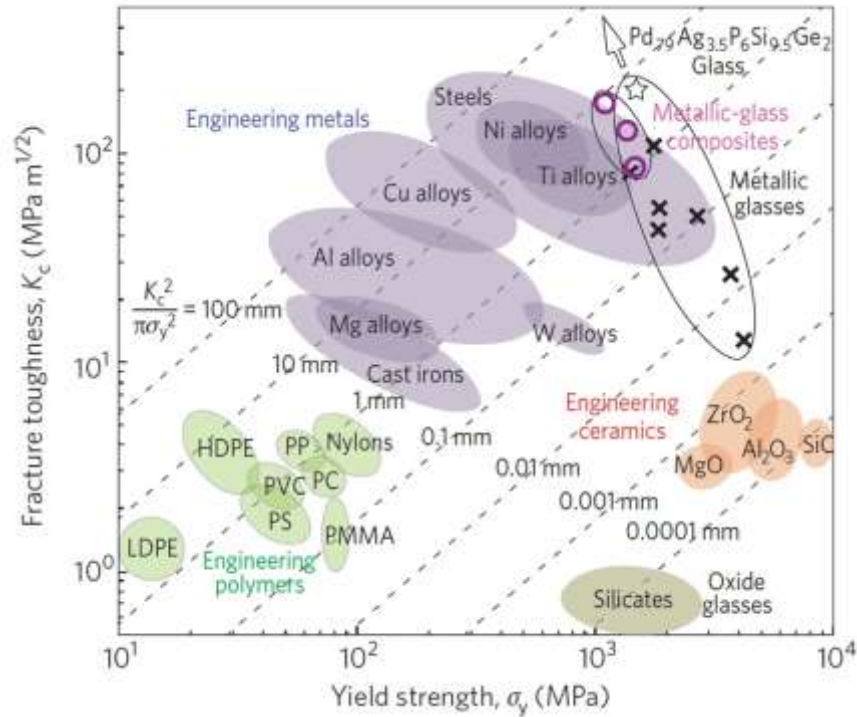


Figure 20: A strength–toughness relationship for engineering materials is presented by the Ashby plot [44].

According to Holloman’s equation [45] for stress-strain behavior in strain hardening,

**Equation 10: Holloman Equation**

$$\sigma = K\varepsilon^n$$

In the above equation (10),  $\sigma$  is the stress,  $K$  is the strength index or strength coefficient, the corresponding plastic strain is denoted by  $\varepsilon$ , and  $n$  is the strain hardening exponent,  $n < 1$  [33].

Surface roughness is related to the strength coefficient of the materials [46],

**Equation 11: Relation between surface roughness and strength co-efficient**

$$R \propto K^{-q}$$

In this equation (11), surface roughness is presented by  $R$ , and  $q$  is calculated from the strength hardening exponent,  $n$  depending on the corresponding material deformation conditions. The roughness is calculated from the CVN specimen's fractured surface to determine a relationship between the surface roughness and strength for the tested CVN (Charpy V-notch) specimen. A parametric surface roughness model is applied where the surface roughness parameter is represented by  $R_s$ .

According to the constitutive relationship that is presented by Hooke's law,

**Equation 12: Hooke's law**

$$\sigma = E\varepsilon$$

In this equation (12),  $E$  is the elastic modulus of the specimen. Substituting equation (10) and (12) into equation (11) and it was found that,

**Equation 13: Relation between roughness and strength of the material**

$$R_s \propto (E^n \sigma^{1-n})^{-q}$$

From the above equation (13), the strength of the material is inversely related to the roughness,  $R_s$  of the fractured surface of the specimen. The inverse relationship between surface

roughness and strength was observed in a variety of materials, such as Al-5052 alloy [46] and ceramics [47].

The CVN specimens' surface roughness,  $R_s$  was determined using a stochastic model proposed by Underwood and Banerji [48]. The model uses a 'profile generation' technique. The technique is a non-destructive method that uses a parametric surface roughness relationship for the randomly oriented surface profile. It was mentioned that Underwood and Banerji's model conforms best to the real situation among various stochastic models [49]. The model is presented as,

**Equation 14: Surface roughness model**

$$R_s = \left(\frac{4}{\pi}\right)(R_L - 1) + 1$$

The model describes a linear relationship between the oriented surface, and randomly samples surface, and it is applicable for  $R_s \geq 1$  [48]. In equation (11),  $R_L$  is the profile roughness parameter, which is equal to the true profile length,  $L_t$  divided by the projected length,  $L'$ , such as

**Equation 15: Profile roughness parameter**

$$R_L = \frac{L_t}{L'}$$

The coefficient  $(4/\pi)$  of the equation (14) was included from the stereometric relationships [49].

In this work, 3D fractured surface images of the CVN specimen was captured by a digital microscope (Keyence VHX-5000) at 300x magnification. At this magnification, a total of 72 images can be captured from a fractured surface of the CVN specimen. Figure 21 illustrates the schematic diagram of 72 images of a fractured surface. There are nine (9) rows and eight (8) columns. Each box represents an image section, so a total of 72 images. The size of each image was  $1,141\mu\text{m} \times 855\mu\text{m}$  (i.e.,  $x \times y$ ). The whole fractured surface was  $10,000\mu\text{m}$  (i.e.,  $2,000\mu\text{m}$  is for the V-notch and  $8,000\mu\text{m}$  is the vertical length along the y-axis)  $\times 10,000\mu\text{m}$  (i.e.,  $x \times y$ ). The remaining part of the vertical (i.e., along the y-axis) and horizontal (i.e., along the x-axis) sections were ignored in the data collection process. The line profile was developed vertically (i.e., along the y-axis) on a fractured surface by a digital microscope. Therefore, to apply equation (14) for this investigation, the true profile length was used as  $855\mu\text{m}$ . A fractured surface and a surface profile are presented in Figures 22 and 23, respectively.

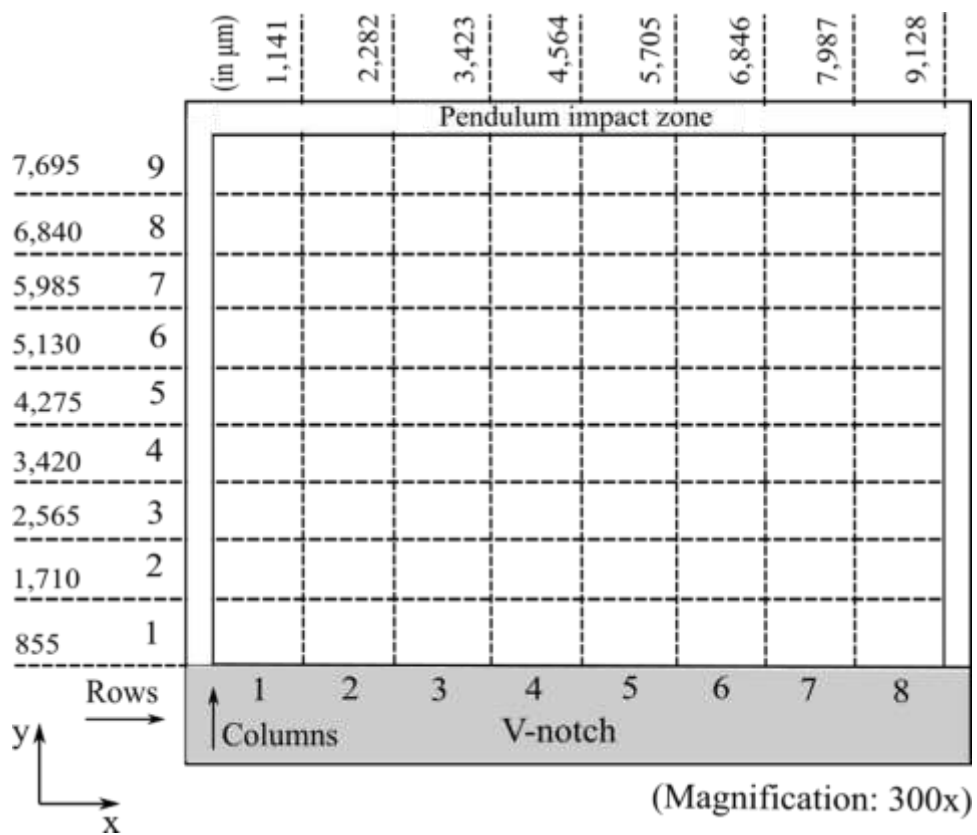
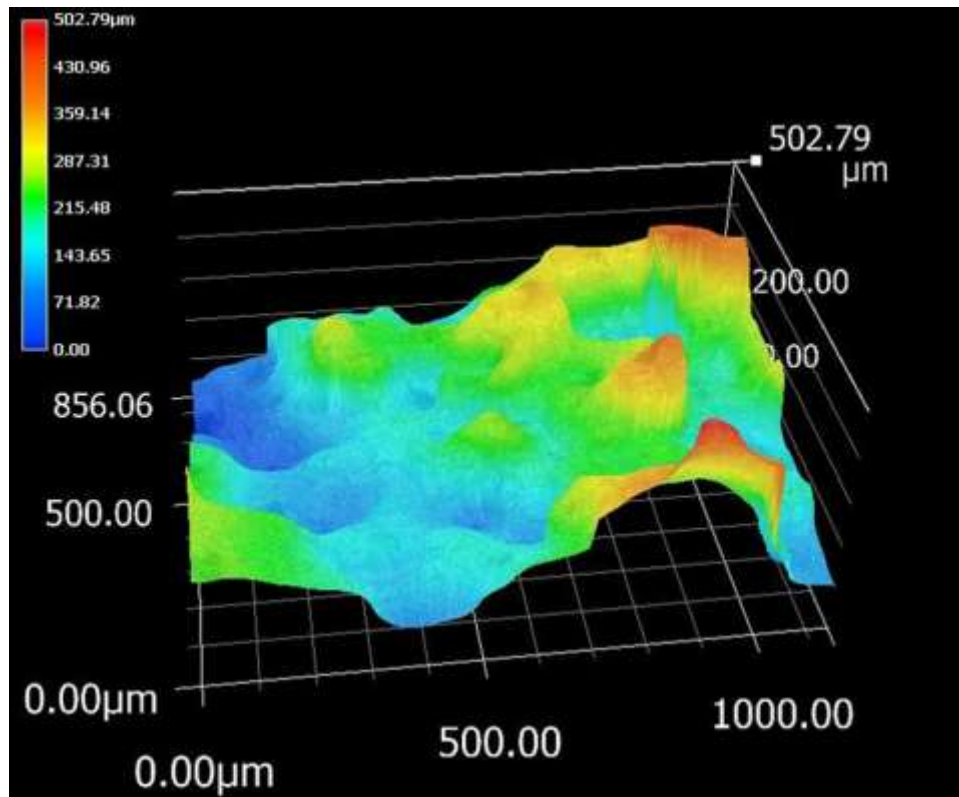
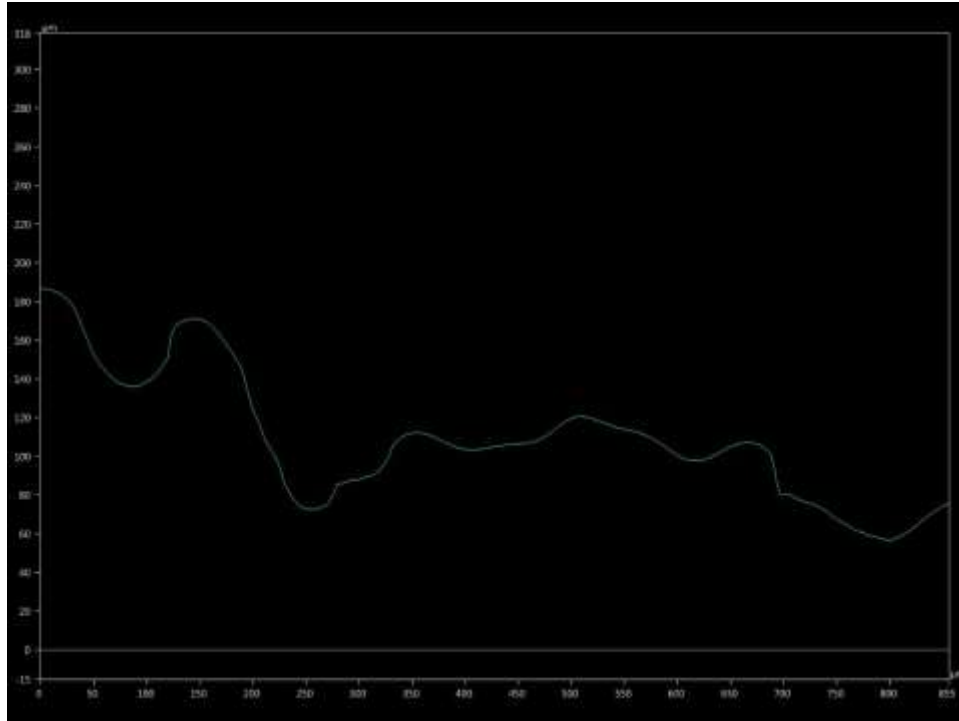


Figure 21: A schematic diagram of a fractured surface image was captured by a digital microscope at 300x magnification for a tested CVN specimen.



**Figure 22: A 3D fractured surface image of a tested CVN specimen captured by a digital microscope at 300x magnification.**



**Figure 23: A surface profile was taken from one of the 72 images of a tested CVN specimen's fractured surface. The development of the profile and profile image were captured by a digital microscope. The roughness ( $R_s$ ) of the profile above is  $R_s = 1.29$**

In the Charpy impact test, the cross-sectional area of the V-notch region of the CVN specimen experiences compression and tension for the pendulum impact. On a schematic diagram of the fractured surface (Figure 24), the region close to the pendulum impact zone experience compression and called the compression region. The same side of the V-notch experience tension for the impact and defined that as a tension region. The middle region of the fractured surface is the region between the tension and compression regions, the so-called neutral region.

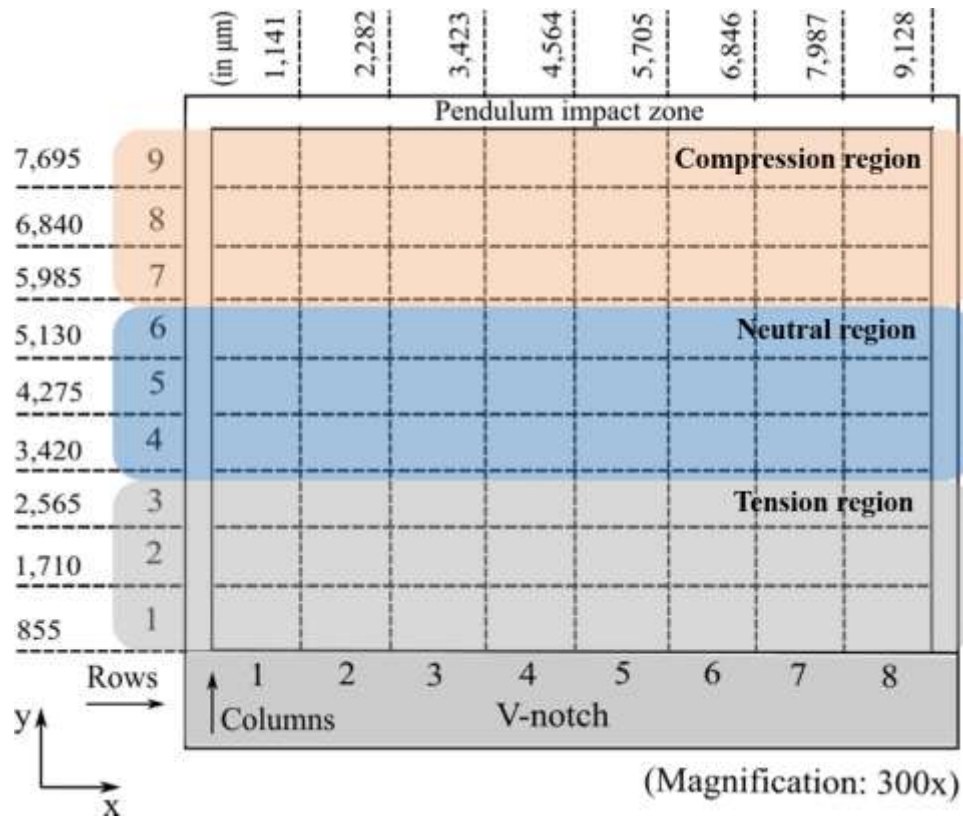


Figure 24: A schematic diagram of three regions: tension, neutral, and compression, of a fractured surface of a tested CVN specimen.

#### 4.1. Surface Roughness

Surface roughness was evaluated from the fractured surface of all the specimens. An average was calculated for each build orientation of corresponding specimens. The surface roughness graphs were plotted the vertical distance against the roughness values to observe the behavior of roughness across the vertical space (i.e., from V-notch to the pendulum impact end). The graphs are presented in Figures 25-30. In figures, each of the value along the y-axis (i.e., roughness value) represents the roughness of the area  $1,141\mu\text{m} \times 855\mu\text{m}$  ( $x \times y$ ). The error bars represent the standard deviation from the average of the roughness values. The tension, neutral, and compression regions are also marked with 'dashed' boxes in each graph.

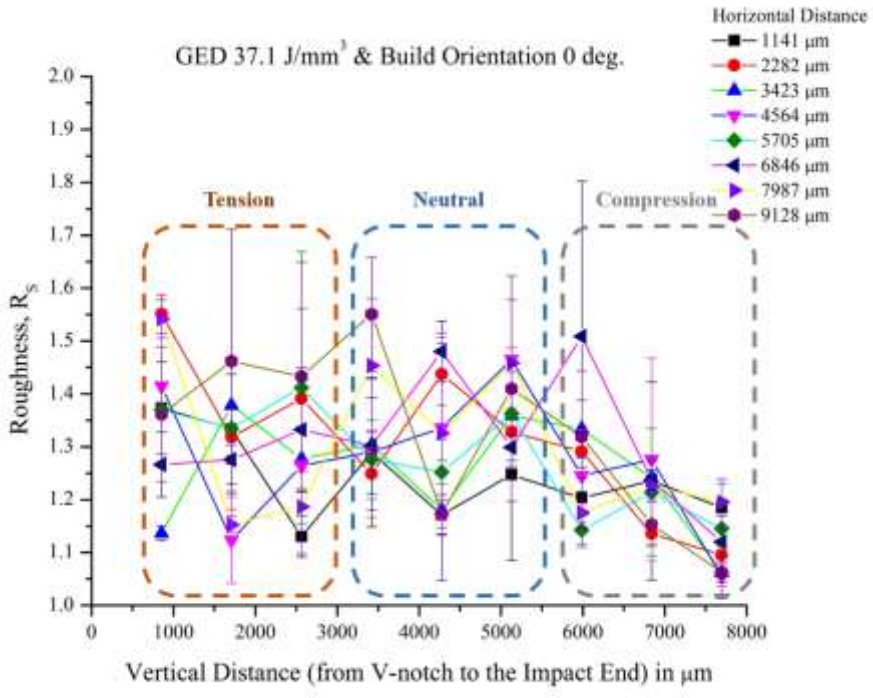


Figure 25: Average roughness of the fractured surface of the CVN specimens built at a GED of 37.1J/mm<sup>3</sup> and 0° build orientation.

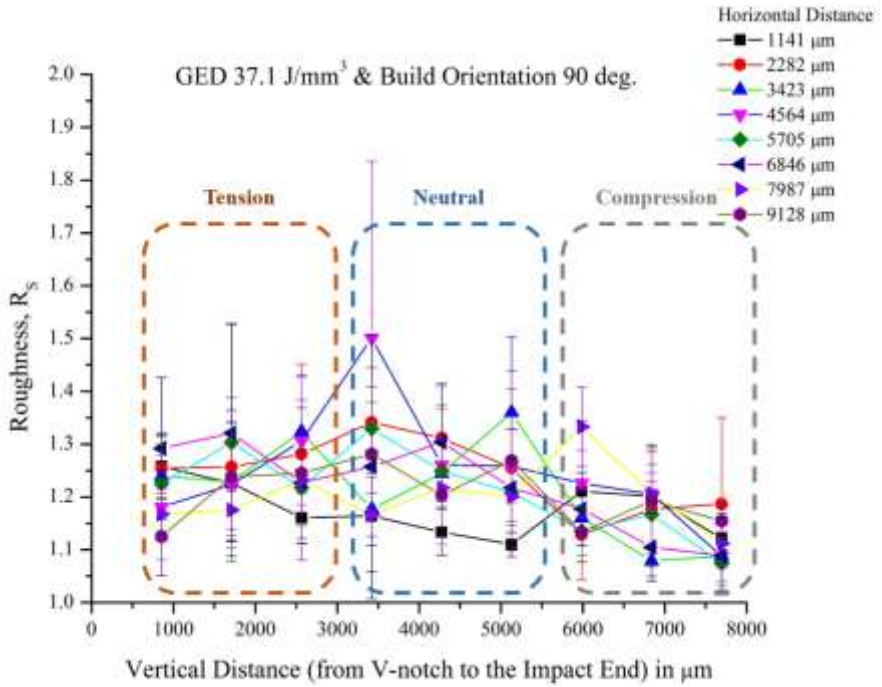
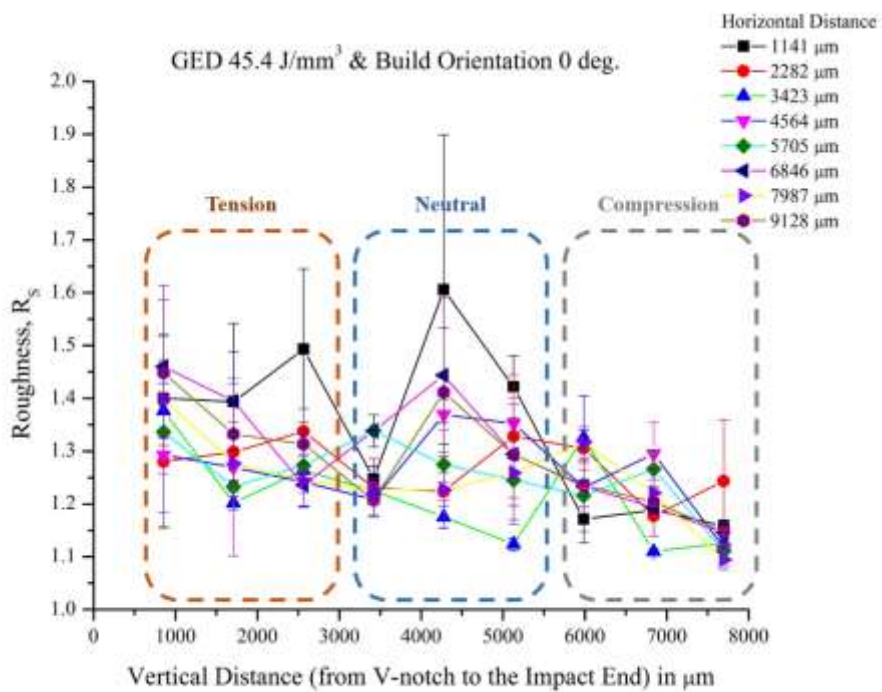


Figure 26: Average roughness of the fractured surface of the CVN specimens built at a GED of 37.1J/mm<sup>3</sup> and 90° build orientation.



**Figure 27: Average roughness of the fractured surface of the CVN specimens built at a GED of 45.4J/mm<sup>3</sup> and 0° build orientation.**

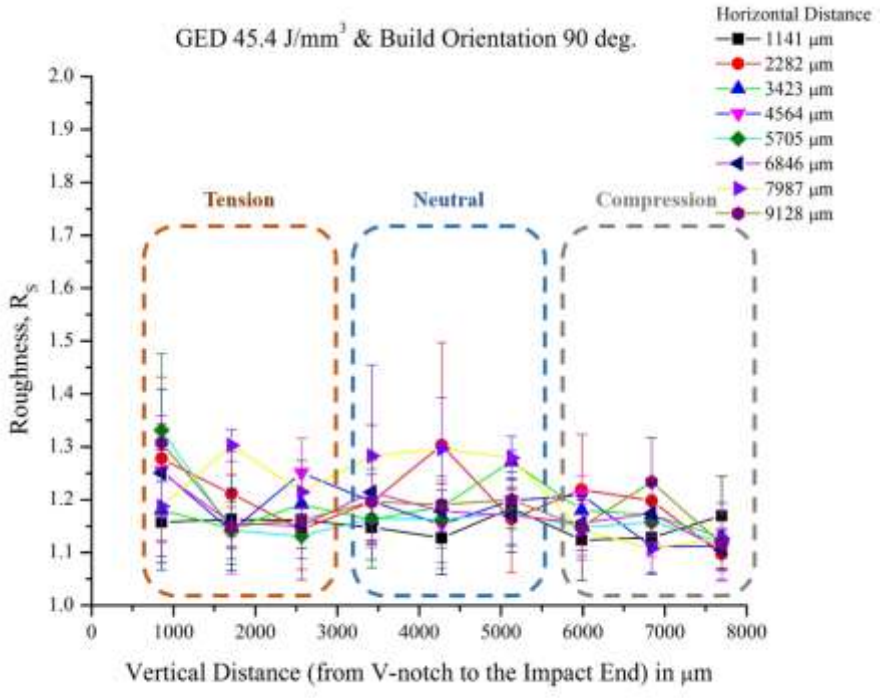


Figure 28: Average roughness of the fractured surface of the CVN specimens built at a GED of 45.4J/mm<sup>3</sup> and 90° build orientation.

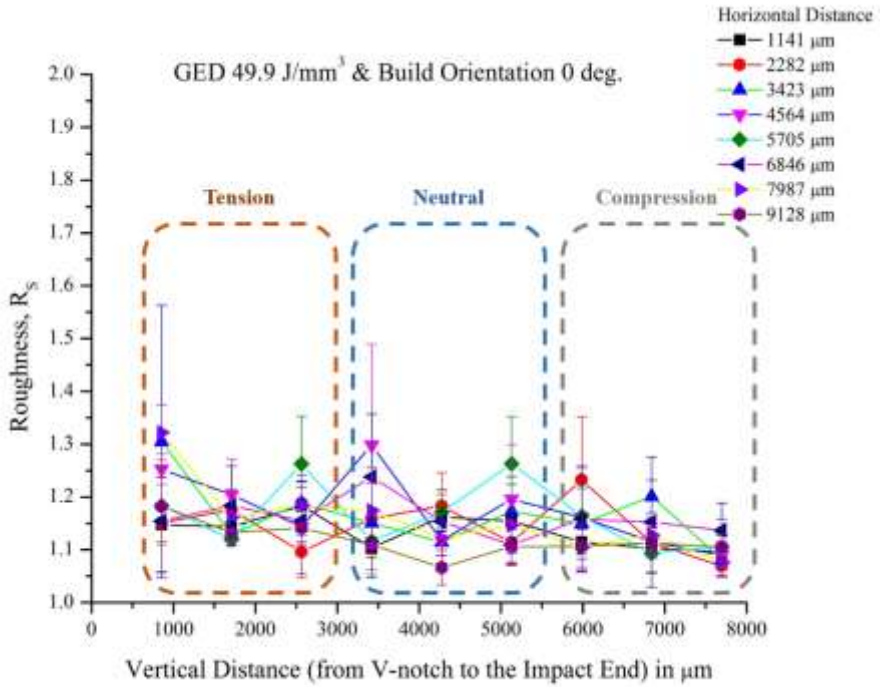
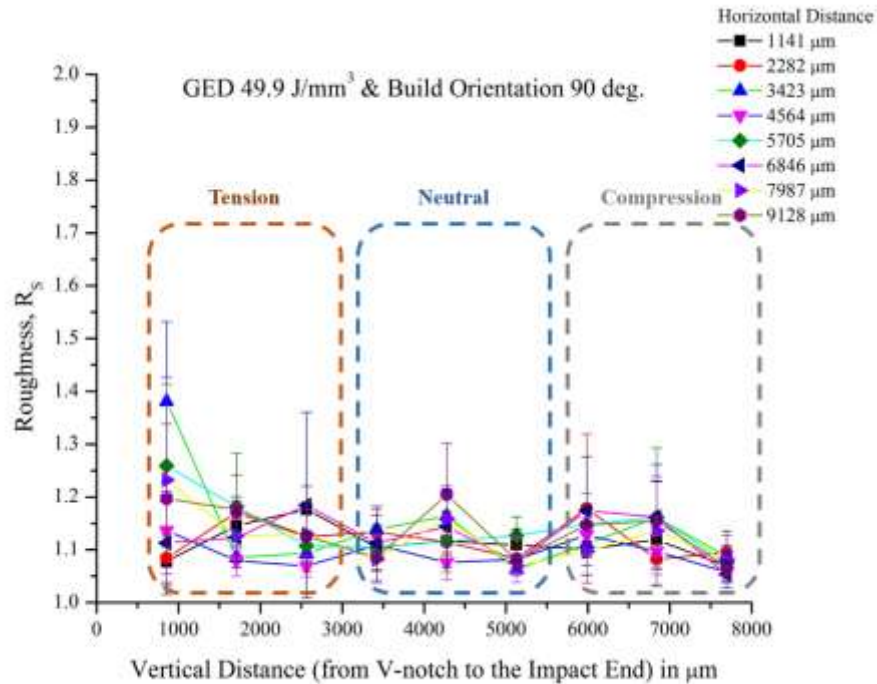


Figure 29: Average roughness of the fractured surface of the CVN specimens built at a GED of 49.9J/mm<sup>3</sup> and 0° build orientation.



**Figure 30: Average roughness of the fractured surface of the CVN specimens built at a GED of 49.9J/mm<sup>3</sup> and 90° build orientation.**

It was observed that the surface roughness values were lower at the compression regions. The roughness in the tension and neutral regions were nearly close. It was also found that the roughness values were comparatively lower for the 90° specimens for all the GEDs. A trend was also observed for all the GEDs and build orientations. The surface roughness value increased with approaching the tension regions (i.e., V-notch zone) from the compression regions (i.e., pendulum impact zone). It may be predicted that the strain hardening occurred at the pendulum impact zone in the compression region.



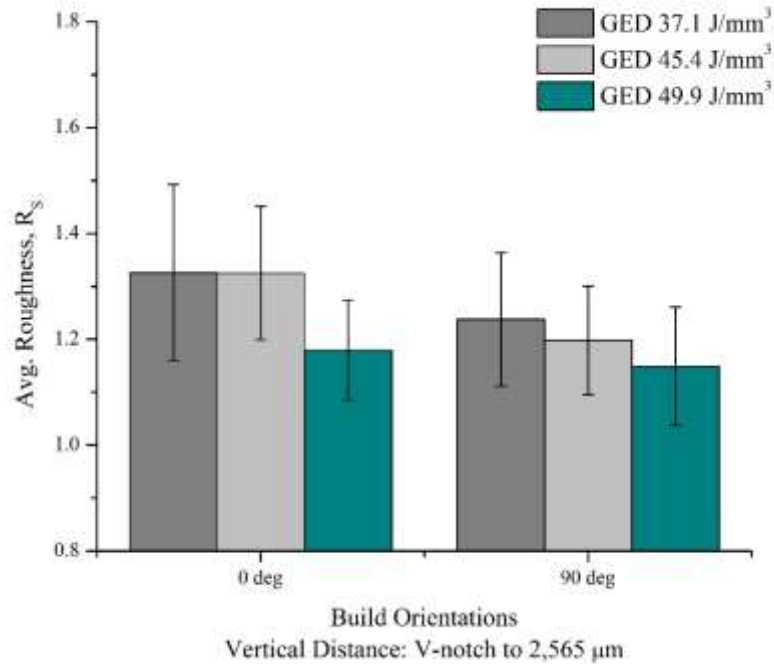


**Figure 32: Average roughness of the ‘tension’ region of the CVN specimens.**

It was found that the roughness values were higher for the 0° specimens (Figure 32). Depending on the GEDs, the roughness values varied in the tension region. Therefore, it was evaluated that the higher GEDs obtained lower roughness values. The error bars represented the standard deviation from the average, and the standard deviation values varied from 0.09 to 0.17.

#### **4.1.1.1.1. Statistical Significance: Roughness on Tension Region**

The ‘student’s T-test’ was applied to evaluate the ‘statistical difference’ of the roughness values in the tension region at build orientations and GEDs. It was observed (Table XII and the statistical sample size in Table XI) that the roughness for the specimens at build orientations 0° and 90° and prepared at GED of 49.9J/mm<sup>3</sup> are not different. At more than 95% confidence limit, the roughness of the remaining specimens produced at build orientations 0° and 90°, and GEDs of 37.1, 45.4, 49.9J/mm<sup>3</sup> are different.

**Table XI: Roughness on tension region: the statistical sample size for the ‘student’s T-test’**

GEDs & BOs	Statistical sample size	
	0°	90°
GED 37.1J/mm <sup>3</sup>	48	72
GED 45.4J/mm <sup>3</sup>	48	72
GED 49.9J/mm <sup>3</sup>	72	72

**Table XII: Student’s T-test for the roughness on the tension region**

GEDs & BOs	Probability, P	Confidence limit (%)
GED 37.1: 0° & 90°	P = 0.0030	99.72
GED 45.4: 0° & 90°	P = 1.4×10 <sup>-7</sup>	100.00
GED 49.9: 0° & 90°	P > 0.05	Not significant
Build 0°: 37.1 & 45.4	P > 0.05	Not significant
Build 0°: 37.1 & 49.9	P = 6.9×10 <sup>-7</sup>	100.00
Build 0°: 45.4 & 49.9	P = 1.9×10 <sup>-9</sup>	100.00
Build 90°: 37.1 & 45.4	P = 0.0429	95.71
Build 90°: 37.1 & 49.9	P = 1.9×10 <sup>-5</sup>	100.00
Build 90°: 45.4 & 49.9	P = 0.0072	99.28

#### 4.1.1.2. Neutral Region

An average roughness was determined for the neutral region. The roughness values were taken to calculate the average in the neutral region marked in a schematic diagram in Figure 33.

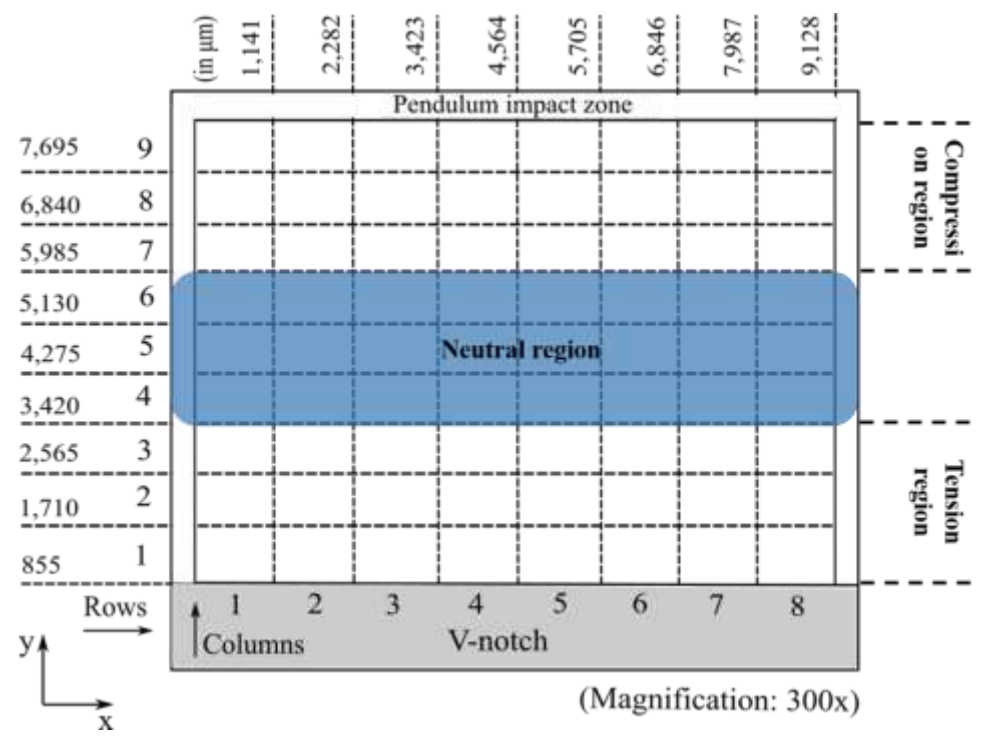


Figure 33: A schematic diagram of the 'neutral' region of a CVN specimen.

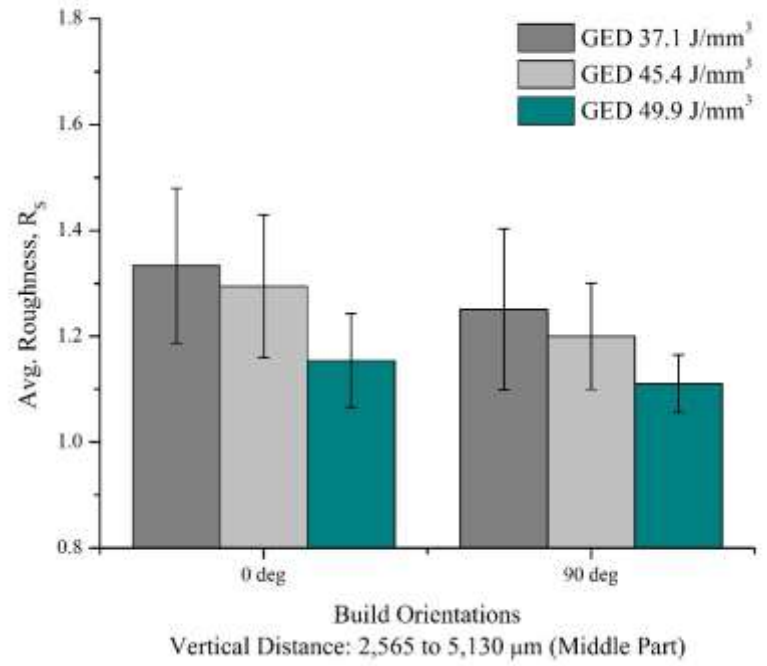


Figure 34: Average roughness of the 'neutral' region of the CVN specimens.

In the neutral region, a consistent behavior (Figure 34) was observed as the tension region. Roughness values were higher for the 0° specimens. Depending on the GEDs, the roughness varied in the neutral region. Higher GEDs experienced lower roughness values. The error bars (i.e.: standard deviation values) varied from 0.05 to 0.15.

#### 4.1.1.2.1. Statistical Significance: Roughness on Neutral Region

For the roughness in the neutral region, the ‘student’s T-test’ was applied to estimate the ‘statistical difference’ at build orientations and GEDs. It was observed (Table XIV and the statistical sample size in Table XIII) that the roughness for the specimens prepared at GED of 37.1 and 45.4J/mm<sup>3</sup> at build orientation 0° is not different. At more than 95% confidence limit, the roughness in the remaining specimens’ neutral regions produced at build orientations 0° and 90°, and GEDs of 37.1, 45.4, 49.9J/mm<sup>3</sup> are different.

**Table XIII: Roughness on neutral region: the statistical sample size for the ‘student’s T-test’**

GEDs & BOs	Statistical sample size	
	0°	90°
GED 37.1J/mm <sup>3</sup>	48	72
GED 45.4J/mm <sup>3</sup>	48	72
GED 49.9J/mm <sup>3</sup>	72	72

**Table XIV: Student's T-test for the roughness on the neutral region**

<b>GEDs &amp; BOs</b>	<b>Probability, P</b>	<b>Confidence limit (%)</b>
<b>GED 37.1: 0° &amp; 90°</b>	P = 0.0040	99.60
<b>GED 45.4: 0° &amp; 90°</b>	P = $9.0 \times 10^{-5}$	99.99
<b>GED 49.9: 0° &amp; 90°</b>	P = 0.0006	99.94
<b>Build 0°: 37.1 &amp; 45.4</b>	P > 0.05	Not significant
<b>Build 0°: 37.1 &amp; 49.9</b>	P = $1.4 \times 10^{-10}$	100.00
<b>Build 0°: 45.4 &amp; 49.9</b>	P = $1.9 \times 10^{-8}$	100.00
<b>Build 90°: 37.1 &amp; 45.4</b>	P = 0.0205	97.95
<b>Build 90°: 37.1 &amp; 49.9</b>	P = $1.2 \times 10^{-10}$	100.00
<b>Build 90°: 45.4 &amp; 49.9</b>	P = $1.6 \times 10^{-9}$	100.00

#### **4.1.1.3. Compression Region**

An average roughness was evaluated for the compression region. The roughness values were applied to calculate the average in the compression region marked in a schematic diagram in Figure 45.

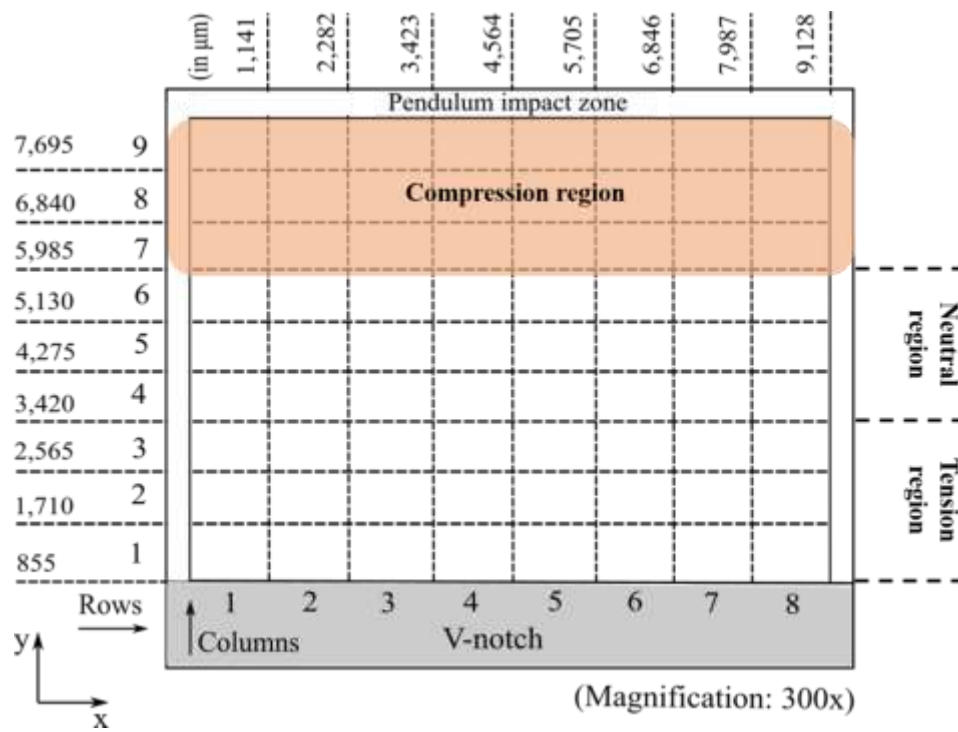
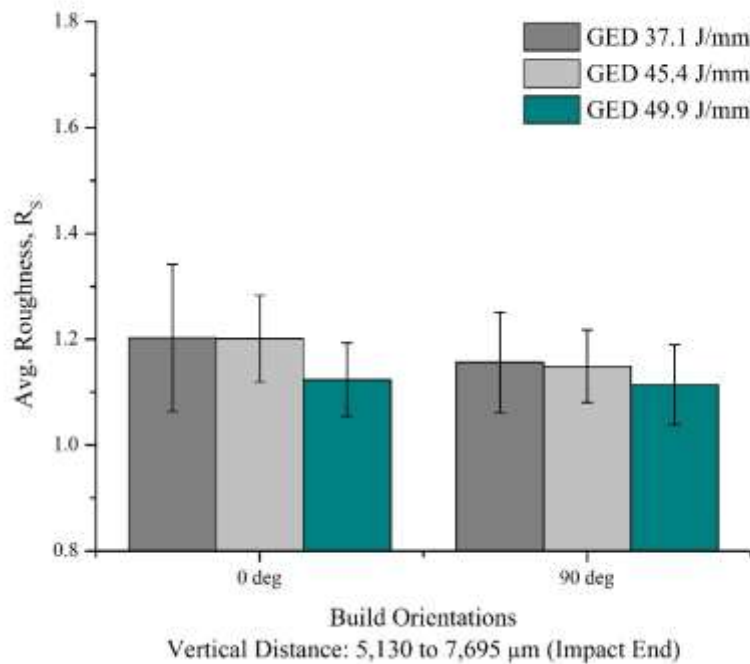


Figure 35: A schematic diagram of the 'compression' region of a CVN specimen.



**Figure 36: Average roughness of the ‘compression’ region of the CVN specimens.**

In the compression region, the similar behavior as the tension and neutral region were found that the roughness values were higher for the 0° specimens (Figure 36). Depending on the GEDs, the roughness values varied in the compression region. Higher GEDs have lower roughness values. Also, the roughness values at the compression region were comparatively lower than the tension and neutral regions. The error bars varied from 0.07 to 0.14.

Therefore, it can be predicted that the compression region experienced lower roughness values and the lower roughness indicates higher strength. Almost, for all the regions: tension, neutral, and compression, 0° specimens have higher roughness. The specimen processed at GED 49.9J/mm<sup>3</sup> has lower roughness values for the tension, neutral, and compression region.

#### **4.1.1.3.1. Statistical Significance: Roughness on Compression Region**

T-tests were performed on the roughness data obtained from the compression region for both build orientations and three GEDs. The T-test results (Table XVI and the statistical sample

size in Table XV) show that the roughness in the compression region has no difference for the specimens prepared at GED of 37.1J/mm<sup>3</sup> built at 0° and 90°, GED of 49.9J/mm<sup>3</sup> built at 0° and 90°, built at 0° and at 37.1 and 45.4J/mm<sup>3</sup>, and build at 90° and 37.1 and 45.4 J/mm<sup>3</sup>. At more than 95% confidence limit, other roughness values are significantly different at build orientations and GEDs.

**Table XV: Roughness on compression region: the statistical sample size for the ‘student’s T-test’**

GEDs & BOs	Statistical sample size	
	0°	90°
GED 37.1J/mm <sup>3</sup>	48	72
GED 45.4J/mm <sup>3</sup>	48	72
GED 49.9J/mm <sup>3</sup>	72	72

**Table XVI: Student’s T-test for the roughness on the compression region**

GEDs & BOs	Probability, P	Confidence limit (%)
GED 37.1: 0° & 90°	P > 0.05	Not significant
GED 45.4: 0° & 90°	P = 0.0005	99.95
GED 49.9: 0° & 90°	P > 0.05	Not significant
Build 0°: 37.1 & 45.4	P > 0.05	Not significant
Build 0°: 37.1 & 49.9	P = 0.0006	99.94
Build 0°: 45.4 & 49.9	P = 6.7×10 <sup>-7</sup>	100.00
Build 90°: 37.1 & 45.4	P > 0.05	Not significant
Build 90°: 37.1 & 49.9	P = 0.0040	99.60
Build 90°: 45.4 & 49.9	P = 0.0042	99.58

#### 4.1.2. The Roughness of the Total Fractured Surface Area

An average roughness was calculated for the total fractured surface area. The roughness values were used to calculate the average for the total fractured surface area marked in a schematic diagram in Figure 37.

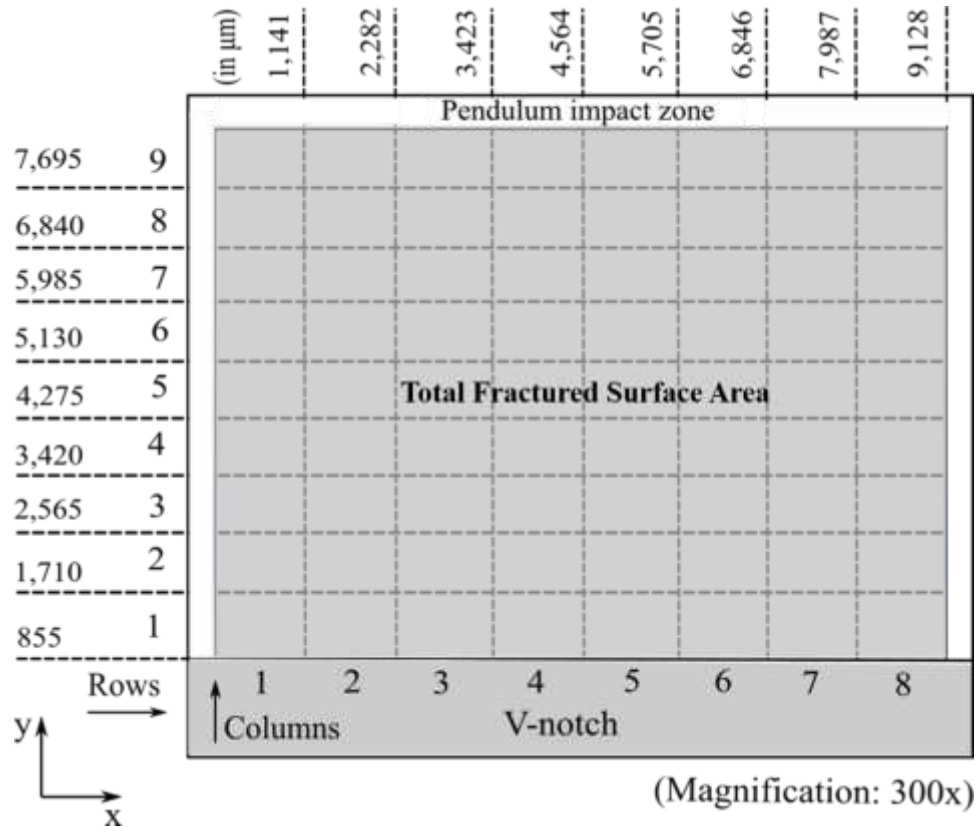
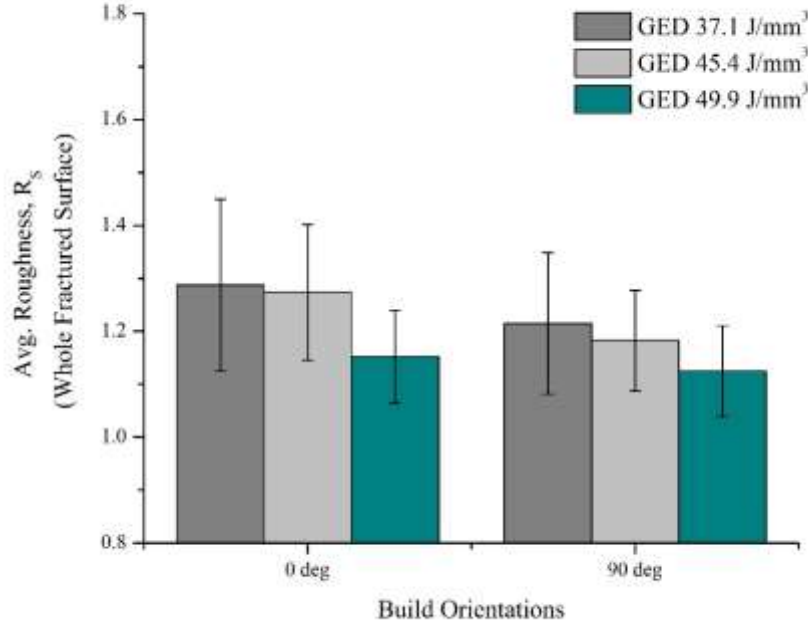


Figure 37: A schematic diagram of the total fractured surface area of a CVN specimen.



**Figure 38: Average roughness of the total fractured surface area of the CVN specimens.**

It was found that the roughness values are higher for the 0° specimens (Figure 38). Depending on the GEDs, the roughness values vary for the whole fractured surface. Higher GEDs have lower roughness values. The error bars (i.e., standard deviation values) vary from 0.09 to 0.16.

#### **4.1.2.1. Statistical Significance: Roughness for Total Fractured Surface**

The student's T-test results (Table XVIII and the statistical sample size in Table XVII) show that the roughness for the total fractured surface of the specimens prepared at GED of 37.1 and 45.4J/mm<sup>3</sup> at build orientation 0° is not significantly different. At more than 95% confidence limit, the roughness for the total fractured surface of the remaining specimens produced at build orientations 0° and 90°, and GEDs of 37.1, 45.4, 49.9J/mm<sup>3</sup> are different.

**Table XVII: Roughness for total fractured surface: the statistical sample size for the ‘student’s T-test’**

GEDs & BOs	Statistical sample size	
	0°	90°
GED 37.1J/mm <sup>3</sup>	144	216
GED 45.4J/mm <sup>3</sup>	144	216
GED 49.9J/mm <sup>3</sup>	216	216

**Table XVIII: Student’s T-test for the roughness for total fractured surface**

GEDs & BOs	Probability, P	Confidence limit (%)
GED 37.1: 0° & 90°	P = 0.0001	99.99
GED 45.4: 0° & 90°	P = 4.2×10 <sup>-12</sup>	100.00
GED 49.9: 0° & 90°	P = 0.0010	99.90
Build 0°: 37.1 & 45.4	P > 0.05	Not significant
Build 0°: 37.1 & 49.9	P = 2.7×10 <sup>-15</sup>	100.00
Build 0°: 45.4 & 49.9	P = 1.7×10 <sup>-19</sup>	100.00
Build 90°: 37.1 & 45.4	P = 0.0038	99.62
Build 90°: 37.1 & 49.9	P = 9.7×10 <sup>-11</sup>	100.00
Build 90°: 45.4 & 49.9	P = 9.7×10 <sup>-11</sup>	100.00

## 4.2. Observation

It may be reported that, at more than 95% confidence limit, the roughness behavior was influenced at build orientations: 0° and 90°, and GEDs of 37.1, 45.4, and 49.9J/mm<sup>3</sup> under Charpy (pendulum) impact conditions. Therefore, the strain hardenability of the materials was also affected by build orientations and GEDs.

## 4.3. Future Research

It may be recommended to perform tests for GEDs of 37.1, 45.4J/mm<sup>3</sup> prepared at build orientations of 0° because only two specimens were reported for this investigation.

## 5. Fracture Surface Analysis

Analysis of void formation and type of fractures are essential criteria for investigating a material's failure mode. After the Charpy impact test, the SLM processed AlSi10Mg CVN (Charpy V-notch) specimens broke at the pendulum impact and are suitable for fracture surface analysis. The strain rate range measured in the split Hopkinson pressure bar (SHPB) experiment was  $800 - 2555\text{s}^{-1}$ . Within this range (i.e., strain rate), no fracture surface was obtained from the SLM built AlSi10Mg SHPB specimens for the fracture surface analysis.

The fractured surface analysis was performed on the Charpy tested CVN specimens. The fractured surfaces were observed by using a digital microscope and scanning electron microscope (SEM). The fractured surface images were captured in a digital microscope (Keyence: VHX 5000) at 300x magnification and presented in Figures 39, 40, 41, 42, 43, and 44. It was noticed that columnar and deformed grains were found for the  $90^\circ$  build specimens. The grains were comparatively more extensive than that of the  $0^\circ$  build specimens. Smaller and deformed grains were found on the fractured surface of the  $0^\circ$  build specimens. Irregular and peanut-shaped voids (which appeared as black colored) were also observed in all the images using the digital microscope.

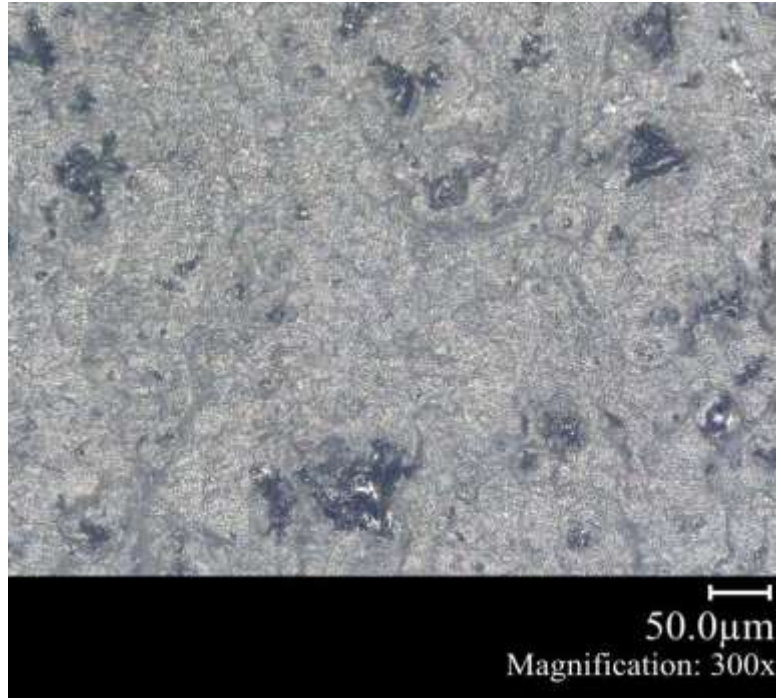


**Figure 39:** The fractured surface of the CVN specimen built at a GED  $37.1\text{J}/\text{mm}^3$ - $0^\circ$ . The image was captured by a digital microscope.

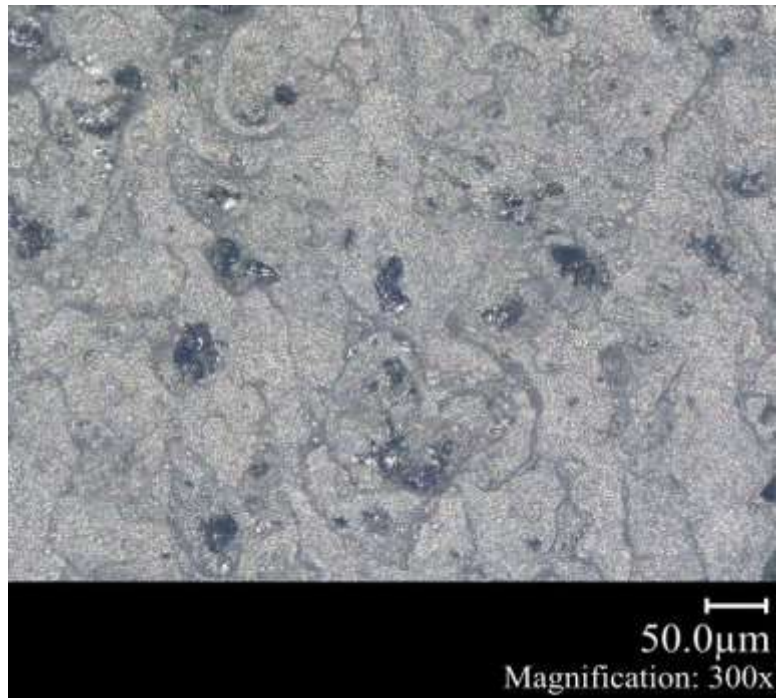


**Figure 40:** The fractured surface of the CVN specimen built at a GED  $37.1\text{J}/\text{mm}^3$ - $90^\circ$ . The image was captured by a digital microscope.

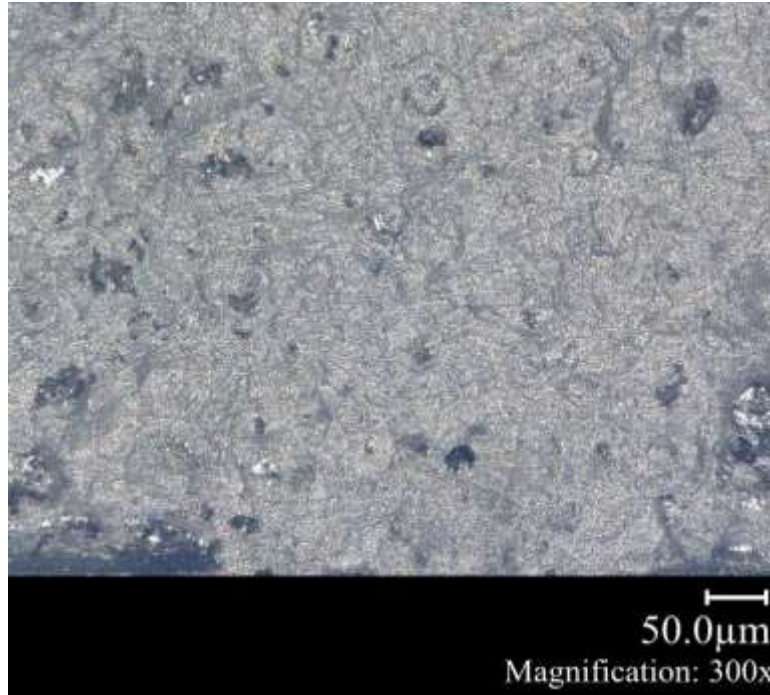


**Figure 41:** The fractured surface of the CVN specimen built at a GED 45.4J/mm<sup>3</sup>-0°. The image was captured by a digital microscope.

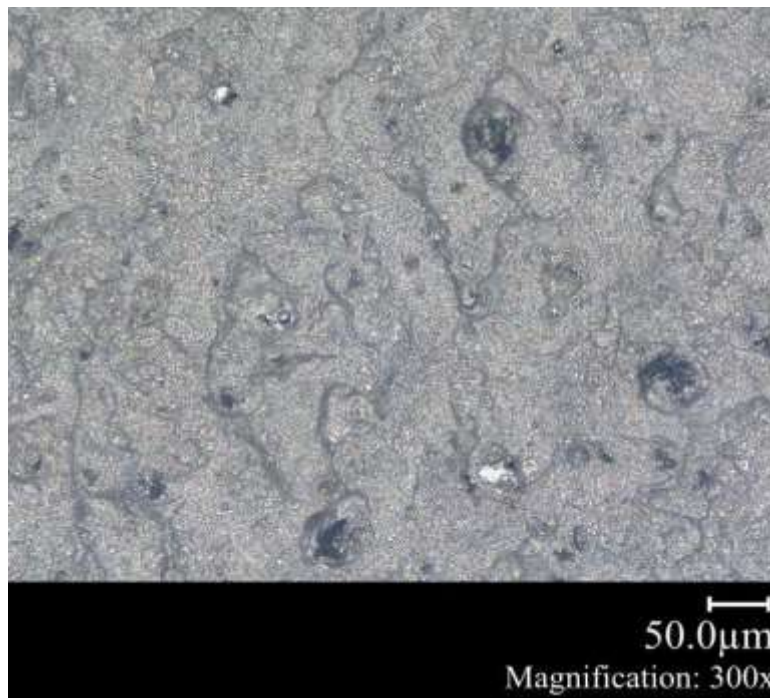


**Figure 42:** The fractured surface of the CVN specimen built at a GED 45.4J/mm<sup>3</sup>-90°. The image was captured by a digital microscope.

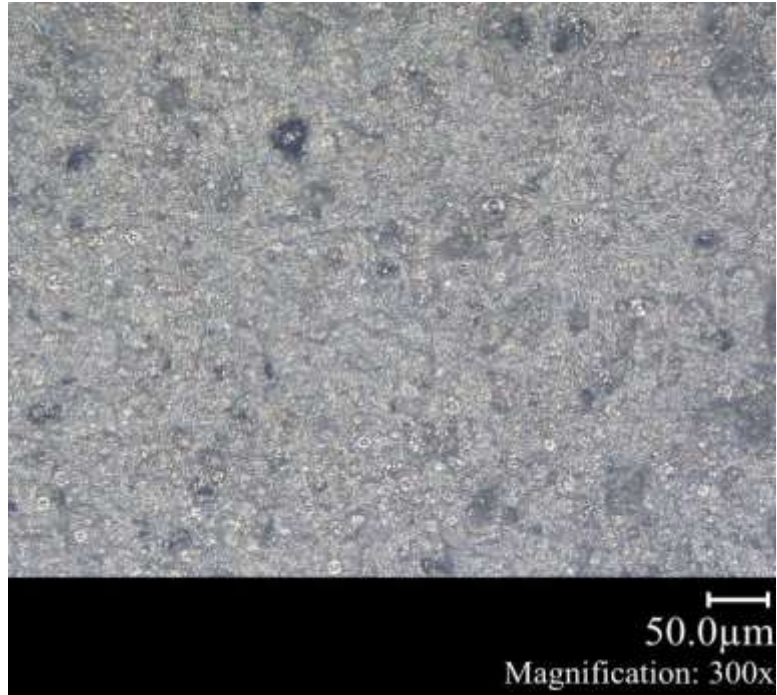


**Figure 43: The fractured surface of the CVN specimen built at a GED 49.9J/mm<sup>3</sup>-0°. The image was captured by a digital microscope.**

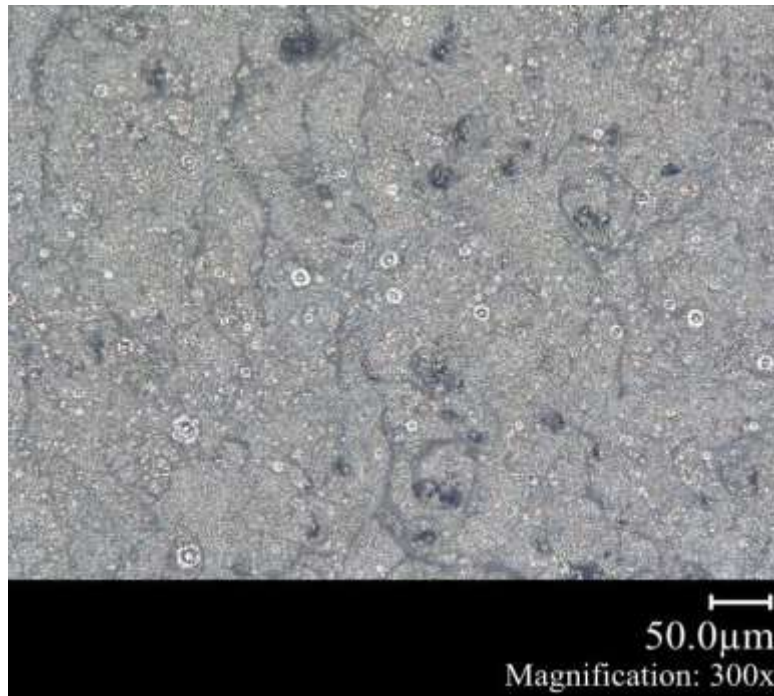


**Figure 44: The fractured surface of the CVN specimen built at a GED 49.9J/mm<sup>3</sup>-90°. The image was captured by a digital microscope.**

The high-resolution SEM (HRSEM) was used to observe fracture type on the fractured surface of the CVN specimens. Cleavage fracture was found in all the fractured surfaces of the specimens. Such luminescent facet fracture occurs in polycrystalline low-energy brittle materials. Typically, this fracture type exhibits a ‘river pattern’ when observed under SEM. Also, the phenomena on the fractured surface of the SLM built AlSi10Mg specimen was reported by the researchers [50, 51, 52, 53, 54]. The HRSEM images were presented in Figures 45, 46, 47, 48, 49, and 50. The ‘yellow’ arrows show the cleavage fracture on the fractured surface of the specimens.

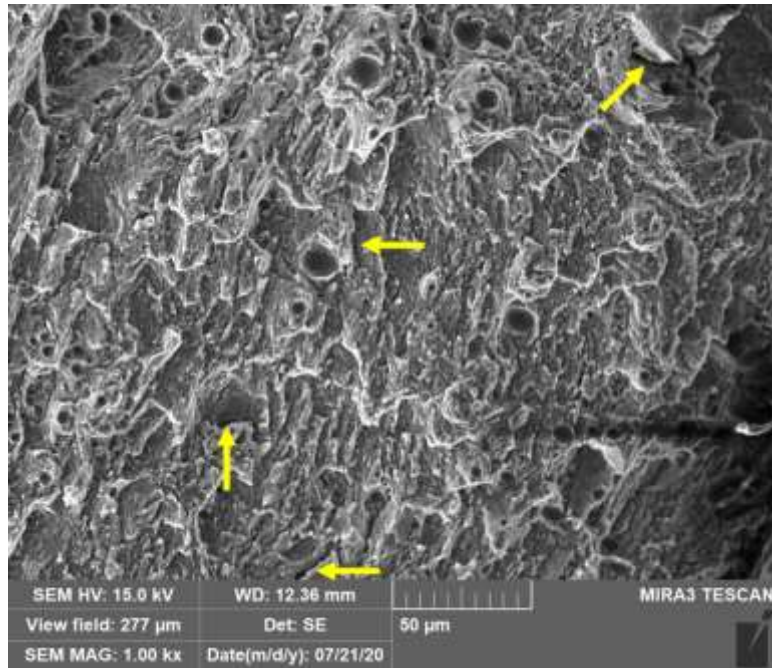


Figure 45: The fractured surface of the CVN specimen built at a GED 37.1J/mm<sup>3</sup>-0°. The image was captured under an SEM.

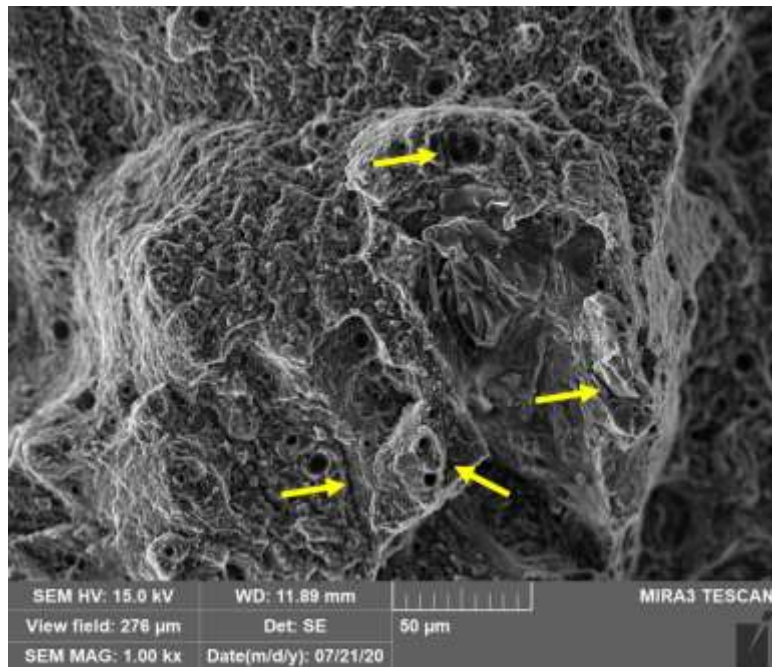


Figure 46: The fractured surface of the CVN specimen built at a GED 37.1J/mm<sup>3</sup>-90°. The image was captured under an SEM.

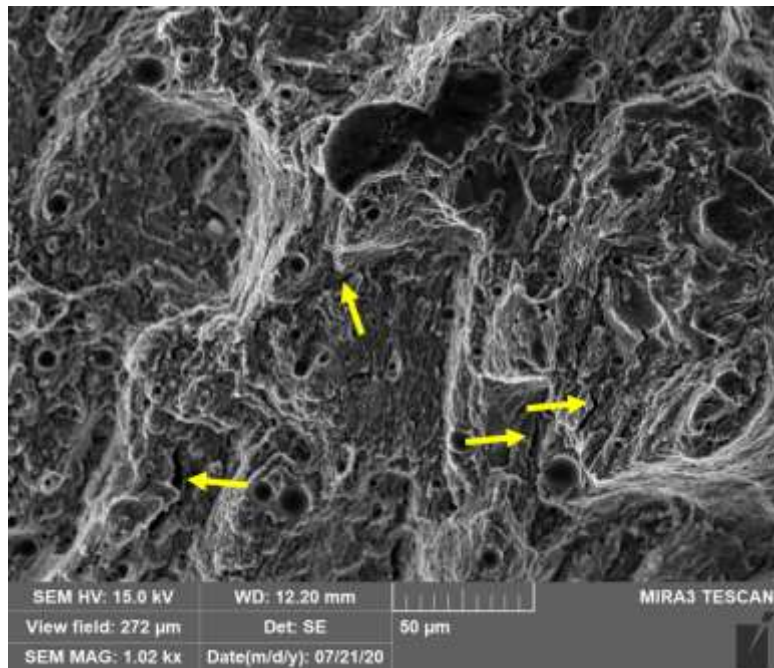


Figure 47: The fractured surface of the CVN specimen built at a GED 45.4J/mm<sup>3</sup>-0°. The image was captured under an SEM.

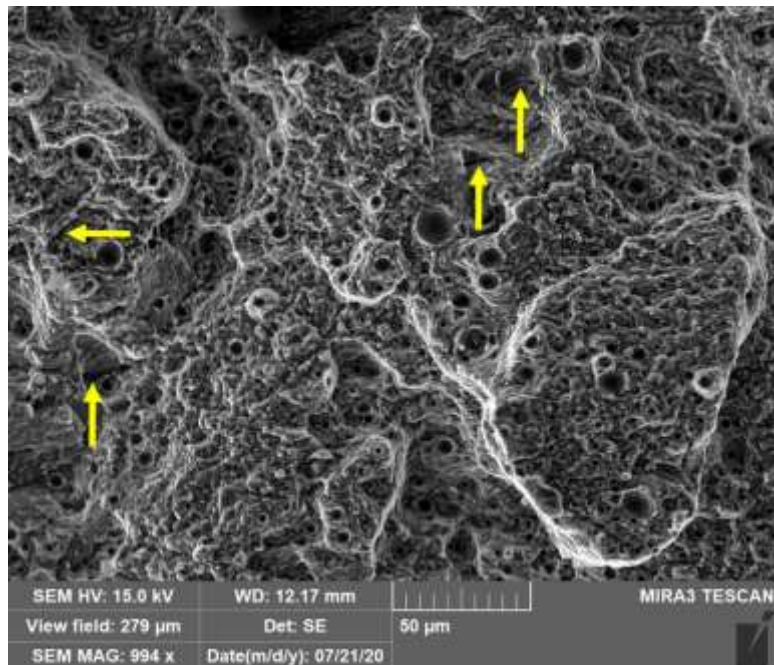


Figure 48: The fractured surface of the CVN specimen built at a GED 45.4J/mm<sup>3</sup>-90°. The image was captured under an SEM.

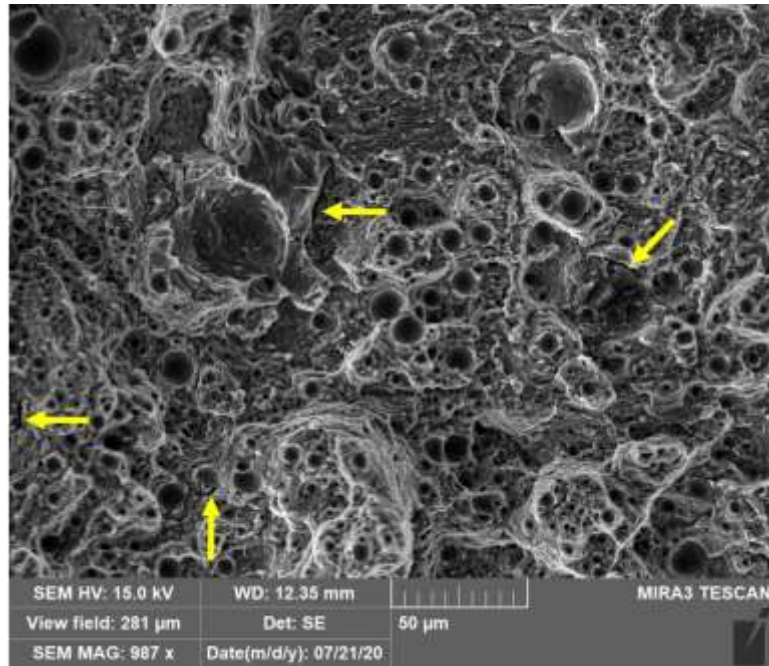


Figure 49: The fractured surface of the CVN specimen built at a GED 49.9J/mm<sup>3</sup>-0°. The image was captured under an SEM.

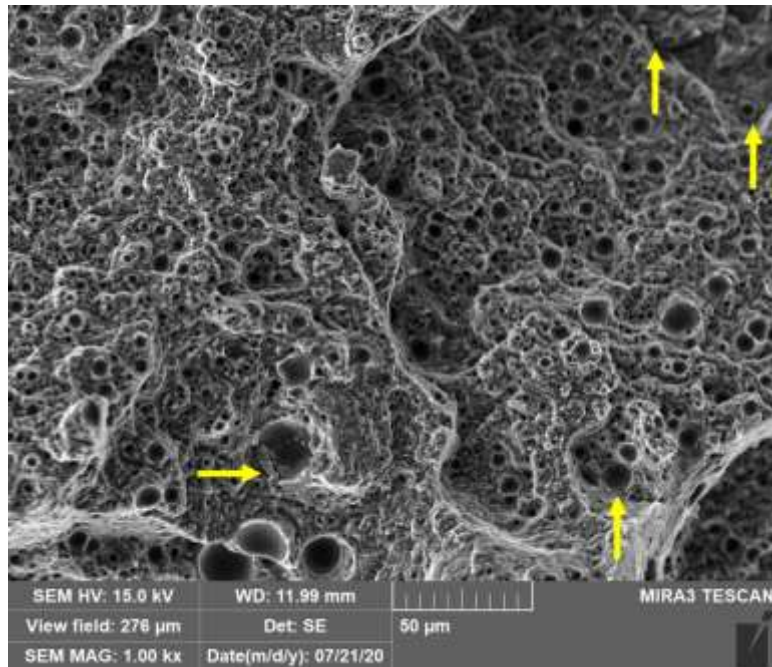
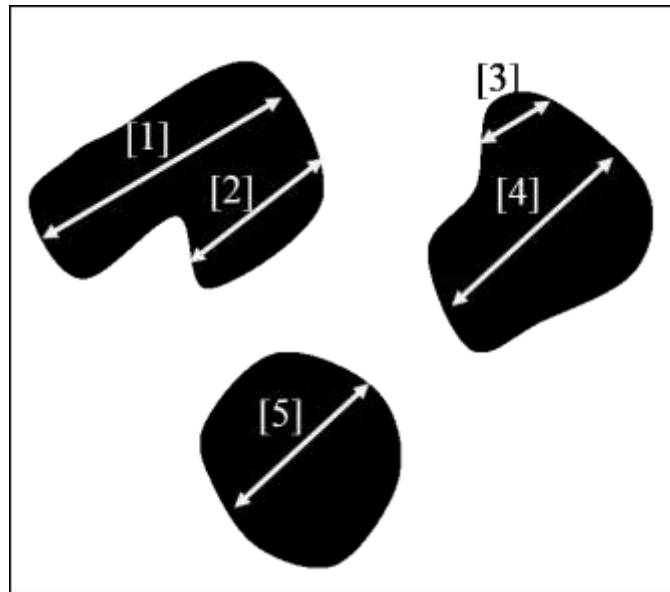


Figure 50: The fractured surface of the CVN specimen built at a GED 49.9J/mm<sup>3</sup>-90°. The image was captured under an SEM.

## 5.1. Void-Size Estimation

The void size measurement was performed using a 2-point measurement method. A 2-point measurement toolkit was available in the digital microscope, which was applied to measure the void's size on the fractured surface of the CVN specimens. The shape of the voids was observed as irregular, peanut-shaped, and coalescence of multiple voids. All these shapes were found on the fractured surface of the CVN specimens. However, it was observed that the size of voids decreased with increasing the GED (global energy density). Small voids were observed at a GED of  $37.1\text{J/mm}^3$ , whereas a GED of  $49.9\text{J/mm}^3$  developed larger voids. A schematic diagram of the 2-points measurement method is presented in Figure 51.



**Figure 51:** A schematic diagram of the 2-point measurement method for measuring the void size. [1] and [2] present the length of the coalescence of voids, [3] and [4] illustrate the peanut-shaped void (which is a type of coalescence of voids), and [5] shows for a single void.

The fractured surface of the CVN specimen exhibited three regions developed under Charpy impact test conditions: compression, neutral, and tension regions, as illustrated in Chapter 4. Figure 52 shows the schematic diagram of these regions of the fractured surface. The void was measured using the 2-points method. The measurement was performed on each row of each region of all the image sections in Figure 63. Such as row 2 from the tension region, and row 5 and row 8 are from the neutral and compression regions, respectively (Figure 53). The void size was measured using this measurement technique for the three rows of each specimen. Likewise, a total of 10,509 voids were identified from the fractured surface of all the CVN specimens.

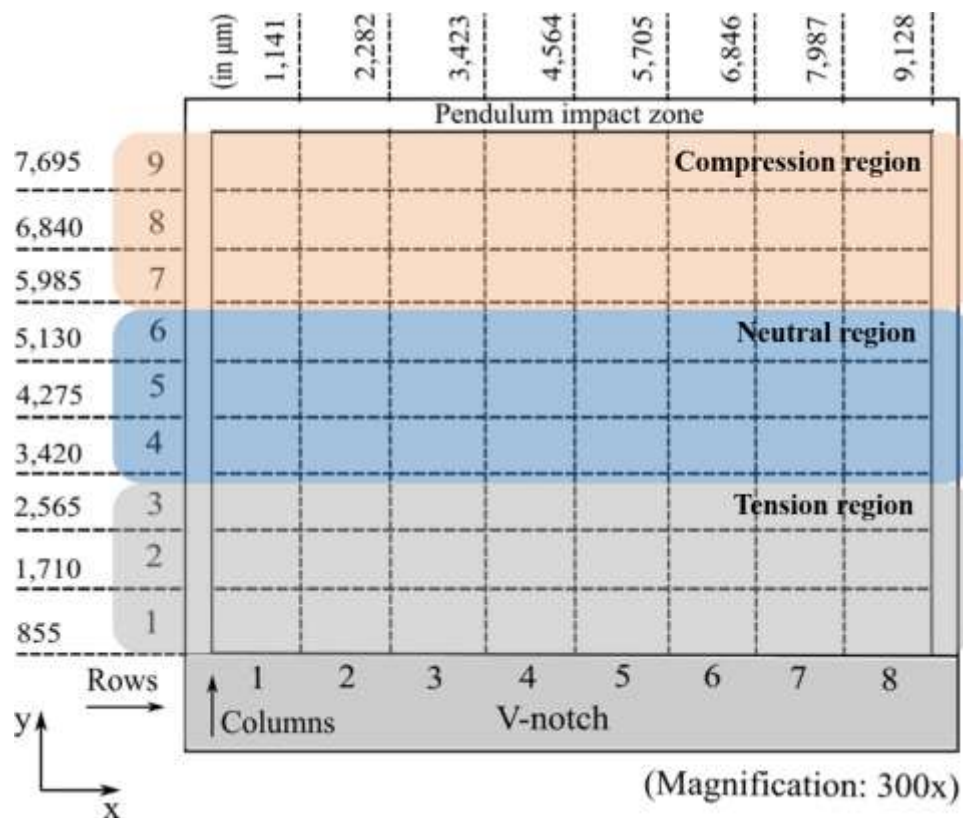
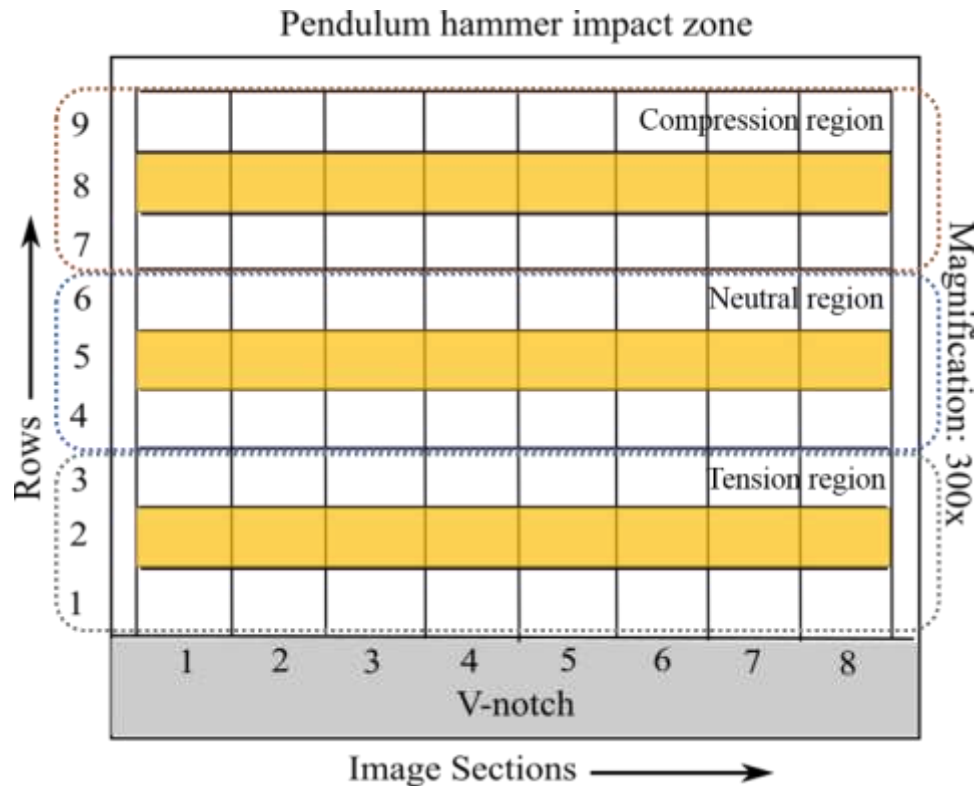


Figure 52: Schematic diagram of the three regions: tension, neutral, and compression, of the CVN specimen. It was also described in Chapter 4.



**Figure 53:** A schematic diagram of all the image sections of the CVN specimen's fractured surface. The void measurement was performed on the rows marked as 'yellow' color.

An average void size was determined for each region of each build orientation and each GED. The development of the void structure in the three regions was predicted based on these measurements.

#### **5.1.1. Void Size at Tension, Neutral, and Compression Region – Specimens Prepared at 37.1J/mm<sup>3</sup>**

It was observed (Figure 54) that the size of the void was larger for the 0° build specimens in the neutral and compression regions for the specimens processed at 37.1J/mm<sup>3</sup> GED. Still, it experienced a higher value in the tension region for the 90° build specimen. It was also observed for the 90° build specimen that the void size decreased from tension to compression regions. In

contrast, the void size increased from tension to compression region for the  $0^\circ$  specimens. The void size was larger for the GED of  $37.1\text{J}/\text{mm}^3$  than the other two GEDs of  $45.4$  and  $49.9\text{J}/\text{mm}^3$ .

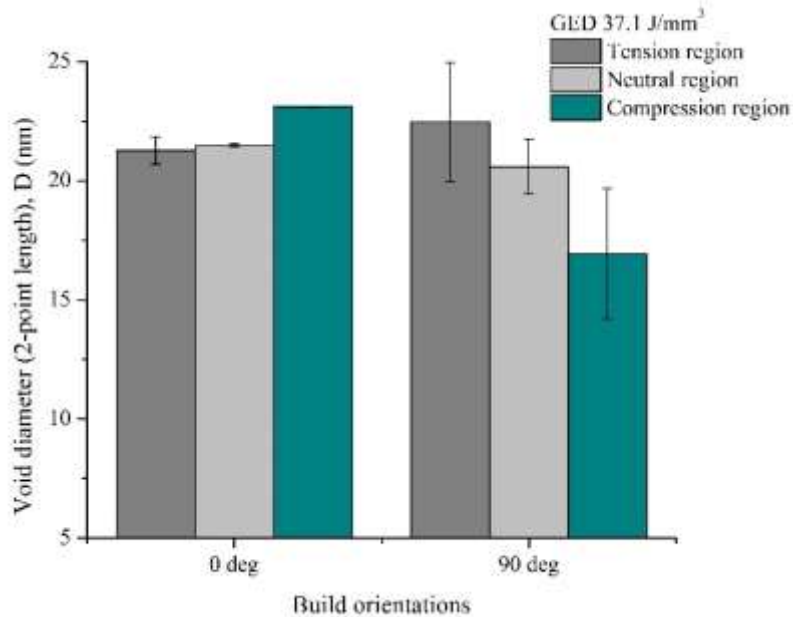


**Figure 54: An average voids size of the three regions of two build orientation:  $0^\circ$  and  $90^\circ$ . The specimens were built at a GED of  $37.1\text{J}/\text{mm}^3$ .**

### 5.1.2. Void Size at Tension, Neutral, and Compression Region – Specimens Prepared at $45.4\text{J}/\text{mm}^3$

It was observed (in Figure 55) that the smallest void size was measured for the GED of  $45.4\text{J}/\text{mm}^3$ . It was also found that the  $90^\circ$  build specimens have a comparatively larger void size than that in the  $0^\circ$  build specimens.

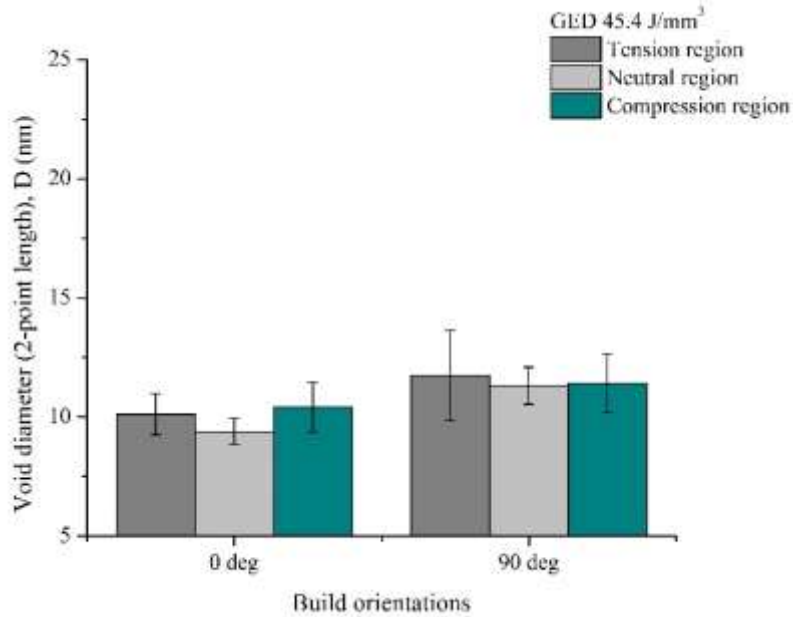


**Figure 55: An average voids size of the three regions of two build orientation: 0° and 90°. The specimens were built at a GED of 45.4 J/mm<sup>3</sup>.**

### **5.1.3. Void Size at Tension, Neutral, and Compression Region – Specimens Prepared at 49.9J/mm<sup>3</sup>**

For GED of 49.9 J/mm<sup>3</sup>, the larger void size was found at the 0° specimens than the 90° build specimens (Figure 56). Also, for both build orientations, the void size decreased from the tension to compression regions. Therefore, for both build orientations, comparatively smaller voids size was measured in the compression region.

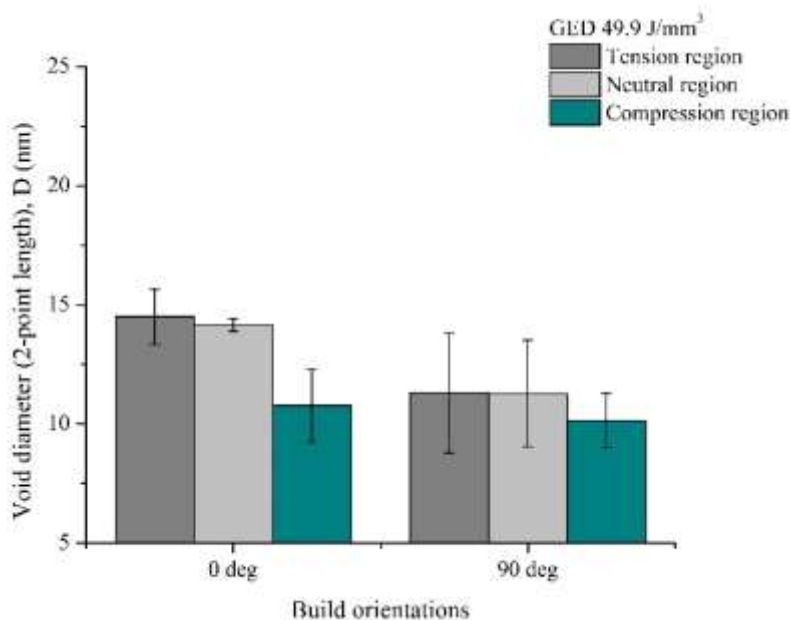


Figure 56: An average voids size of the three regions of two build orientation: 0° and 90°. The specimens were built at a GED of 49.9 J/mm<sup>3</sup>.

#### 5.1.4. Statistical Significance: Void Size at Tension region

‘Student’s T-test’ was used to evaluate the ‘statistical significance’ for the size of the void in the tension region of the specimens prepared at 0° and 90° build orientations and at three GED of 37.1, 45.4, and 49.9J/mm<sup>3</sup>. The T-test results (Table XX and the statistical sample size in Table XIX) show that the size of the void for the specimens prepared at GED 37.1J/mm<sup>3</sup> built at 0° and 90° and built at 90° prepared at GEDs 45.4 and 49.9J/mm<sup>3</sup> are not significantly different. At more than 95% confidence limit, the size of the void prepared at 0° and 90° build orientations and at a GED of 37.1J/mm<sup>3</sup> are different.

Table XIX: Void size at tension region: the statistical sample size for the ‘student’s T-test’

GEDs & BOs	Statistical sample size	
	0°	90°
GED 37.1J/mm <sup>3</sup>	599	886
GED 45.4J/mm <sup>3</sup>	729	539
GED 49.9J/mm <sup>3</sup>	361	481

**Table XX: Student's T-test for the void size at the tension region**

GEDs & BOs	Probability, P	Confidence limit (%)
<b>GED 37.1: 0° &amp; 90°</b>	P > 0.05	Not significant
<b>GED 45.4: 0° &amp; 90°</b>	P = 0.0297	97.03
<b>GED 49.9: 0° &amp; 90°</b>	P = $1.2 \times 10^{-16}$	100.00
<b>Build 0°: 37.1 &amp; 45.4</b>	P = $5.3 \times 10^{-35}$	100.00
<b>Build 0°: 37.1 &amp; 49.9</b>	P = $5.1 \times 10^{-14}$	100.00
<b>Build 0°: 45.4 &amp; 49.9</b>	P = $3.5 \times 10^{-15}$	100.00
<b>Build 90°: 37.1 &amp; 45.4</b>	P = $1.9 \times 10^{-30}$	100.00
<b>Build 90°: 37.1 &amp; 49.9</b>	P = $3.0 \times 10^{-50}$	100.00
<b>Build 90°: 45.4 &amp; 49.9</b>	P > 0.05	Not significant

### 5.1.5. Statistical Significance: Void Size at Neutral Region

In the neutral region for the size of the void, the student's T-test results (Table XXII and the statistical sample size in Table XXI) show that most of the comparisons are significantly different at more than 95% confidence limit. The comparisons between GED of  $37.1 \text{ J/mm}^3$  built at 0° and 90° and was built at 90° and at GEDs of 45.4 and  $49.9 \text{ J/mm}^3$  are not statistically different.

**Table XXI: Void size at neutral region: the statistical sample size for the 'student's T-test'**

GEDs & BOs	Statistical sample size	
	0°	90°
<b>GED 37.1J/mm<sup>3</sup></b>	585	860
<b>GED 45.4J/mm<sup>3</sup></b>	694	456
<b>GED 49.9J/mm<sup>3</sup></b>	461	457

**Table XXII: Student's T-test for the void size at the neutral region**

GEDs & BOs	Probability, P	Confidence limit (%)
GED 37.1: 0° & 90°	P > 0.05	Not significant
GED 45.4: 0° & 90°	P = 0.0197	98.03
GED 49.9: 0° & 90°	P = 6.2×10 <sup>-13</sup>	100.00
Build 0°: 37.1 & 45.4	P = 2.0×10 <sup>-38</sup>	100.00
Build 0°: 37.1 & 49.9	P = 8.4×10 <sup>-16</sup>	100.00
Build 0°: 45.4 & 49.9	P = 6.7×10 <sup>-19</sup>	100.00
Build 90°: 37.1 & 45.4	P = 1.4×10 <sup>-22</sup>	100.00
Build 90°: 37.1 & 49.9	P = 2.4×10 <sup>-36</sup>	100.00
Build 90°: 45.4 & 49.9	P > 0.05	Not significant

### 5.1.6. Statistical Significance: Void Size at Compression Region

The T-test results in the compression region (Table XXIV and the statistical sample size in Table XXIII) show that the comparison of GED of 45.4J/mm<sup>3</sup> built at 0° and 90° is not significantly different. At more than 95% confidence limit, the size of void for the other comparisons is different.

**Table XXIII: Void size at compression region: the statistical sample size for the 'student's T-test'**

GEDs & BOs	Statistical sample size	
	0°	90°
GED 37.1J/mm <sup>3</sup>	479	871
GED 45.4J/mm <sup>3</sup>	618	475
GED 49.9J/mm <sup>3</sup>	431	527

**Table XXIV: Student's T-test for the void size at the compression region**

<b>GEDs &amp; BOs</b>	<b>Probability, P</b>	<b>Confidence limit (%)</b>
<b>GED 37.1: 0° &amp; 90°</b>	$P = 1.7 \times 10^{-7}$	100.00
<b>GED 45.4: 0° &amp; 90°</b>	$P > 0.05$	Not significant
<b>GED 49.9: 0° &amp; 90°</b>	$P = 1.1 \times 10^{-29}$	100.00
<b>Build 0°: 37.1 &amp; 45.4</b>	$P = 4.8 \times 10^{-29}$	100.00
<b>Build 0°: 37.1 &amp; 49.9</b>	$P = 5.3 \times 10^{-14}$	100.00
<b>Build 0°: 45.4 &amp; 49.9</b>	$P = 9.0 \times 10^{-16}$	100.00
<b>Build 90°: 37.1 &amp; 45.4</b>	$P = 2.8 \times 10^{-10}$	100.00
<b>Build 90°: 37.1 &amp; 49.9</b>	$P = 1.4 \times 10^{-14}$	100.00
<b>Build 90°: 45.4 &amp; 49.9</b>	$P = 0.0210$	97.91

### **5.1.7. Void Size at GEDs: 37.1, 45.4, and 49.9J/mm<sup>3</sup>**

An average was calculated for all the CVN specimens for each build orientations (Figure 57). It was required to determine the effect of the GEDs on the average size of the void. It was found that the void size decreased from lower to higher GEDs for both build orientations. It was noticed that the GED of 45.4J/mm<sup>3</sup> experienced a slightly higher value for the 90° build specimens than that for the 0° specimens. The specimens processed at GED of 37.1J/mm<sup>3</sup> developed larger voids than that for the specimens processed at GED of 49.9J/mm<sup>3</sup>.

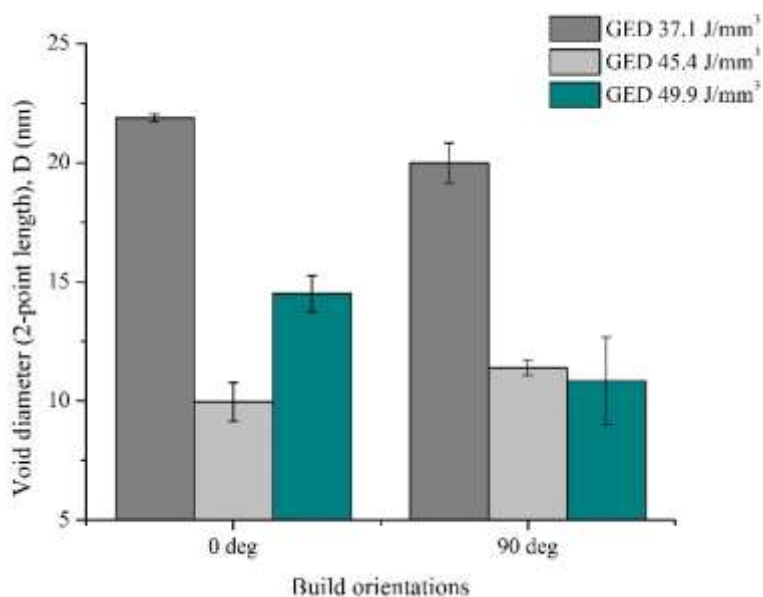


Figure 57: An average voids size at two build orientations: 0° and 90° and at three GEDs: 37.1, 45.4, and 49.9 J/mm<sup>3</sup>.

#### 5.1.7.1. Statistical Significance: Void Size at GEDs: 37.1, 45.4, and 49.9J/mm<sup>3</sup>

The T-test for the void size was performed for all the specimens at three GEDs. It was noticed that at 95% confidence limit (Table XXVI and the statistical sample size in Table XXV), the size of the void at built orientations and GEDs is different.

Table XXV: Void size at GEDs: 37.1, 45.4, and 49.9J/mm<sup>3</sup>: the statistical sample size for the ‘student’s T-test’

GEDs & BOs	Statistical sample size	
	0°	90°
GED 37.1J/mm <sup>3</sup>	1,663	2,617
GED 45.4J/mm <sup>3</sup>	2,041	1,470
GED 49.9J/mm <sup>3</sup>	1,253	1,465

**Table XXVI: Student's T-test for the void size at GEDs: 37.1, 45.4, and 49.9J/mm<sup>3</sup>**

<b>GEDs &amp; BOs</b>	<b>Probability, P</b>	<b>Confidence limit (%)</b>
<b>GED 37.1: 0° &amp; 90°</b>	P = 0.0018	99.82
<b>GED 45.4: 0° &amp; 90°</b>	P = 0.0007	99.93
<b>GED 49.9: 0° &amp; 90°</b>	P = $5.8 \times 10^{-54}$	100.00
<b>Build 0°: 37.1 &amp; 45.4</b>	P = $2.3 \times 10^{-98}$	100.00
<b>Build 0°: 37.1 &amp; 49.9</b>	P = $1.3 \times 10^{-40}$	100.00
<b>Build 0°: 45.4 &amp; 49.9</b>	P = $6.7 \times 10^{-47}$	100.00
<b>Build 90°: 37.1 &amp; 45.4</b>	P = $1.3 \times 10^{-57}$	100.00
<b>Build 90°: 37.1 &amp; 49.9</b>	P = $1.3 \times 10^{-106}$	100.00
<b>Build 90°: 45.4 &amp; 49.9</b>	P = 0.0052	99.48

## 5.2. Observation

A (3D-) digital microscope and a scanning electron microscope (SEM) were used to analyze the fractured surfaces obtained from CVN (Charpy V-notch) specimens. The observation of the analyses are reported here:

- The difference in the grain structure of 0° build specimen and 90° build specimen was observed using a digital microscope. The grains on the fractured surface of the CVN specimens were found as deformed grains for both orientations. Comparatively longer and columnar grains were found for the 90° build specimens, where the grains were smaller for the 0° build specimens.
- Voids were visible on the Charpy specimens' fractured surface for both orientations: 0° and 90°, and GEDs. The voids were irregular, peanut-shaped, and coalescence of multiple voids observed in all the images captured by a digital microscope.
- At more than 95% confidence limit, the three regions influenced the void size, such as tension, neutral, and compression, on the fractured surface of the CVN specimens.

- The void size was influenced by the build orientations:  $0^\circ$  and  $90^\circ$ , and GEDs of 37.1, 45.4, and  $49.9\text{J}/\text{mm}^3$  with more than 95% confidence limit.
- Cleavage fracture was observed by an SEM. The presence of the cleavage fracture was found on the fractured surface of all the specimens. Also, it was found that the presence of the cleavage fracture decreased for the GED of  $49.9\text{J}/\text{mm}^3$  specimens.

In general, the formation of voids and cleavage fractures deteriorate the strength of the materials. Therefore, from the observation on the fractured surface of the CVN specimens, it was found that the strength of the SLM processed AlSi10Mg specimens was influenced by voids, coalescences of voids, and cleavage fracture. The grain structures were influenced by build orientations. Also, it was found that the void size and presence of cleavage fracture were affected by GEDs.

## 6. Microanalysis: Tested Charpy and Split Hopkinson Pressure Bar Specimens

This chapter presents the microanalyses of the X-ray diffraction (XRD) data for both CVN (Charpy V-notch) and SHPB (split Hopkinson pressure bar) SLM built AlSi10Mg specimens. The analyses were performed to understand the corresponding crystal structure and lattice strain (or microstrain) during the dynamic impact loading experiments. The crystal structure is associated with the structure of the specimens' grain, and the lattice strain helps to describe the corresponding deformation and strain hardening behavior for both CVN and SHPB specimens. Many researchers used XRD to predict the crystal size of the specimens. Chen *et al.* [55] used the Full Width at Half Maximum (FWHM) values to predict the size of the crystal of the SLM built and spark plasma sintered AlSi10Mg alloy. Padovano *et al.* [56] and Rosenthal *et al.* [57] used the FWHM maximum value of the XRD to analyze the influence of temperature on the crystal size of the SLM-AlSi10Mg specimens. Similar types of analyses were performed by other researchers [58, 59, 60, 61, 62] to understand the crystal size of the specimens. However, both CVN and SHPB specimens went through deformation in the dynamic impact loading experiment. The crystal size for both CVN and SHPB specimens cannot be accurately analyzed unless considering the crystal's lattice strain during plastic deformation under dynamic loading. The Warren–Averbach (W-A) analysis or Williamson–Hall (W-H) analysis are often employed to analyze the lattice strain (or microstrain) and the corresponding crystal size [63]. Therefore, the W-H method was employed to investigate the lattice strain and crystal size for both CVN and SHPB specimens and to analyze the strain hardening behavior of the specimens depending on GEDs and build orientations.

## 6.1. Concept and Theory for the Microanalysis

The stress-free polycrystalline metal alloys (such as AlSi10Mg) show that the lattice plane spacings in the constituent crystals remain strain-free, with no peak broadening and peak shift. When deformation occurs elastically, and the strain remains relatively uniform over the long-distance called uniform macrostrain. In the uniform macrostrain condition, the lattice plane's spacings vary with the induced stress distribution for the applied pressure. A peak shift occurs in the diffraction lines, and a new  $2\theta$  value is found for the Bragg's angle. If the deformation occurs plastically, the lattice plane spacings are distorted and vary from one crystal to another. The microscopic strain is nonuniform and also called lattice microstrain. The nonuniform microstrain causes broadening of the corresponding diffraction line, but no peak shift occurs. Both peak shift and peak broadening may occur in plastically deformed metal alloys [64]. The diffraction line phenomena for the three different strain-conditions were presented by a schematic diagram in Figure 58.

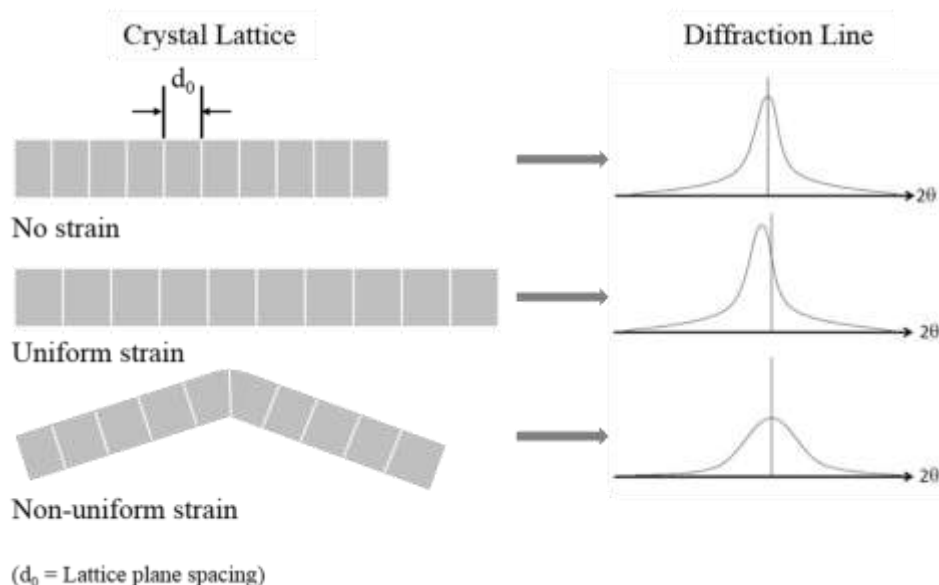


**Figure 58: A schematic diagram of lattice strain based, shift, and broadening [65].**

The line peaks of the Bragg reflection planes in the X-ray diffraction technique provide information for elemental analysis. For the purpose of this investigation, only Al peaks are considered. Since the AlSi10Mg is a hypoeutectic alloy in which the principal element is Al. This Al, in the Al/Si-solid solution, is presented as a primary aluminum or  $\alpha$ -Al matrix. The highest intensity profiles (or diffraction peak profiles) for the Bragg's reflection planes were obtained for the  $\alpha$ -Al matrix considered for the peak broadening analysis of this study. The X-ray peak broadening depicted the lattice strain (or microstrain) and crystalline size of the crystal. The non-uniformity of stress and dislocation density cause instrumental broadening related to the lattice strain (or lattice deformation) and crystal size and show the diffraction peaks in the X-ray diffraction procedure [66], and the corresponding width of the diffraction peak is presented as,

**Equation 16: Integrated width of the diffraction peak**

$$\beta_{hkl(measured)}^2 = \beta_{hkl(instrumental)}^2 + \beta_{hkl(size)}^2 + \beta_{hkl(\varepsilon)}^2$$

In the above equation (16),  $\beta_{hkl(size)}$  and  $\beta_{hkl(\varepsilon)}$  are the FWHM of the crystal size and microstrain ( $\varepsilon$ ), respectively, and  $\beta_{hkl(instrumental)}$  is the instrumental broadening. The instrumental broadening is defined by three main components. The three components that define instrumental broadening are: 1) X-ray source breadth (total area / peak height), 2) X-ray beam axial divergence, and 3) sample surface roughness [67]. The X-ray diffractometer's instrumental broadening is calculated using standard silicon (or internal silicon) for its high crystallinity.

The FWHM of X-ray diffraction from the specimen compared with the single-crystalline Si standard gave the instrumental broadening correction factor.

The true crystal broadening was determined when the instrumental broadening was removed by using a Gaussian correction [68]. The following equation was used to determine the correction factor.

**Equation 17: Instrumental broadening correction**

$$\beta_{hkl}^2(2\theta) = \beta_{hkl(measured)}^2(2\theta) - \beta_{hkl(instrumental)}^2(2\theta)$$

In the above equation (17),  $\beta_{hkl}(2\theta)$  is the true FWHM and  $\beta_{hkl(measured)}(2\theta)$  and  $\beta_{hkl(instrumental)}(2\theta)$  are, respectively, the FWHM of the specimen and single-crystalline Si-standard. The ‘ $\theta$ ’ is the Bragg’s angle for the X-ray diffraction lines.

One popular method for determining the crystal size is the Scherrer formula [68]. Scherrer’s equation (18) only addresses the specimen’s crystal size obtained from the XRD peak broadening.

**Equation 18: Scherrer’s equation**

$$\beta_{hkl}(2\theta) = \frac{0.9\lambda}{D \cos \theta}$$

In equation (18), the wavelength of the X-ray radiation (CuK $\alpha$ ) is  $\lambda = 0.154 \text{ nm}$ , and  $D$  is the average dimension of crystallite.

The lattice strain (or microstrain) was calculated from the Stokes and Wilson formula [69]. The strain-induced peak broadening arises from crystal defects and distortions [70].

**Equation 19: Stokes and Wilson formula**

$$\beta_{hkl}(2\theta) = 4\varepsilon \tan \theta$$

The crystal size and lattice strain (or microstrain) were determined using the Williamson-Hall (W-H) analysis method. Since the multiple crystallographic planes of Al can reflect distinctive Bragg's lines, several researchers [69, 70, 71] found the W-H method suitable for studying aluminum alloys.

The W-H method is a graphical analysis method that addresses the influence of the lattice strain and crystal size present in the materials [70]. The uniform deformation model (UDM), uniform stress deformation model (USDm), and uniform deformation energy density model (UDEDm) were used in the W-H analysis [63]. The first five Bragg reflections (i.e., (111), (200), (220), (311), and (222)) of Al were selected to apply the W-H method for these models.

The isotropic behavior of a material is considered in the uniform deformation model (UDM). A consistent deformation in all crystallographic directions was assumed. The mathematical expression for this model is [72]:

**Equation 20: Uniform deformation model (UDM)**

$$\beta_{hkl} \cos \theta = \left( \frac{k\lambda}{D} \right) + (4\varepsilon \sin \theta)$$

In equation (20),  $k$  is a shape factor. In the W-H method, the graph is plotted as  $\beta_{hkl} \cos \theta$  against  $4 \sin \theta$ . The crystal size,  $D$  is measured from the intercept (i.e.,  $(k\lambda/D)$ ) of the linear plot and strain,  $\varepsilon$  is determined from the linear slope of the curve fit. From this graphical

analysis, the lattice strain and crystal size for the CVN and SHPB specimens are reported in Tables XVI and XVII. However, the assumption of isotropic nature of lattice strain is doubtful for crystalline material and it is more physical considering anisotropic lattice strain,  $\varepsilon_{hkl}$  of a material [73].

Hook's law presents the anisotropic microstrain as,

**Equation 21: Hooke's law**

$$\varepsilon_{hkl} = \sigma / E_{hkl}$$

In equation (21),  $\sigma$  is uniform stress and  $E_{hkl}$  is the anisotropic Young's modulus in ( $hkl$ ) direction is given as in Equation (22).

**Equation 22: Young's modulus of the cubic crystals [74]**

$$\frac{1}{E_{hkl}} = S_{11} - 2(S_{11} - S_{12} - S_{44}) \left[ \frac{(hk)^2 + (hl)^2 + (kl)^2}{h^2 + k^2 + l^2} \right]$$

where  $S_{11}$ ,  $S_{12}$ , and  $S_{44}$  are the elastic compliances of the cubic structures. The values for  $S_{11}$ ,  $S_{12}$ , and  $S_{44}$  are obtained from reference [75]:  $1.57 \times 10^{-11}$ ,  $-5.70 \times 10^{-12}$ , and  $3.51 \times 10^{-11} \text{ m}^2 \text{ N}^{-1}$ , respectively. Therefore, equation (20) transforms into equation (23):

**Equation 23: Uniform stress deformation model (USDM)**

$$\beta_{hkl} \cos \theta = \left( \frac{k\lambda}{D} \right) + \frac{4\sigma \sin \theta}{E_{hkl}}$$

The uniform stress,  $\sigma$  was determined by measuring the slope of the graph of  $4 \sin \theta / E_{hkl}$  and  $\beta_{hkl} \cos \theta$ . The crystal size,  $D$  is obtained by measuring the intercept. The crystal size and lattice strain for the CVN and SHPB specimens were estimated using USDM in the W-H method are reported in Tables XVI and XVII.

However, it is more rational to use a parameter for the deformation in which the density of deformation energy,  $u$  causes the lattice strain [63, 73] as per the assumption in the uniform deformation energy density model (UDEDM). This model assumes that the density of the deformation energy is uniform. The energy density,  $u$  is a function of strain obtained from Hooke's law, as shown in Equation (24) as:

**Equation 24: Deformation energy density**

$$u = \frac{1}{2} E_{hkl} \varepsilon_{hkl}^2$$

Applying equation (24) into equation (23):

**Equation 25: Uniform deformation energy density model (UDEDM)**

$$\beta_{hkl} \cos \theta = \left( \frac{k\lambda}{D} \right) + \left( 4 \sqrt{\frac{2}{E_{hkl}}} \sin \theta \right) \sqrt{u}$$

According to the W-H method, the graph is plotted between  $4\sqrt{2/E_{hkl}} \sin \theta$  (or  $2^{5/2} E_{hkl}^{-1/2} \sin \theta$ ) and  $\beta_{hkl} \cos \theta$ . The crystal size is obtained by measuring the graph's intercept, and the energy density,  $u$  is calculated by measuring the linear graph's slope. The lattice strain and crystal size of the CVN and SHPB specimens obtained are reported in Tables XVI and XVII. It was suggested that W-H-UDEDM is a practical method for various materials. The results of the W-H-UDEDM showed good agreement with the transmission electron microscopy study of Al alloys and different materials [63, 70, 76].

## 6.2. X-ray Diffraction Experiment

A Rigaku-Ultima-IV X-ray diffractometer with CuK $\alpha$  radiation ( $\lambda = 0.154$  nm) system was used to perform the XRD experiment at 40 kV and 40 mA. The radiation scanning was conducted from 20° to 90° with a 0.02° step size. The X-ray diffraction patterns were obtained from the XRD experiment analyzed using the MDI-Jade software platform. The Bragg's reflection planes of Al were identified and shown in Figures 74, 80, 81, and 82. In the XRD pattern for both CVN and SHPB specimens, no new Al peaks were observed.

### 6.2.1. CVN Specimens

In the Charpy impact test, the CVN specimen experiences maximum stress at the V-notch zones. The two transverse surfaces of the two sides of the CVN specimen face experienced minimum stress during the pendulum impact on the specimen. Simulation studies on the 'Charpy impact' on different materials may help to visualize the stress distribution in the transverse

section of the CVN specimen [77, 78]. In this investigation, the XRD experiment was performed on the transverse surface (i.e., flat surface) of the CVN specimen. A tested CVN specimen and one of the transverse surfaces (i.e., flat surfaces) of the specimen are presented in Figure 59.

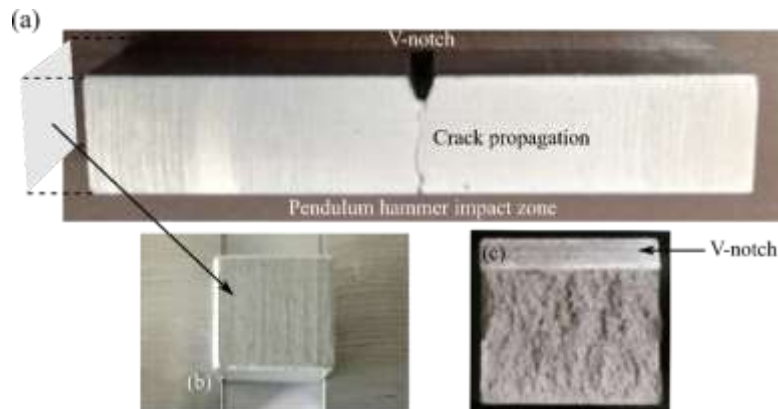


**Figure 59: A tested SLM built AlSi10Mg CVN specimen: (a) tested specimen, where the V-notch is shown on the top of the diagram and hammer impact zone is opposite to the face of V-notch. The crack initiates at the V-notch due to the impact, (b) the flat surface where XRD was performed, and (c) the fractured surface of the specimen.**

### 6.2.2. SHPB Specimens

The XRD experiment was conducted on the flat surface of the tested-SHPB specimen (Figure 60a). In the SHPB experiment, the stress wave for the incident bar impact propagates through the specimen presented in Figure 60b.

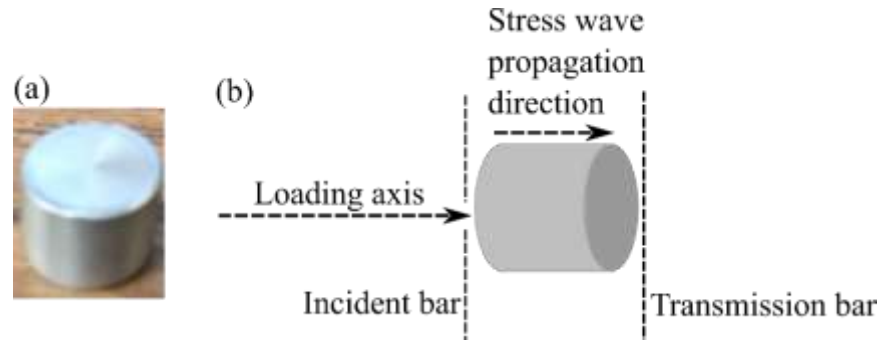


**Figure 60: XRD experiment was performed on the flat surface of the tested SHPB specimens: (a) tested SHPB specimen, and (b) a schematic diagram of the stress wave propagation direction.**

### 6.3. Microanalysis for the CVN Specimens

The XRD was performed on all the sixteen (16) CVN specimens (i.e., energy absorption data were described in chapter 4). The corresponding XRD pattern is presented in Figure 61. No significant peak shift was observed in the XRD pattern for all the specimens. An average was taken over each Bragg's reflection plane, and each build orientation and GED to get the peak shift in the XRD line graph shown in Figure 61. The result is presented by a bar chart in Figure 62. It was found that the corresponding standard deviation (SD) from the average was tiny, which is hardly visible if the SD is presented in the bar chart of Figure 62. The SD is presented in a separate bar chart in Figure 63. Since the peak shifts are minimal, so it is ignored for further calculation. Also, it was observed from Figure 61, the peak intensity of the XRD line graph depends on the build orientation. The intensity for the Al(111) was higher for the 0° build specimen, where the 90° build specimens have a higher intensity for the Al(200) peaks.

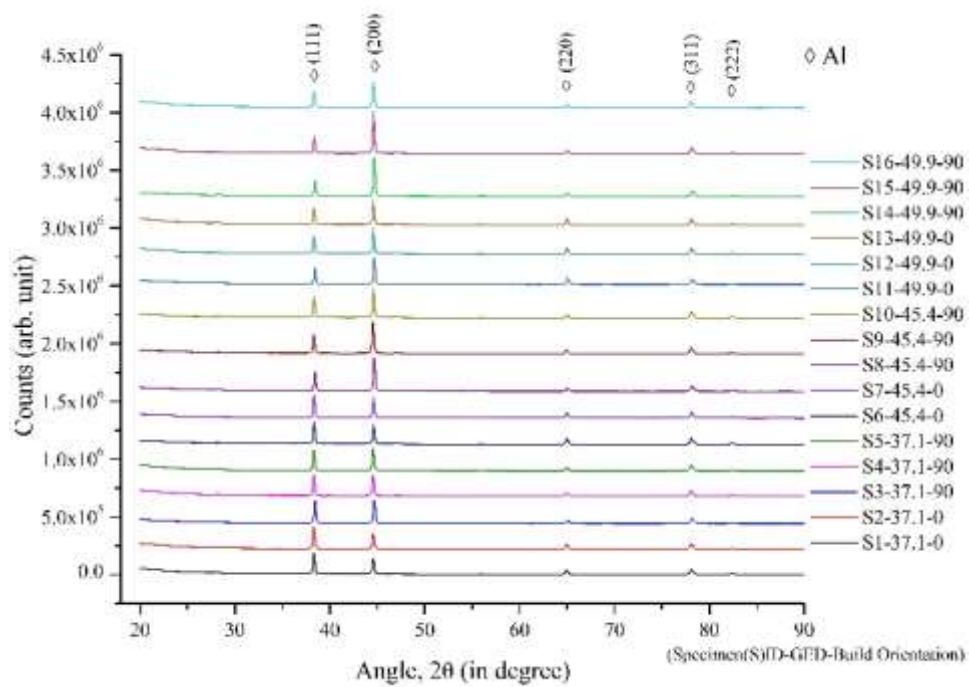


**Figure 61: The XRD line graph for the tested CVN specimens.**

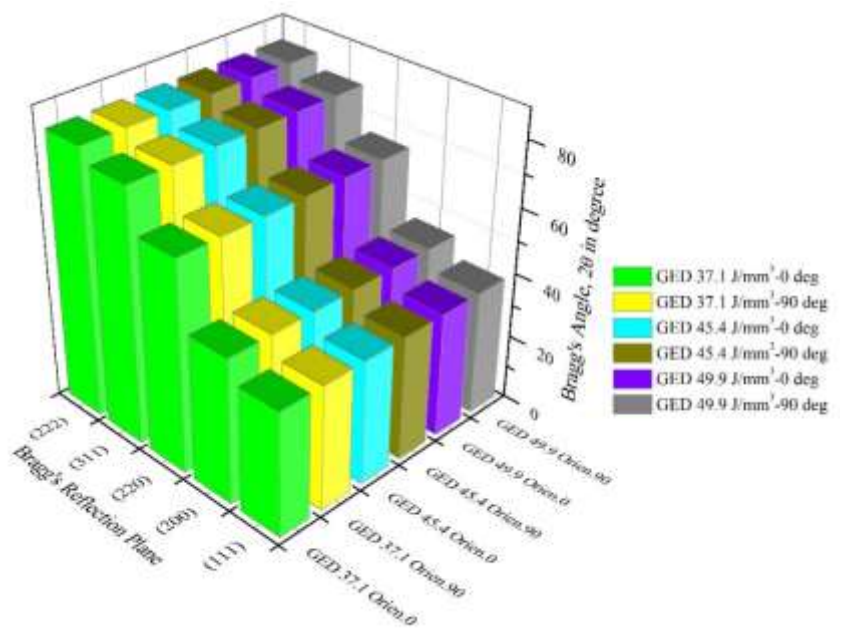


Figure 62: The average of the Bragg's angle for each peak of aluminum in the XRD line graphs for the tested CVN specimens.

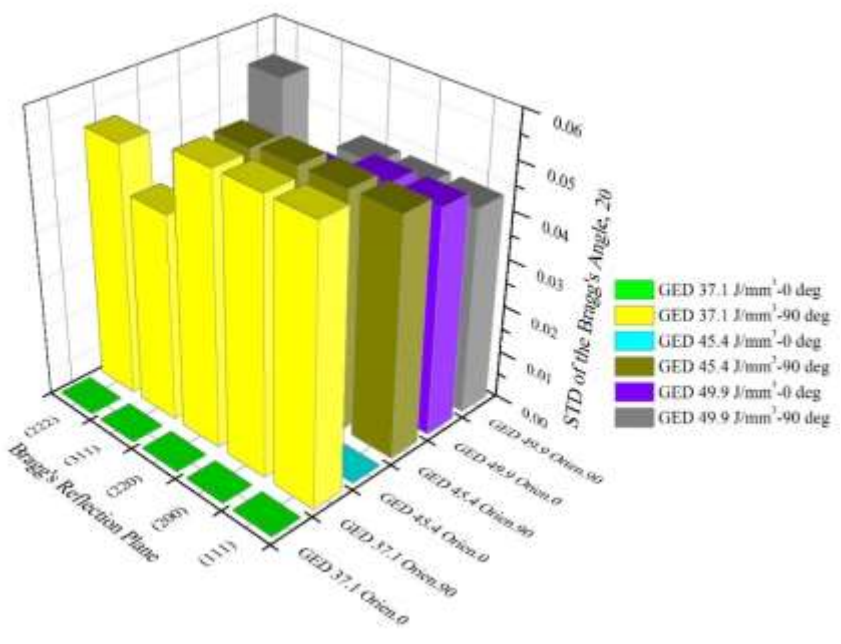


Figure 63: Standard deviation from the average of the Bragg's angle for each aluminum peak of Figure 71

The UDM, USDM, UDEDM, and Scherrer method was considered to analyze the lattice strain and crystal size of the tested CVN specimens following equations 15, 17, 20, and 22. Table XXVII presents the corresponding data of the lattice strain and crystal size. Table XXVII shows the crystal size obtained from the Scherrer method was lower than the other three methods: UDM, USDM, and UDEDM. Since UDEDM is considered to be a practical method, so, for the later analysis, the data obtained by using UDEDM will be applied.

**Table XXVII: Geometric parameters of the SLM-ALSi10Mg CVN specimens. The specimens were prepared at two build orientations (BO): 0° and 90°, and three GEDs: 37.1, 45.4, and 49.9J/mm<sup>3</sup> and tested under Chapry impact loading.**

GED, J/mm <sup>3</sup>	BO	Scherrer method	W-H method							
			UDM			USDM			UDEDM	
		D, nm	D, nm	$\epsilon$ , ( $\times 10^{-3}$ )	D, nm	$\sigma$ , MPa	$\epsilon$ , ( $\times 10^{-3}$ )	D, nm	u, kJ/m <sup>3</sup>	$\epsilon$ , ( $\times 10^{-3}$ )
37.1	0°	30.81 ±0.15	96.37 ±4.13	1.589 ±0.04	58.78 ±1.92	52.10 ±2.40	1.092 ±0.05	73.91 ±2.96	4.36 ±0.33	1.351 ±0.05
	90°	30.36 ±0.07	112.32 ±4.58	1.736 ±0.03	61.21 ±0.36	56.39 ±0.43	1.182 ±0.01	80.26 ±1.24	5.15 ±0.12	1.469 ±0.02
45.4	0°	32.54 ±0.09	108 ±4.36	1.547 ±0.03	63.15 ±2.87	50.10 ±1.75	1.050 ±0.04	79.30 ±2.27	4.08 ±0.23	1.307 ±0.04
	90°	31.77 ±0.65	108.92 ±7.45	1.605 ±0.02	63.03 ±2.56	52.76 ±1.02	1.106 ±0.02	81 ±4.24	4.46 ±0.14	1.367 ±0.02
49.9	0°	33.67 ±0.46	118.92 ±4.88	1.535 ±0.04	68.12 ±1.07	50.81 ±1.66	1.065 ±0.03	88.04 ±2.26	4.11 ±0.24	1.312 ±0.04
	90°	32.07 ±1.35	135.99 ±12.32	1.723 ±0.13	71.42 ±3.48	58.34 ±5.20	1.223 ±0.11	96.15 ±6.50	5.34 ±0.88	1.491 ±0.12

### 6.3.1. Lattice Strain

The bar chart of Figure 64 represents the lattice strain obtained from the UDEDM analysis section of Table XXVII. A trend about lattice strain was observed and reported here. The influence of build orientation and GED was observed on the lattice strain. The higher GED experienced higher lattice strain. The 90° specimens faced higher lattice strain than the 0° specimens. The higher lattice strain influenced the size of the crystal. The 0° specimens built at GED of 37.1J/mm<sup>3</sup> experienced the smallest crystal size presented in Figure 66. However, the

crystals of the GED  $37.1\text{J/mm}^3$ - $0^\circ$  specimens experienced higher lattice strain than the crystals of the  $49.9\text{J/mm}^3$ - $0^\circ$  specimens (Figure 79).

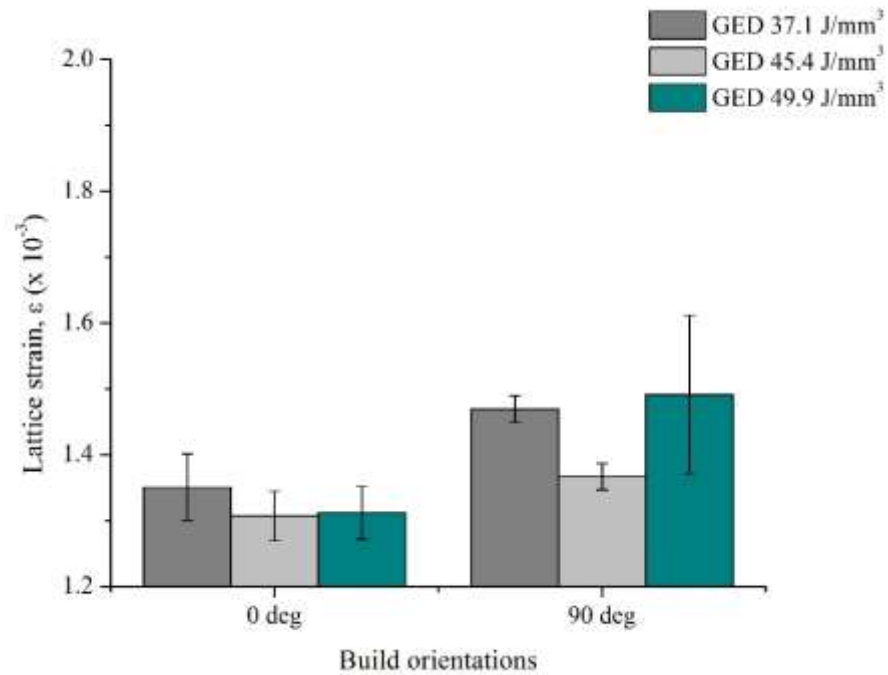
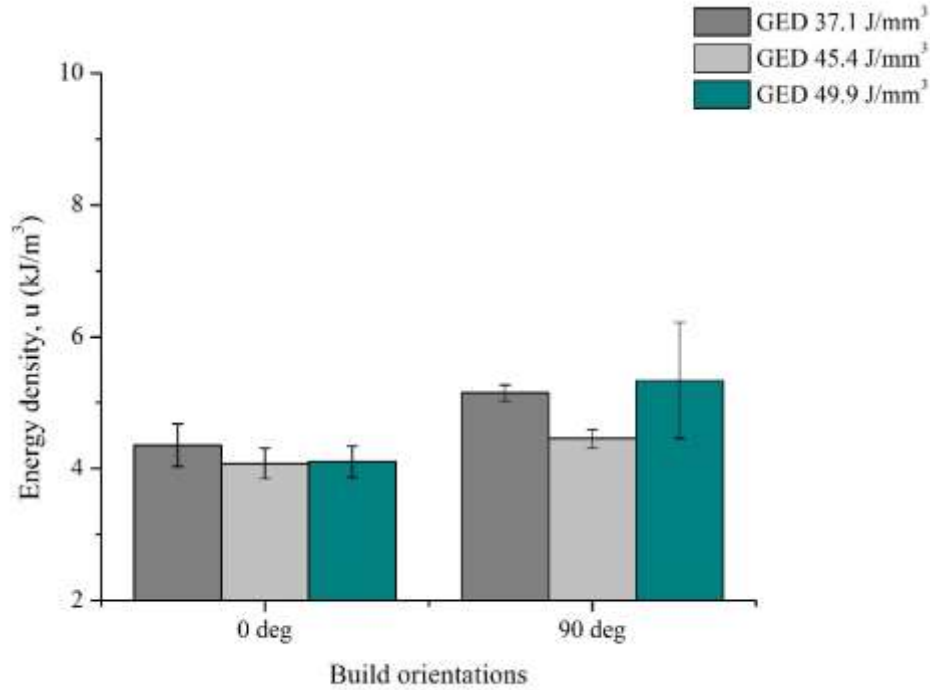


Figure 64: The average lattice strain of the tested CVN specimens.

### 6.3.2. Deformation Energy Density

The lattice deformation energy density was obtained from the UDED analysis section of Table XXVII. The observed trend may be reported here. The deformation energy density was higher for the specimens built at high GED, such as  $49.9\text{J/mm}^3$  (Figure 65), and for  $90^\circ$  build specimens. The higher deformation energy density than the  $0^\circ$  specimens. The  $90^\circ$  specimens faced a higher deformation energy density indicates a higher lattice strain induced in the specimen.



**Figure 65: The average deformation energy density of the tested CVN specimens.**

### 6.3.3. Crystal Size

The crystal size of the tested CVN specimens was represented by a bar chart in Figure 66. The data for the bar chart was taken from the UDEDM analysis (Table XXVII). It was discussed as the crystal size after lattice strain (i.e., deformed crystal), increased from lower to higher GED for both build orientations. The maximum average crystal size was observed for the GED 49.9J/mm<sup>3</sup> at 90° build orientation. Also, the 90° build specimens experienced comparatively larger crystals than the 0° build specimens. The standard deviation was represented by error bars on the bar chart. The range of the error bars was from 1.24 to 6.50.

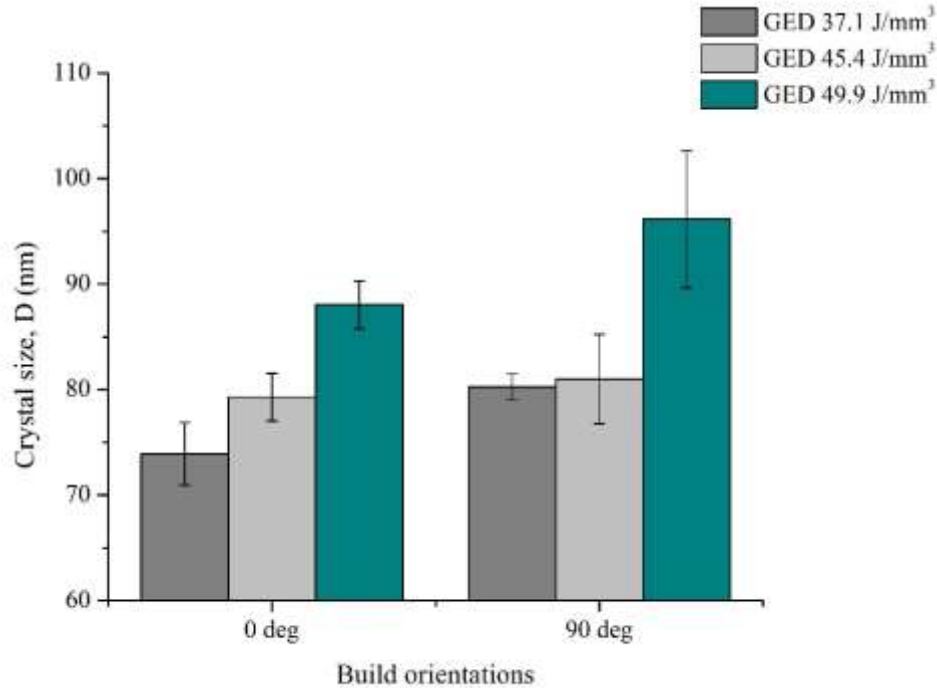


Figure 66: The average size of the crystal of the tested CVN specimens

#### 6.4. Microanalysis for the SHPB Specimens

The XRD experiment was performed for the SHPB specimens tested under high rate dynamic loading conditions using an SHPB apparatus. The strain rate ranged from 800 to  $2555\text{s}^{-1}$ . The corresponding XRD pattern for the three GEDs: 37.1, 45.4, and  $49.9\text{J/mm}^3$ , are presented in Figures 67, 68, and 69, respectively. From the XRD line graphs, no significant peak shift was observed for all the specimens. However, to visualize the presence of the peak shifts in the XRD line graph in Figures 67, 68, and 69, an average was taken over each Bragg's reflection plane and each build orientation and GED. The result was presented by a bar chart in Figure 70. However, it was found that the corresponding standard deviation (SD) from the average was tiny, which is hardly visible if the SD is presented in the bar chart of Figure 70. The standard deviation is shown in a separate bar chart in Figure 71. Since the peak shifts were minimal and

ignored for further calculation. Also, it was observed from Figures 67, 68, and 69 that the peak intensity of the XRD line graph depends on build orientation.

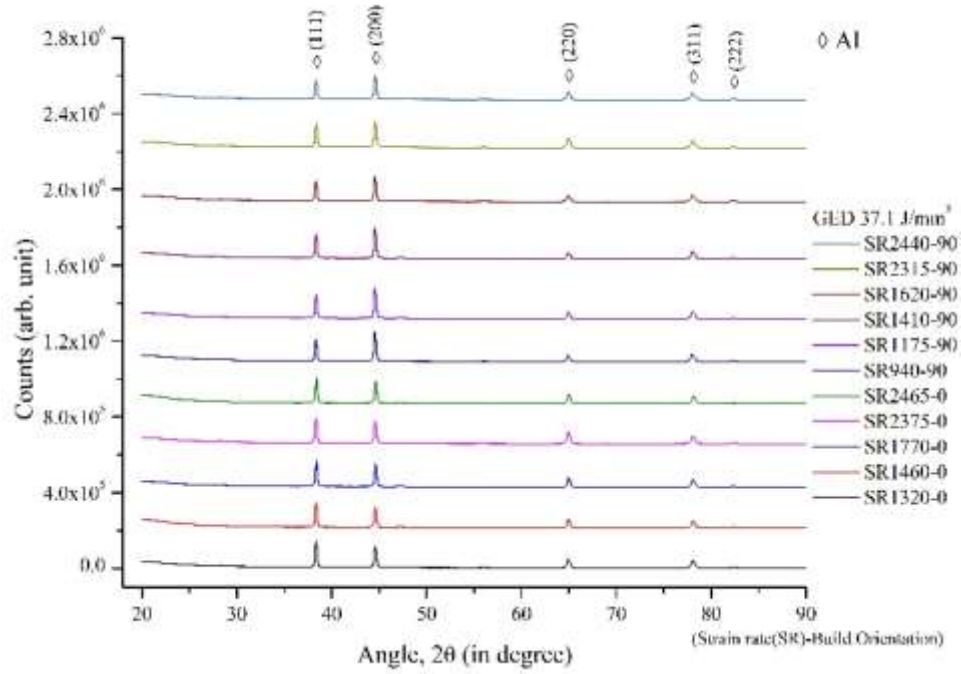


Figure 67: The XRD line graph for the specimens built at GED of  $37.1 \text{ J/mm}^3$ .

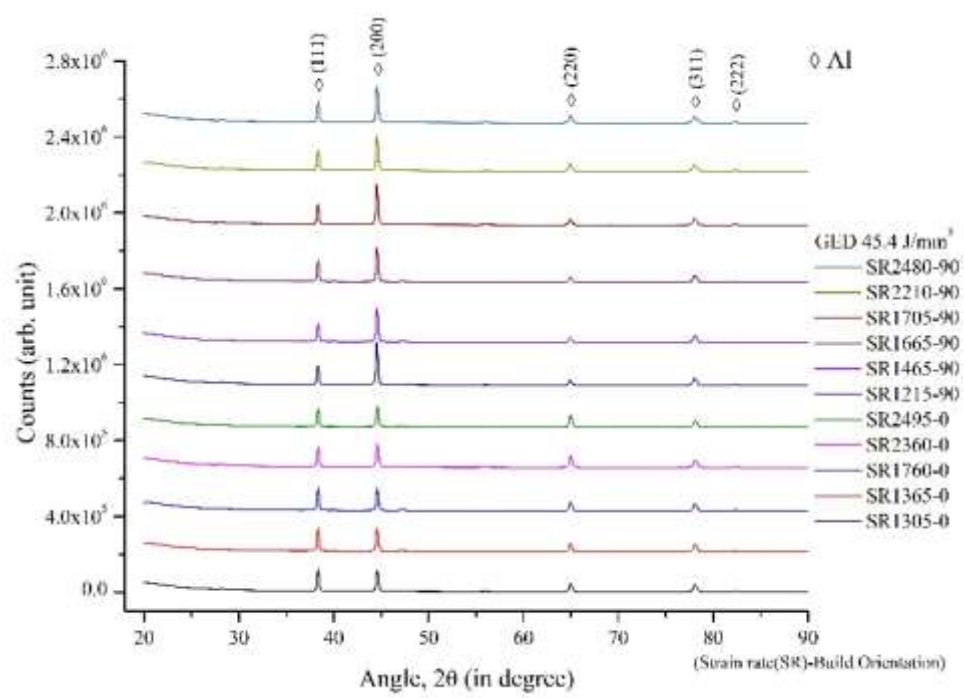


Figure 68: The XRD line graph for the specimens built at GED of 45.4J/mm<sup>3</sup>.

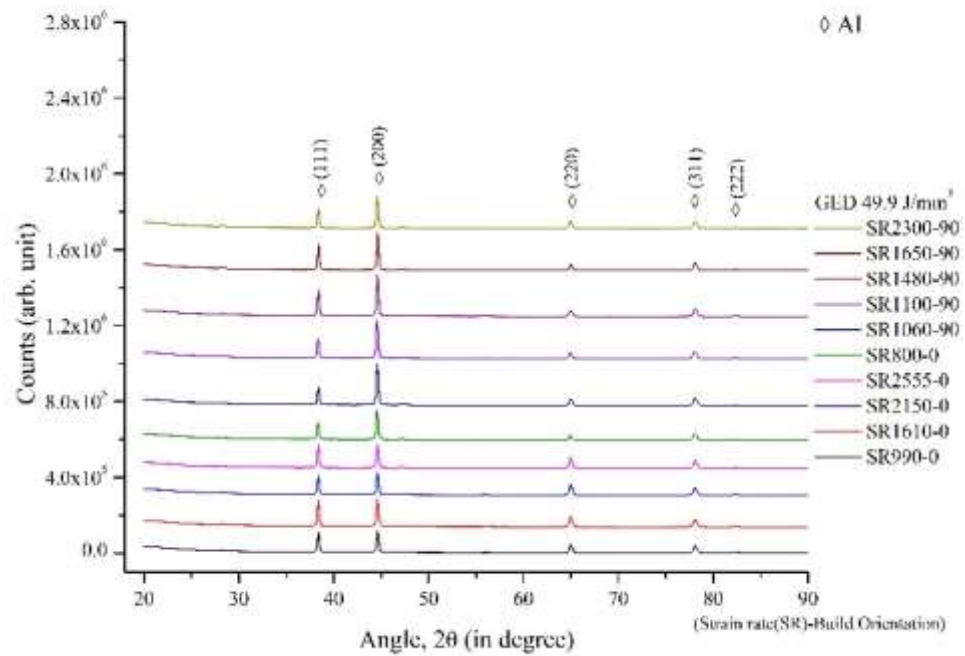


Figure 69: The XRD line graph for the specimens built at GED of 49.9J/mm<sup>3</sup>.

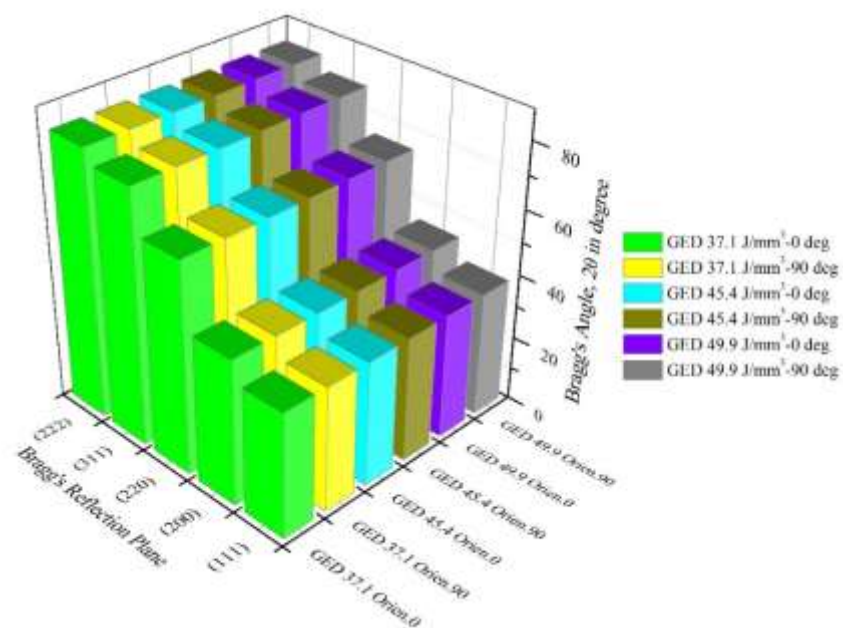


Figure 70: The average of the Bragg's angle for each peak of aluminum in the XRD line graphs for the tested SHPB specimens.

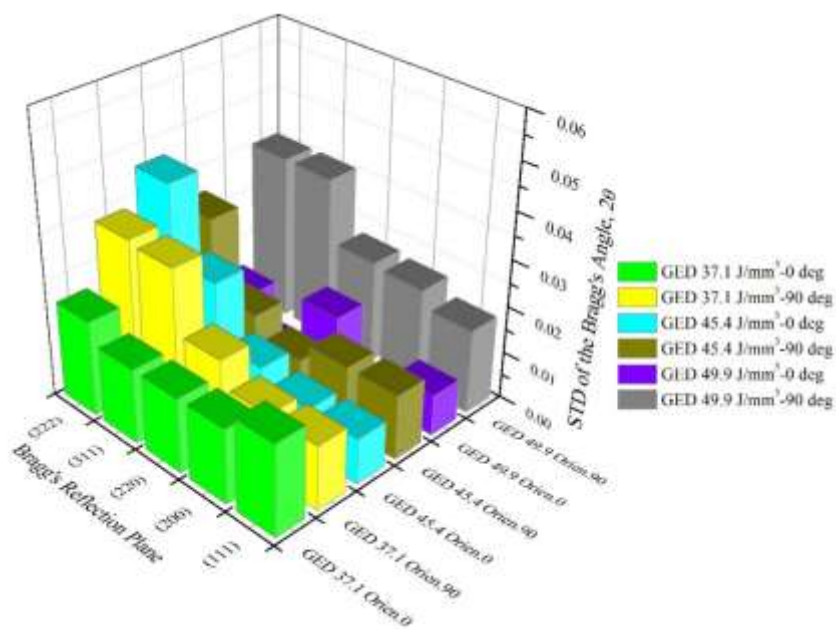


Figure 71: Standard deviation from the average of the Bragg's angle for each aluminum peak of Figure 70.

The lattice strain and crystal size of the tested SHPB specimens were calculated using the UDM, USDM, UDEDM, and Scherrer method. Table XXVIII presents the corresponding data of the lattice strain and crystal size. Table XXVIII shows that the Scherrer method gave lower values than the other three methods: UDM, USDM, and UDEDM. For further analysis, only UDEDM data were considered.

**Table XXVIII: Geometric parameters of the SLM-ALSi10Mg SHPB specimens. The specimens were prepared at two build orientations (BO): 0° and 90°, and three GEDs: 37.1, 45.4, and 49.9J/mm<sup>3</sup> and examined at different strain rates, which range from 800 to 2555s<sup>-1</sup> using SHPB.**

GED, J/mm <sup>3</sup>	BO	Scherrer method	W-H method							
			UDM			USDM			UEDM	
		D, nm	D, nm	ε, (×10 <sup>-3</sup> )	D, nm	σ, MPa	ε, (×10 <sup>-3</sup> )	D, nm	u, kJ/m <sup>3</sup>	ε, (×10 <sup>-3</sup> )
37.1	0°	27.92 ±0.36	141.67 ±30.75	2.068 ±0.09	63.55 ±5.63	68.21 ±4.06	1.430 ±0.09	89.43 ±12.09	6.60 ±1.37	1.764 ±0.09
	90°	27.22 ±0.46	149 ±32.62	2.163 ±0.13	63.80 ±6.73	71.50 ±6.15	1.498 ±0.13	91.63 ±13.77	7.28 ±2.34	1.848 ±0.14
45.4	0°	28.32 ±0.36	123.83 ±9.72	1.970 ±0.07	61.46 ±2.15	64.77 ±2.43	1.357 ±0.05	83.59 ±4.25	6.66 ±0.79	1.677 ±0.06
	90°	27.63 ±0.44	175.32 ±17.50	2.217 ±0.08	69.66 ±1.40	74.76 ±2.73	1.567 ±0.06	102.97 ±4.47	6.76 ±2.67	1.914 ±0.07
49.9	0°	28.53 ±0.38	163.24 ±22.86	2.095 ±0.09	68.67 ±3.69	69.90 ±4.01	1.465 ±0.08	99.17 ±8.49	7.76 ±0.78	1.797 ±0.09
	90°	28.62 ±0.61	160.62 ±16.63	2.084 ±0.07	69.80 ±5.22	70.19 ±2.73	1.471 ±0.06	100.37 ±8.49	6.79 ±2.12	1.798 ±0.06

#### 6.4.1. Lattice Strain

The lattice strain for the tested SHPB specimens is presented with a bar chart in Figure 72. The lattice strain data were obtained from the UDEDM analysis section of Table XXVIII. The observed trend may be reported here.

The influence of build orientation was observed on the lattice strain. Table XXVIII represents the measured highest strain rates for build orientations and GEDs that the SHPB specimens were investigated under dynamic impact loading conditions using SHPB. The GED of

37.1J/mm<sup>3</sup>-0° build specimens experienced a higher strain rate (i.e., 2495s<sup>-1</sup>) than that of 90° build specimens (i.e., 2480s<sup>-1</sup>) in the SHPB experiment. In contrast, the 0° build specimens experienced less lattice strain than the 90° build specimens. A similar phenomenon was observed for the other two GEDs. The 90° build specimens faced higher lattice strain than the 0° build specimens. The GED of 49.9J/mm<sup>3</sup>-0° build specimens were examined at a 2555s<sup>-1</sup> strain rate, whereas the GED-49.9J/mm<sup>3</sup> at 90° build specimens were at 2300s<sup>-1</sup>. However, the lattice strain was almost the same for both build orientations at GED of 49.9J/mm<sup>3</sup>.

**Table XXIX: Maximum strain rate applied for the SHPB specimens**

<b>GED, J/mm<sup>3</sup></b>	<b>Build orientation</b>	<b>Max. strain rate, s<sup>-1</sup></b>
<b>37.1</b>	0°	2495
	90°	2480
<b>45.4</b>	0°	2465
	90°	2440
<b>49.9</b>	0°	2555
	90°	2300

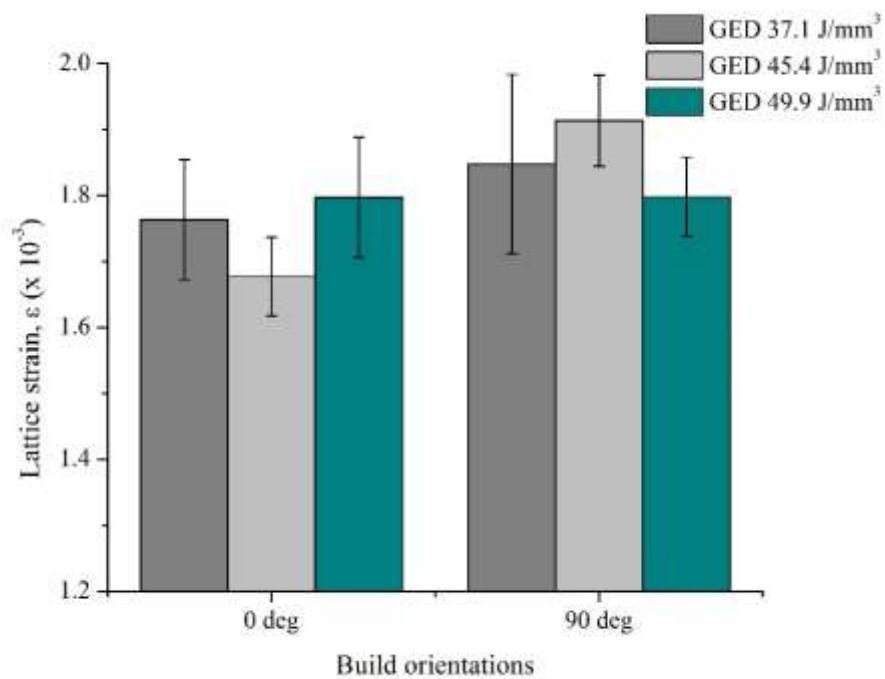


Figure 72: The average lattice strain of the tested SHPB specimens.

#### 6.4.1.1. Statistical Significance: Lattice Strain

The T-test results (Table XXXI and the statistical sample size in Table XXX) for the lattice strain show that most of the comparisons are not significantly different.

Table XXX: Lattice strain: the statistical sample size for the ‘student’s T-test’

GEDs & BOs	Statistical sample size	
	0°	90°
GED 37.1J/mm <sup>3</sup>	5	10
GED 45.4J/mm <sup>3</sup>	6	9
GED 49.9J/mm <sup>3</sup>	5	8

**Table XXXI: Student's T-test for the lattice strain**

<b>GEDs &amp; BOs</b>	<b>Probability, P</b>	<b>Confidence limit (%)</b>
<b>GED 37.1: 0° &amp; 90°</b>	P > 0.05	Not significant
<b>GED 45.4: 0° &amp; 90°</b>	P = 0.0004	99.96
<b>GED 49.9: 0° &amp; 90°</b>	P > 0.05	Not significant
<b>Build 0°: 37.1 &amp; 45.4</b>	P > 0.05	Not significant
<b>Build 0°: 37.1 &amp; 49.9</b>	P > 0.05	Not significant
<b>Build 0°: 45.4 &amp; 49.9</b>	P > 0.05	Not significant
<b>Build 90°: 37.1 &amp; 45.4</b>	P > 0.05	Not significant
<b>Build 90°: 37.1 &amp; 49.9</b>	P > 0.05	Not significant
<b>Build 90°: 45.4 &amp; 49.9</b>	P = 0.0184	98.16

#### **6.4.2. Deformation Energy Density**

The energy density in the lattice deformation for the tested SHPB specimens was obtained from the UDEDM analysis section data of Table XXVIII. A trend was observed that may be discussed here. It was observed that 90° build specimens experienced higher deformation energy density than the 0° build specimens except the specimens built at GED 49.9 J/mm<sup>3</sup>-0° (Figure 73). At GED 49.9 J/mm<sup>3</sup>, the 0° specimen experienced the max strain rate of 2555s<sup>-1</sup> whereas, the max strain rate is 2300s<sup>-1</sup> for the 90° build specimen.

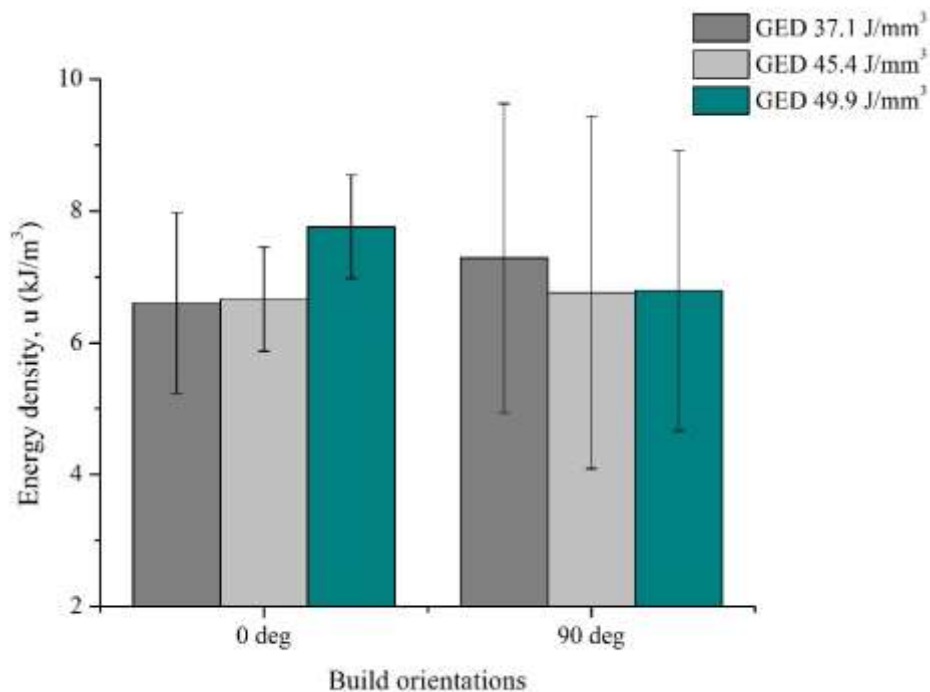


Figure 73: The average deformation energy density of the tested SHPB specimens.

#### 6.4.2.1. Statistical Significance: Deformation Energy

The T-test results (Table XXXIII and the statistical sample size in Table XXXII) for the lattice deformation energy show that none of the comparisons are significantly different.

Table XXXII: Deformation energy: the statistical sample size for the ‘student’s T-test’

GEDs & BOs	Statistical sample size	
	0°	90°
GED 37.1J/mm <sup>3</sup>	5	10
GED 45.4J/mm <sup>3</sup>	6	9
GED 49.9J/mm <sup>3</sup>	5	8

**Table XXXIII: Student's T-test for the deformation energy**

<b>GEDs &amp; BOs</b>	<b>Probability, P</b>	<b>Confidence limit (%)</b>
<b>GED 37.1: 0° &amp; 90°</b>	P > 0.05	Not significant
<b>GED 45.4: 0° &amp; 90°</b>	P > 0.05	Not significant
<b>GED 49.9: 0° &amp; 90°</b>	P > 0.05	Not significant
<b>Build 0°: 37.1 &amp; 45.4</b>	P > 0.05	Not significant
<b>Build 0°: 37.1 &amp; 49.9</b>	P > 0.05	Not significant
<b>Build 0°: 45.4 &amp; 49.9</b>	P > 0.05	Not significant
<b>Build 90°: 37.1 &amp; 45.4</b>	P > 0.05	Not significant
<b>Build 90°: 37.1 &amp; 49.9</b>	P > 0.05	Not significant
<b>Build 90°: 45.4 &amp; 49.9</b>	P > 0.05	Not significant

### 6.4.3. Crystal Size

The crystal size of the tested SHPB specimens was represented by a bar chart in Figure 74. The data for the bar chart was obtained from the UDEDM analysis section of Table XXVIII. In the previous section, a trend is that the 90° build specimens experienced higher lattice strain than the 0° build specimens. This behavior of the lattice strain influenced the size of the crystals of the specimens. The 90° build specimens experienced bigger crystals than the 0° build specimens.

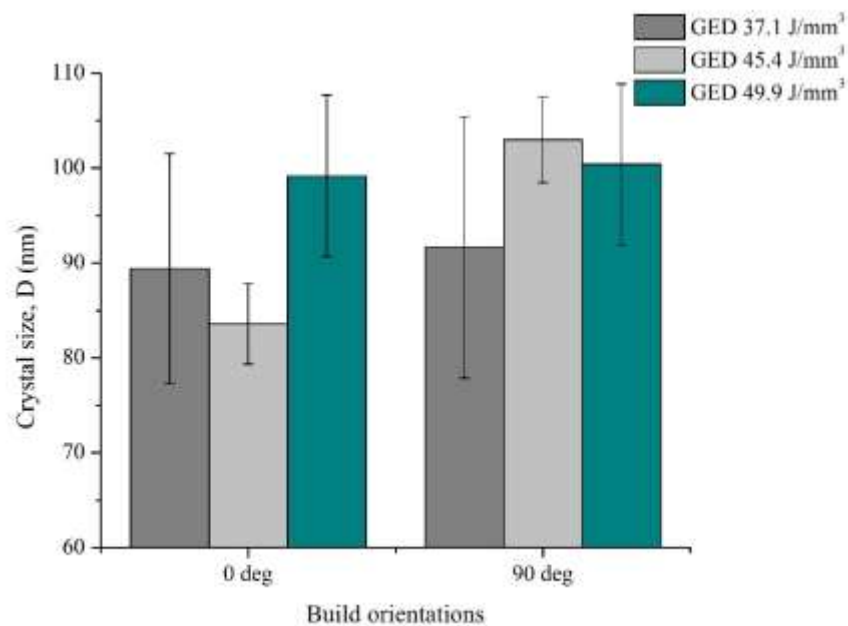


Figure 74: The average size of the crystal of the tested SHPB specimens.

#### 6.4.3.1. Statistical Significance: Crystal Size

The T-test results for the crystal size (Table XXXV and the statistical sample size in Table XXXIV) show that most of the comparisons are not significantly different.

Table XXXIV: Crystal size: the statistical sample size for the ‘student’s T-test’

GEDs & BOs	Statistical sample size	
	0°	90°
GED 37.1J/mm <sup>3</sup>	5	10
GED 45.4J/mm <sup>3</sup>	6	9
GED 49.9J/mm <sup>3</sup>	5	8

**Table XXXV: Student's T-test for the crystal size**

<b>GEDs &amp; BOs</b>	<b>Probability, P</b>	<b>Confidence limit (%)</b>
<b>GED 37.1: 0° &amp; 90°</b>	P > 0.05	Not significant
<b>GED 45.4: 0° &amp; 90°</b>	P = 0.0001	99.99
<b>GED 49.9: 0° &amp; 90°</b>	P > 0.05	Not significant
<b>Build 0°: 37.1 &amp; 45.4</b>	P > 0.05	Not significant
<b>Build 0°: 37.1 &amp; 49.9</b>	P > 0.05	Not significant
<b>Build 0°: 45.4 &amp; 49.9</b>	P = 0.0418	95.82
<b>Build 90°: 37.1 &amp; 45.4</b>	P > 0.05	Not significant
<b>Build 90°: 37.1 &amp; 49.9</b>	P > 0.05	Not significant
<b>Build 90°: 45.4 &amp; 49.9</b>	P > 0.05	Not significant

## 6.5. Observation

In summary, the XRD line graphs for the CVN and SHPB specimens were analyzed. No peak shifts were observed for the tested SHPB and Charpy impact specimens in the XRD line graphs. Statistical significance was not used for the CVN specimens for extremely small statistical sample size (i.e., sample size ranges from 2 to 3). For the tested SHPB specimens, no statistical significance was observed for the lattice strain, crystal size, and deformation energy at build orientations: 0° and 90°, and GEDs of 37.1, 45.4, and 49.9J/mm<sup>3</sup>.

## 7. Conclusion

The strain hardening behavior of SLM built AlSi10Mg under dynamic impact conditions was investigated for the SHPB (split Hopkinson pressure bar) and CVN (Charpy V-notch) specimens. The specimens were prepared at two build orientations (i.e.,  $0^\circ$  and  $90^\circ$ ) and at three different values of the global energy density (GED) (i.e., 37.1, 45.4, and  $49.9\text{J/mm}^3$ ). A split Hopkinson Pressure bar apparatus and a Charpy impact pendulum tester provided the required dynamic impact loading in laboratory premises.

For this investigation, the SHPB and CVN specimens were examined, focusing on three modes of failure: void formation, fracture type, and shear plane development. These failure modes affect the strain hardenability of the SLM built AlSi10Mg.

The corresponding observation and recommendations for future research were described at the end of each dissertation chapter. Following is a general conclusion obtained from the dissertation research.

- The strain hardening behavior was observed for both SHPB and CVN specimens under dynamic impact loading conditions.
- Void growth, type of fractures, roughness, and strength of the SLM built AlSi10Mg were affected by global energy density and build orientation. That influenced the strength and strain hardening characteristics of the SLM built AlSi10Mg.

## 8. References Cited

- [1] Xiong, Z. H., Liu, S. L., Li, S. F., Shi, Y., Yang, Y. F., and Misra, R. D. K. (2019). Role of melt pool boundary condition in determining the mechanical properties of selective laser melting AlSi10Mg alloy. *Materials Science and Engineering: A*, 740–741, 148–156. <https://doi.org/10.1016/j.msea.2018.10.083>
- [2] Cabrini, M., Calignano, F., Fino, P., Lorenzi, S., Lorusso, M., Manfredi, D., Testa, C., and Pastore, T. (2018). Corrosion behavior of heat-treated AlSi10Mg manufactured by laser powder bed fusion. *Materials*, 11(7). <https://doi.org/10.3390/ma11071051>
- [3] Zhou, L., Mehta, A., Schulz, E., McWilliams, B., Cho, K., and Sohn, Y. (2018). Microstructure, precipitates and hardness of selectively laser melted AlSi10Mg alloy before and after heat treatment. *Materials Characterization*, 143, 5–17. <https://doi.org/10.1016/j.matchar.2018.04.022>
- [4] Kempen, K., Thijs, L., Humbeeck, J. V., and Kruth, J.-P. (2015). Processing AlSi10Mg by selective laser melting: Parameter optimisation and material characterisation. *Materials Science and Technology*, 31(8), 917–923. <https://doi.org/10.1179/1743284714Y.0000000702>
- [5] Biffi, C. A., Fiocchi, J., and Tuissi, A. (2018). Selective laser melting of AlSi10 Mg: Influence of process parameters on Mg<sub>2</sub>Si precipitation and Si spheroidization. *Journal of Alloys and Compounds*, 755, 100–107. <https://doi.org/10.1016/j.jallcom.2018.04.298>
- [6] Riener, K., Albrecht, N., Ziegelmeier, S., Ramakrishnan, R., Haferkamp, L., Spierings, A. B., and Leichtfried, G. J. (2020). Influence of particle size distribution and morphology on the properties of the powder feedstock as well as of AlSi10Mg parts produced by laser powder bed fusion (LPBF). *Additive Manufacturing*, 34, 101286. <https://doi.org/10.1016/j.addma.2020.101286>

- [7] Chen, W. W., and Song, B. (2010). Split Hopkinson (Kolsky) Bar: Design, testing and applications. Springer Science & Business Media.
- [8] Ramesh, K. T. (2008). High rates and impact experiments. In W. N. Sharpe (Ed.), Springer Handbook of Experimental Solid Mechanics (pp. 929–960). Springer US.  
[https://doi.org/10.1007/978-0-387-30877-7\\_33](https://doi.org/10.1007/978-0-387-30877-7_33)
- [9] Tronskar, J. P., Mannan, M. A., and Lai, M. O. (2001). Direct measurement of displacement in instrumented Charpy impact testing for structural integrity assessment. *Journal of Testing and Evaluation*, 29(3), 246–257. <https://doi.org/10.1520/JTE12252J>
- [10] Amir, B., Samuha, S., and Sadot, O. (2019). Influence of selective laser melting machine source on the dynamic properties of AlSi10Mg alloy. *Materials*, 12(7), 1143.  
<https://doi.org/10.3390/ma12071143>
- [11] Nurel, B., Nahmany, M., Frage, N., Stern, A., and Sadot, O. (2018). Split Hopkinson pressure bar tests for investigating dynamic properties of additively manufactured AlSi10Mg alloy by selective laser melting. *Additive Manufacturing*, 22, 823–833.  
<https://doi.org/10.1016/j.addma.2018.06.001>
- [12] Zaretsky, E., Stern, A., and Frage, N. (2017). Dynamic response of AlSi10Mg alloy fabricated by selective laser melting. *Materials Science and Engineering: A*, 688, 364–370.  
<https://doi.org/10.1016/j.msea.2017.02.004>
- [13] Maconachie, T., Leary, M., Zhang, J., Medvedev, A., Sarker, A., Ruan, D., Lu, G., Faruque, O., and Brandt, M. (2020). Effect of build orientation on the quasi-static and dynamic response of SLM AlSi10Mg. *Materials Science and Engineering: A*, 788, 139445.  
<https://doi.org/10.1016/j.msea.2020.139445>

- [14] Tvergaard, V., and Needleman, A. (1986). Effect of material rate sensitivity on failure modes in the Charpy V-notch test. *Journal of the Mechanics and Physics of Solids*, 34(3), 213–241. [https://doi.org/10.1016/0022-5096\(86\)90019-0](https://doi.org/10.1016/0022-5096(86)90019-0)
- [15] Wang, L., Yang, L., Dong, X., and Jiang, X. (2019). Crack dynamics and fragmentation. In *Dynamics of Materials* (pp. 387–493). Elsevier. <https://doi.org/10.1016/B978-0-12-817321-3.00009-7>
- [16] Ruiz, C., and Mines, R. A. W. (1985). The Hopkinson pressure bar: An alternative to the instrumented pendulum for Charpy tests. *International Journal of Fracture*, 29(2), 101–109. <https://doi.org/10.1007/BF00034296>
- [17] Wang, L., Jiang, X., Guo, M., Zhu, X., and Yan, B. (2017). Characterisation of structural properties for AlSi10Mg alloys fabricated by selective laser melting. *Materials Science and Technology*, 33(18), 2274–2282. <https://doi.org/10.1080/02670836.2017.1398513>
- [18] Rosenthal, I., Shneck, R., and Stern, A. (2018). AlSi10Mg alloy fabricated by selective laser melting. *Annals of “Dunarea de Jos” University of Galati. Fascicle XII, Welding Equipment and Technology*, 29, 5–10. <https://doi.org/10.35219/awet.2018.01>
- [19] Rakesh, C. h. S., Priyanka, N., Jayaganthan, R., and Vasa, N. J. (2018). Effect of build atmosphere on the mechanical properties of AlSi10Mg produced by selective laser melting. *Materials Today: Proceedings*, 5(9, Part 1), 17231–17238. <https://doi.org/10.1016/j.matpr.2018.04.133>
- [20] Kempen, K., Thijs, L., Van Humbeeck, J., and Kruth, J.-P. (2012). Mechanical properties of AlSi10Mg produced by selective laser melting. *Physics Procedia*, 39, 439–446. <https://doi.org/10.1016/j.phpro.2012.10.059>

- [21] Kan, W. H., Nadot, Y., Foley, M., Ridosz, L., Proust, G., and Cairney, J. M. (2019). Factors that affect the properties of additively-manufactured AlSi10Mg: Porosity versus microstructure. *Additive Manufacturing*, 29, 100805. <https://doi.org/10.1016/j.addma.2019.100805>
- [22] Alghamdi, F., and Haghshenas, M. (2019). Microstructural and small-scale characterization of additive manufactured AlSi10Mg alloy. *SN Applied Sciences*, 1(3), 255. <https://doi.org/10.1007/s42452-019-0270-5>
- [23] Suttey, Luke Joseph. (2018). Evaluation of Metallurgical and Mechanical Properties of AlSi10Mg Produced by Selective Laser Melting. Montana Tech of The University of Montana.
- [24] McWilliams, B., Pramanik, B., Kudzal, A., and Taggart-Scarff, J. (2018). High strain rate compressive deformation behavior of an additively manufactured stainless steel. *Additive Manufacturing*, 24, 432–439. <https://doi.org/10.1016/j.addma.2018.09.016>
- [25] DebRoy, T., Wei, H. L., Zuback, J. S., Mukherjee, T., Elmer, J. W., Milewski, J. O., Beese, A. M., Wilson-Heid, A., De, A., and Zhang, W. (2018). Additive manufacturing of metallic components – Process, structure and properties. *Progress in Materials Science*, 92, 112–224. <https://doi.org/10.1016/j.pmatsci.2017.10.001>
- [26] ASTM, A. (2014). ASTM A370: standard test methods and definitions for mechanical testing of steel products.
- [27] ASTM, E 23. (2007). "Standard test methods for notched bar impact testing of metallic materials." E23-07a, Pennsylvania, PA, USA.
- [28] Kuelper, K. (2019). Dynamic mechanical response of additively manufactured 316L and AlSi10Mg. Graduate Theses & Non-Theses. [https://digitalcommons.mtech.edu/grad\\_rschr/207](https://digitalcommons.mtech.edu/grad_rschr/207)

- [29] Fazio, F., Piccione, G., Tribulato, K., Ferrantelli, V., Giangrosso, G., Arfuso, F., and Faggio, C. (2014). Bioaccumulation of heavy metals in blood and tissue of striped mullet in two Italian lakes. *Journal of Aquatic Animal Health*, 26(4), 278–284.  
<https://doi.org/10.1080/08997659.2014.938872>.
- [30] Newman, K. B., Lynch, D. A., Newman, L. S., Ellegood, D., and Newell, J. D. (1994). Quantitative computed tomography detects air trapping due to asthma. *Chest*, 106(1), 105–109.  
<https://doi.org/10.1378/chest.106.1.105>
- [31] Salah Uddin, M., Kuelper, K., and Pramanik, B. (2020). Characterization of dynamic material property of AlSi10Mg aluminum alloy under high strain rate compressive loading. In A. Tomsett (Ed.), *Light Metals 2020* (pp. 440–444). Springer International Publishing.  
[https://doi.org/10.1007/978-3-030-36408-3\\_62](https://doi.org/10.1007/978-3-030-36408-3_62)
- [32] Pramanik, B., Mantena, P. R., Tadepalli, T., and Rajendran, A. M. (2014). Indirect tensile characterization of graphite platelet reinforced vinyl ester nanocomposites at high-strain rate. *Open Journal of Composite Materials*, 04(04), 201–214.  
<https://doi.org/10.4236/ojcm.2014.44022>
- [33] Meyers, M. A. (1994). *Dynamic behavior of materials*. John Wiley & Sons.
- [34] Berkovic, L., Chabotier, A., Coghe, F., and Rabet, L. (2011). Measuring and modeling of low temperature Hopkinson tests. *Procedia Engineering*, 10, 1645–1650.  
<https://doi.org/10.1016/j.proeng.2011.04.275>
- [35] Leary, M., Maconachie, T., Sarker, A., Faruque, O., and Brandt, M. (2019). Mechanical and thermal characterisation of AlSi10Mg SLM block support structures. *Materials & Design*, 183, 108138. <https://doi.org/10.1016/j.matdes.2019.108138>

- [36] Blazynski, T. Z. (1987). *Materials at high strain rates*. Springer Science & Business Media.
- [37] Meyers, M. A., Xu, Y. B., Xue, Q., Pérez-Prado, M. T., and McNelley, T. R. (2003). Microstructural evolution in adiabatic shear localization in stainless steel. *Acta Materialia*, 51(5), 1307–1325. [https://doi.org/10.1016/S1359-6454\(02\)00526-8](https://doi.org/10.1016/S1359-6454(02)00526-8).
- [38] Lins, J. F. C., Sandim, H. R. Z., Kestenbach, H.-J., Raabe, D., and Vecchio, K. S. (2007). A microstructural investigation of adiabatic shear bands in an interstitial free steel. *Materials Science and Engineering: A*, 457(1), 205–218. <https://doi.org/10.1016/j.msea.2006.12.019>
- [39] Reedy, E. D., and Stavig, M. E. (2020). Interfacial toughness: Dependence on surface roughness and test temperature. *International Journal of Fracture*, 222(1), 1–12. <https://doi.org/10.1007/s10704-019-00419-0>
- [40] Boccaccini, A. R., and Winkler, V. (2002). Fracture surface roughness and toughness of Al<sub>2</sub>O<sub>3</sub>-platelet reinforced glass matrix composites. *Composites Part A: Applied Science and Manufacturing*, 33(1), 125–131. [https://doi.org/10.1016/S1359-835X\(01\)00080-X](https://doi.org/10.1016/S1359-835X(01)00080-X)
- [41] Nasser, M. H. B., Grasselli, G., and Mohanty, B. (2010). Fracture toughness and fracture roughness in anisotropic granitic rocks. *Rock Mechanics and Rock Engineering*, 43(4), 403–415. <https://doi.org/10.1007/s00603-009-0071-z>
- [42] Ponson, L., Srivastava, A., Osovski, S., Bouchaud, E., Tvergaard, V., and Needleman, A. (2013). Correlating toughness and roughness in ductile fracture. ArXiv:1307.4413 [Cond-Mat]. <http://arxiv.org/abs/1307.4413>, [hal-00845351](https://hal.archives-ouvertes.fr/hal-00845351), <https://hal.archives-ouvertes.fr/hal-00845351>
- [43] Bouchaud, E., and Bouchaud, J.-P. (1994). Fracture surfaces: Apparent roughness, relevant length scales, and fracture toughness. *Physical Review B*, 50(23), 17752–17755. <https://doi.org/10.1103/PhysRevB.50.17752>

- [44] Ritchie, R. O. (2011). The conflicts between strength and toughness. *Nature Materials*, 10(11), 817–822. <https://doi.org/10.1038/nmat3115>
- [45] Hollomon, J. H. (1945). Tensile deformation. *Aime Trans*, 12(4), 1-22.
- [46] Dai, K., Villegas, J., and Shaw, L. (2005). An analytical model of the surface roughness of an aluminum alloy treated with a surface nanocrystallization and hardening process. *Scripta Materialia*, 52(4), 259–263. <https://doi.org/10.1016/j.scriptamat.2004.10.021>
- [47] Fischer, H., Schäfer, M., and Marx, R. (2003). Effect of surface roughness on flexural strength of veneer ceramics. *Journal of Dental Research*, 82(12), 972–975. <https://doi.org/10.1177/154405910308201207>
- [48] Underwood, E. E. (1986). Quantitative fractography. In G. F. Vander Voort (Ed.), *Applied Metallography* (pp. 101–122). Springer US. [https://doi.org/10.1007/978-1-4684-9084-8\\_8](https://doi.org/10.1007/978-1-4684-9084-8_8)
- [49] Banerji, K. (1988). Quantitative fractography: A modern perspective. *Metallurgical Transactions A*, 19(4), 961–971. <https://doi.org/10.1007/BF02628381>
- [50] Biffi, C. A., Fiocchi, J., Bassani, P., Paolino, D. S., Tridello, A., Chiandussi, G., Rossetto, M., and Tuissi, A. (2017). Microstructure and preliminary fatigue analysis on AlSi10Mg samples manufactured by SLM. *Procedia Structural Integrity*, 7, 50–57. <https://doi.org/10.1016/j.prostr.2017.11.060>
- [51] Delahaye, J., Tchuindjang, J. T., Lecomte-Beckers, J., Rigo, O., Habraken, A. M., and Mertens, A. (2019). Influence of Si precipitates on fracture mechanisms of AlSi10Mg parts processed by Selective Laser Melting. *Acta Materialia*, 175, 160–170. <https://doi.org/10.1016/j.actamat.2019.06.013>

- [52] Han, Q., and Jiao, Y. (2019). Effect of heat treatment and laser surface remelting on AlSi10Mg alloy fabricated by selective laser melting. *The International Journal of Advanced Manufacturing Technology*, 102(9), 3315–3324. <https://doi.org/10.1007/s00170-018-03272-y>
- [53] Uzan, N. E., Ramati, S., Shneck, R., Frage, N., and Yeheskel, O. (2018). On the effect of shot-peening on fatigue resistance of AlSi10Mg specimens fabricated by additive manufacturing using selective laser melting (Am-slm). *Additive Manufacturing*, 21, 458–464. <https://doi.org/10.1016/j.addma.2018.03.030>
- [54] Wang, L., Jiang, X., Guo, M., Zhu, X., and Yan, B. (2017). Characterisation of structural properties for AlSi10Mg alloys fabricated by selective laser melting. *Materials Science and Technology*, 33(18), 2274–2282. <https://doi.org/10.1080/02670836.2017.1398513>
- [55] Chen, B., Moon, S. K., Yao, X., Bi, G., Shen, J., Umeda, J., and Kondoh, K. (2018). Comparison study on additive manufacturing (AM) and powder metallurgy (PM) alsi10mg alloys. *JOM*, 70(5), 644–649. <https://doi.org/10.1007/s11837-018-2793-4>
- [56] Padovano, E., Badini, C., Pantarelli, A., Gili, F., and D’Aiuto, F. (2020). A comparative study of the effects of thermal treatments on AlSi10Mg produced by laser powder bed fusion. *Journal of Alloys and Compounds*, 831, 154822. <https://doi.org/10.1016/j.jallcom.2020.154822>
- [57] Rosenthal, I., Shneck, R., and Stern, A. (2018). Heat treatment effect on the mechanical properties and fracture mechanism in AlSi10Mg fabricated by additive manufacturing selective laser melting process. *Materials Science and Engineering: A*, 729, 310–322. <https://doi.org/10.1016/j.msea.2018.05.074>
- [58] Lam, L. P., Zhang, D. Q., Liu, Z. H., and Chua, C. K. (2015). Phase analysis and microstructure characterisation of AlSi10Mg parts produced by Selective Laser Melting. *Virtual and Physical Prototyping*, 10(4), 207–215. <https://doi.org/10.1080/17452759.2015.1110868>

- [59] Maamoun, A. H., Veldhuis, S. C., and Elbestawi, M. (2019). Friction stir processing of AlSi10Mg parts produced by selective laser melting. *Journal of Materials Processing Technology*, 263, 308–320. <https://doi.org/10.1016/j.jmatprotec.2018.08.030>
- [60] Maamoun, A. H., Elbestawi, M. A., and Veldhuis, S. C. (2018). Influence of shot peening on AlSi10Mg parts fabricated by additive manufacturing. *Journal of Manufacturing and Materials Processing*, 2(3), 40. <https://doi.org/10.3390/jmmp2030040>
- [61] Maamoun, A. H., Xue, Y. F., Elbestawi, M. A., and Veldhuis, S. C. (2019). The effect of selective laser melting process parameters on the microstructure and mechanical properties of Al6061 and AlSi10Mg alloys. *Materials*, 12(1), 12. <https://doi.org/10.3390/ma12010012>
- [62] Maamoun, A. H., Elbestawi, M., Dosbaeva, G. K., and Veldhuis, S. C. (2018). Thermal post-processing of AlSi10Mg parts produced by Selective Laser Melting using recycled powder. *Additive Manufacturing*, 21, 234–247. <https://doi.org/10.1016/j.addma.2018.03.014>
- [63] Singla, G., Singh, K., and Pandey, O. P. (2013). Williamson–Hall study on synthesized nanocrystalline tungsten carbide (Wc). *Applied Physics A*, 113(1), 237–242. <https://doi.org/10.1007/s00339-012-7531-0>
- [64] Cullity, B. D. (1978). *Elements of x-ray diffraction* (2nd ed). Addison-Wesley Pub. Co.
- [65] Banerjee, D. (n.d.). X-Ray Diffraction (XRD). Retrieved December 6, 2020, from [https://www.google.com/url?sa=t&rct=j&q=&esrc=s&source=web&cd=&cad=rja&uact=8&ved=2ahUKEwifx7Wsp7ntAhWRtlkKHY1VD9MQFjAAegQIBRAC&url=https%3A%2F%2Fwww.iitk.ac.in%2Fche%2Fpdf%2Fresources%2FXRD-reading-material.pdf&usg=AOvVaw3Iho2XZvVslvwi\\_6\\_WR1SA](https://www.google.com/url?sa=t&rct=j&q=&esrc=s&source=web&cd=&cad=rja&uact=8&ved=2ahUKEwifx7Wsp7ntAhWRtlkKHY1VD9MQFjAAegQIBRAC&url=https%3A%2F%2Fwww.iitk.ac.in%2Fche%2Fpdf%2Fresources%2FXRD-reading-material.pdf&usg=AOvVaw3Iho2XZvVslvwi_6_WR1SA)

- [66] Zhao, Y., and Zhang, J. (2008). Microstrain and grain-size analysis from diffraction peak width and graphical derivation of high-pressure thermomechanics. *Journal of Applied Crystallography*, 41(6), 1095–1108. <https://doi.org/10.1107/S0021889808031762>.
- [67] Shiraishi, M., and Inagaki, M. (2003). Chapter 10—X-ray diffraction methods to study crystallite size and lattice constants of carbon materials. In E. Yasuda, M. Inagaki, K. Kaneko, M. Endo, A. Oya, and Y. Tanabe (Eds.), *Carbon Alloys* (pp. 161–173). Elsevier Science. <https://doi.org/10.1016/B978-008044163-4/50010-3>
- [68] Xu, H., and Guo, H. (Eds.). (2011). *Thermal barrier coatings*. Woodhead Pub Ltd.
- [69] Ortiz, A. L., and Shaw, L. (2004). X-ray diffraction analysis of a severely plastically deformed aluminum alloy. *Acta Materialia*, 52(8), 2185–2197. <https://doi.org/10.1016/j.actamat.2004.01.012>
- [70] Sivasankaran, S., Sivaprasad, K., Narayanasamy, R., & Satyanarayana, P. V. (2011). X-ray peak broadening analysis of AA 6061100–x–xwt.% Al<sub>2</sub>O<sub>3</sub> nanocomposite prepared by mechanical alloying. *Materials Characterization*, 62(7), 661–672. <https://doi.org/10.1016/j.matchar.2011.04.017>
- [71] Williamson, G. K., and Hall, W. H. (1953). X-ray line broadening from filed aluminium and wolfram. *Acta Metallurgica*, 1(1), 22–31. [https://doi.org/10.1016/0001-6160\(53\)90006-6](https://doi.org/10.1016/0001-6160(53)90006-6)
- [72] Khorsand Zak, A., Abd. Majid, W. H., Abrishami, M. E., and Yousefi, R. (2011). X-ray analysis of ZnO nanoparticles by Williamson–Hall and size–strain plot methods. *Solid State Sciences*, 13(1), 251–256. <https://doi.org/10.1016/j.solidstatesciences.2010.11.024>
- [73] Rosenberg, Y., Machavariani, V. S., Voronel, A., Garber, S., Rubshtein, A., Frenkel, A. I., and Stern, E. A. (2000). Strain energy density in the x-ray powder diffraction from mixed

crystals and alloys. *Journal of Physics: Condensed Matter*, 12(37), 8081–8088.

<https://doi.org/10.1088/0953-8984/12/37/307>

[74] Zhang, J.-M., Zhang, Y., Xu, K.-W., and Ji, V. (2007). Young's modulus surface and Poisson's ratio curve for cubic metals. *Journal of Physics and Chemistry of Solids*, 68(4), 503–510. <https://doi.org/10.1016/j.jpcs.2007.01.025>

[75] Tallon, J. L., and Wolfenden, A. (1979). Temperature dependence of the elastic constants of aluminum. *Journal of Physics and Chemistry of Solids*, 40(11), 831–837.

[https://doi.org/10.1016/0022-3697\(79\)90037-4](https://doi.org/10.1016/0022-3697(79)90037-4)

[76] Augustin, A., Udupa, K. R., and K., U. B. (2016). Crystallite size measurement and micro-strain analysis of electrodeposited copper thin film using Williamson-Hall method. *AIP Conference Proceedings*, 1728(1), 020492. <https://doi.org/10.1063/1.4946543>

[77] Madhusudhan, D., Chand, S., Ganesh, S., and Saibhargavi, U. (2018). Modeling and simulation of Charpy impact test of maraging steel 300 using Abaqus. *IOP Conference Series: Materials Science and Engineering*, 330, 012013. <https://doi.org/10.1088/1757-899X/330/1/012013>

[78] Dubey, P., Sharma, N. K., Rathi, A., and Kumar, A. (2016). Studies on Impact Behavior of Cortical Bone using Charpy Test and Finite Element Simulation. In *Proceedings of the World Congress on Engineering (Vol. 2)*.